UNIVERSITY OF CALIFORNIA
RIVERSIDE

Magnetic Insulator Thin Films and Induced Magneto-Transport Effect at Normal Metal / Magnetic Insulator Interface

A Dissertation submitted in partial satisfaction
of the requirements for the degree of

Doctor of Philosophy

in

Physics

by

Tao Lin

August 2013

Dissertation Committee:
Professor Jing Shi, Chairperson
Professor Chun Ning (Jeanie) Lau
Professor Ward P. Beyermann

Copyright by
Tao Lin
2013

The Dissertation of Tao Lin is approved:

_____

_____

_____

Committee Chairperson

University of California, Riverside

Acknowledgments

It is a milestone at this moment when I accomplish my work of Ph.D. study in University of California Riverside. With all pains and gains, the journey of the past years builds a solid foundation for my future, and will be always memorable in my life.

First and foremost I gratefully acknowledge my advisor, Professor Jing Shi, for the opportunity of working in his research group as his student. Prof. Shi is not only an excellent scientist but also a gracious mentor, who is always professional, insightful, supportive, and patient. He taught me a lot in both academia and life, and sets a role model for me in my lifetime. My work could not be done without his guidance, support and encouragement. I could not ask for a better mentoring. Thank you for teaching and advising me, Professor Shi.

I am also very grateful to my committee members, Professor Jeanie Lau and Professor Ward Beyermann, for their interests and precious time. And thank you to all the faculty and staff in Physics department at UC Riverside, for making it great pleasure here.

I would like to acknowledge my colleagues in the lab for their unceasing help and friendship. Thank you to Xinfei Liu, Peng Wei, Deqi Wang, Ray Sachs, Jianxing Ma, Zuhong Xiong, Di Wu, Yong Pu, Zhiyong Wang, Zilong Jiang, Chi Tang, Yadong Xu, Zhisheng Lin, and Hamad Alyahyaei. And I also thank to Dong Yan, Dexter Humphrey,

John Butler, Nissim Amos, Brian Youngblood and Ilya Krivorotov for their technical help. You are wonderful people and it is pleasure to work with you.

Also, I would like to deeply thank my friends here: Dong Gui, Wei Han, Dezheng Sun, Wenzhong Bao and Honghui Cheng, Hsiang-Ku Lin, Yingdi Liu, Xiaoxiao He and Guanqun Shi, Yeming Zhu, Guangdeng Liao and Yiming Li, Li Yan and Ying Liu, Gang Liu, Hang Zhang, Yan Li, Adrian Swartz, Hua Wen, Renjing Zheng, Bin Cheng, Jason Morales, Xiaojin Tan, Yachong Wang, Yang Zhao and Xiaoquan Zhou, Lei Guo, and so many people that I cannot list all here. I enjoyed every wonderful moment together with you and our friendship will be cherished a lifetime.

Last but not least, I greatly appreciate my family for their continuously support and encouraging. Especially, I could not express any more gratitude to my wife, Jiewen Ouyang, for her love, trust, patience, understanding and encouragement. She is always standing behind me and shares the optimism with me, as well as taking care of my daily life and encouraging me in my work. It is always the most precious time spending with her. I was really lucky to meet you and I love you so much, my dear.

Thank you all!!!

To my family for supporting and encouraging me with affections and love.

ABSTRACT OF THE DISSERTATION

Magnetic Insulator Thin Films and Induced Magneto-Transport Effect
at Normal Metal / Magnetic Insulator Interface

by

Tao Lin

Doctor of Philosophy, Graduate Program in Physics
University of California, Riverside, August 2013
Professor Jing Shi, Chairperson

The discipline of spintronics with magnetic insulators (MI) has attracted a great deal of attention in both research and application interests. Yttrium iron garnet (YIG) is a ferrimagnetic insulator which is recently called the spin Seebeck insulator, for it supports pure spin current generation. Non-magnetic metals (NM) with strong spin-orbit interaction (e.g. Pd, Pt), are used as either spin current generator or detector based on the spin Hall effect (SHE) or the inverse spin Hall effect (ISHE). The combination of these two types of material plays a very important role in spintronics. On the other hand, a recent magneto-transport study shows strong evidence of a magnetic proximity effect in thin Pt films deposited on YIG. It is desirable to have more experimental evidence to distinguish the two effects qualitatively and even quantitatively. In my work here, the induced magneto-transport effects at NM/MI interface will be discussed in details, including induced independent spin moments at the interface and disentanglement of

anisotropic magnetoresistance (AMR) and spin Hall magnetoresistance (SMR), as well as the fabrication of YIG thin films and devices.

Pulsed laser deposition (PLD) has emerged as a preferred technique to deposit complex oxide thin films, heterostructures, and superlattices with high quality. The general PLD techniques will be discussed in Chapter I, with examples of $La_{0.7}Sr_{0.3}MnO_3$ and Fe_3O_4 thin films fabrication and characterization. In Chapter II, I will discuss our approach to grow YIG films on (110)- and (111)-oriented gadolinium gallium garnet (GGG) substrates. In both orientations, we have successfully grown epitaxial YIG thin films confirmed by the patterns of the reflection high-energy electron diffraction (RHEED). The layer-by-layer mode was achieved with lower laser repetition rates than reported by other groups. For both orientations, the atomic force microscopy images showed that the YIG surface was extremely flat, and flat terraces were found with the atomic step height on film surface. The magnetic properties were measured with in-plane easy-axis and very narrow coercive field, which was almost independent of temperature. The in-plane magnetic anisotropy was explored as well. This work paves the way to engineering anisotropy of the thin films for YIG-based magnetic devices.

As a thin layer of NM (e.g. Pd, Pt) was deposited on the MI thin film like YIG, NM developed both low- and high-field magneto-transport effects that were absent in

standalone NM or thick NM on YIG. While the low-field magnetoresistance (MR) peaks of NM tracked the coercive field of the YIG film, the much larger high-field MR and the anomalous Hall effect (AHE-like) did not appear to have any relationship with the bulk YIG magnetization. The high-field MR had a sign reversal at some intermediate temperature for both Pd and Pt, and the magnitude of AHE-like signal of Pd increased with decreasing temperature, while that of Pt had sign reversal. The distinct high-field magneto-transport effects in NM/MI structures had been investigated with different NM film thicknesses and some control samples, and were shown to be caused by interfacial local moments in NM. Besides, both a clear resistivity minimum and a ln(T) temperature dependence were observed at low temperatures in thin NM films, suggesting that the Kondo effect may be relevant. Detailed discussions about the origin of these effects will be presented in Chapter III.

The AMR effect, evidence for a proximity induced magnetic moment in Pt/YIG bilayer, was previously found absent in experiments with a rotating magnetic field applied at room temperature. Instead, the observed magnetoresistance was attributed to a new type of effect called SMR that is caused by magnetization-dependent spin current reflection at the interface. In both Pd/YIG and Pt/YIG bilayers, however, we have observed that SMR and AMR coexist over a wide range of temperatures with AMR dominating at low

temperatures. Detailed experimental results of the temperature dependence and field dependence of the two types of magnetoresistance were shown to disentangle AMR and SMR quantitatively. While AMR is likely caused by the proximity induced magnetization in NM that saturates at relatively low fields, at higher magnetic fields when additional interfacial magnetic moments are gradually aligned, the spin current reflection effect and consequently SMR are greatly enhanced. The detailed analysis and discussions will be presented in Chapter IV.

Contents

List of Figures xv

List of Tables xxii

Chapter I Magnetic Thin Film Growth and Characterization 1

1.1 Pulsed Laser Deposition 1

1.2 $La_{1-x}Sr_xMnO_3$ (LSMO) Thin Film Preparation and Property Measurements 5

1.3 Fe_3O_4 Thin Film Preparation and Measurements 12

1.4 Discussion 19

Chapter II Yttrium Iron Garnet Thin Film Growth 22

2.1 Introduction 22

2.2 Sample Preparation and Characterization 24

2.3 Optimization of Growth Parameters 26

2.3.1 Substrate Treatment 26

2.3.2 Post-annealing Effects 27

2.3.3 Molecular Beam Epitaxy and Layer-by-layer Growth 30

2.3.4 Atomically Flat Terraces 32

2.4 Magnetic Properties 33

2.5 Discussion 35

Chapter III Induced Magneto-transport Effects at Interface 38

3.1 Introduction 38

3.1.1 Anomalous Hall Effect 38

3.1.2 Seebeck Effect and Anomalous Nernst Effect 41

3.1.3 Spin Hall Effect and Inversed Spin Hall Effect 42

3.1.4 Spin Seebeck Effect 45

3.1.5 Magnetic Proximity Effect vs. Spin Seebeck Effect 48

3.2 Device Fabrication and Measurements 50

3.3 Low-Field Magneto-transport Effects 54

3.4 High-Field Magneto-transport Effects 58

3.4.1 High Field Magneto-resistance 58

3.4.2 AHE-like Effect 60

3.4.3 Possible Kondo Effect 66

3.5 Discussion 67

Chapter IV Spin Hall Magnetoresistance 70

4.1 Introduction 70

4.1.1 Anisotropic Magneto-resistance (AMR) 70

4.1.2 Spin Hall Magneto-resistance (SMR) 72

4.2 Device Fabrication and Measurements 76

4.3 Low-Field Magnetoresistance 78

4.4 AMR vs. SMR 80

4.5 Temperature Dependence of AMR/SMR 84

4.6 Field Dependence of AMR/SMR 89

4.7 Discussion 91

Chapter V Appendix 94

5.1 Laboratory Instruments Management system (LIMs) 94

5.2 PLD Operational Manual 99

5.2.1 Sample Loading 99

5.2.2 System Startup 101

5.2.3 Deposition Procedure 102

5.2.4 System Shutdown 102

Chapter VI References 104

List of Figures

Figure I-1 Schematic illustration of Pulsed Laser Deposition system. 2

Figure I-2 Picture of our homemade PLD system. Inset: Zoom view of the main UHV chamber. 3

Figure I-3 Schematic illustration of STAIB® RHEED system with differential pumping stage. [staibinstruments.com]..... 3

Figure I-4 Plume injected from yttrium iron garnet (YIG) target during the deposition.... 5

Figure I-5 Schematic illustration of a unit cell of $RaMnO_3$ in real space. The rare-earth Ra atoms are at the corners with one Mn atom at the center of the cubic. Six oxygen atoms are at the center of the faces. 6

Figure I-6 RHEED patterns before (left) and after (right) deposition of LSMO on STO(110) are consistent, suggesting epitaxial growth of LSMO on STO(110). 8

Figure I-7 RHEED intensity oscillations suggest layer by layer growth mode during LSMO/STO(110) deposition. Each period of the oscillation corresponds to one mono-layer of LSMO, with full coverage at peaks and half coverage at valleys. 8

Figure I-8 HRTEM image of $[LSMO(7ML)/STO(3ML)]_{14}$/STO(110) superlattice sample with 14 periodic units in full range. The inset shows high resolution image near substrate. The dark and bright part corresponds to STO and LSMO layers respectively. 9

Figure I-9 (a) In-plane magnetic hysteresis loops of LSMO/STO(110) at 5K. (b) Temperature dependence of in-plane saturate magnetic moments of LSMO/STO(110).. 10

Figure I-10 Temperature dependence of resistivity of LSMO/STO(110) at zero field..... 10

Figure I-11 (a) In-plane magnetoresistance of LSMO/STO(110) as function of field at different temperatures. (b) Temperature dependence of MR ratio (H = 10 kOe). 11

Figure I-12 Schematic illustration of a unit cell of Fe_3O_4 in real space. 13

Figure I-13 RHEED patterns before (left) and after (right) deposition of Fe_3O_4 on MgO(100) are consistent, suggesting epitaxial growth of Fe_3O_4 on MgO(100). 15

Figure I-14 RHEED intensity oscillations suggest layer-by-layer growth mode during Fe_3O_4/MgO(100) deposition. Each period of the oscillation corresponds to one

mono-layer (1/4 unit cell) of Fe_3O_4, with full coverage at peaks and half coverage at valleys. 15

Figure I-15 (a) In-plane and (b) out-of-plane magnetic hysteresis loops of Fe_3O_4/MgO(100) thin film at 300K. The magnetization has in-plane anisotropy. 16

Figure I-16 Normalized resistivity of Fe_3O_4/MgO(100) thin film as a function of inversed temperture. Inset: Temperature dependence of resistance of Fe_3O_4/MgO(100) thin film. 17

Figure I-17 (a) Magnetoresistance and (b) anomalous Hall effect of Fe_3O_4/MgO(100) thin film at different temperatures. Inset: Temperature dependence of AHE resistance..... 18

Figure I-18 Scaling of longitudinal conductivity and anomalous Hall conductivity. The typical driven current is 100 nA except one indicated. 19

Figure II-1 Schematic illustration of a unit cell of YIG crystal structure in real space. ... 23

Figure II-2 AFM images of GGG(110) substrates under different treatments: (a) pristine substrate with mechanical polishing; (b) chemical etching; (c) annealing in oxygen at 600 °C; (d) annealing in oxygen at 1000 °C; (e) annealing in oxygen at 1300 °C..... 26

Figure II-3 (a) The color of as-grown YIG film (before parameters optimization) is dark brown (top), and the RHEED pattern disappears (bottom), suggesting amorphous YIG deposition. (b) After annealing in oxygen at 800°C for 6 hours, the color of YIG film become light yellow (top), and the RHEED pattern reforms (bottom), suggesting crystallization of the film. 28

Figure II-4 The magnetic hysteresis loops of YIG film (before parameters optimization) with different annealing temperatures in oxygen for 6 hours. The optimal annealing temperature was determined to be 800°C. The curves are offset for clear comparison. .. 29

Figure II-5 With optimal growth parameters, high quality as-grown YIG films were obtained. (a) The color of as-grown film is light yellow, suggesting crystalline growth. (b) The magnetic hysteresis loop shows magnetic moment of as-grown film is the same as post-annealed at 800 °C. 30

Figure II-6 With optimal growth parameters, RHEED patterns before (left) and after (right) deposition of YIG on GGG(110) are consistent, suggesting epitaxial growth of YIG on GGG(110). 30

Figure II-7 With optimal growth parameters, RHEED intensity oscillations suggest layer-by-layer growth mode during YIG/GGG(110) deposition. Each period of the oscillation corresponds to one mono-layer (1/4 unit cell) of YIG, with full coverage at peaks and half coverage at valleys. 31

Figure II-8 With optimal growth parameters, (a) RHEED pattern and (b) RHEED intensity oscillations demonstrate high quality layer-by-layer epitaxy deposition of YIG/GGG(111) thin films. 31

Figure II-9 Clear atomically flat terraces of YIG/GGG(110) were shown by AFM topography image (left) and cross-section of the steps (right). The height of each step (monolayer) is 4.38 Å, which agrees with YIG lattice constant (12.376 Å/4* $\sqrt{2}$ = 4.375 Å) 32

Figure II-10 AFM images of atomically flat terraces on YIG/GGG(111). 33

Figure II-11 In-plane and out-of-plane magnetic hysteresis loops of YIG/GGG(110) thin film at 300K. The magnetization has in-plane easy axis. Inset: Zoom in of in-plane magnetic moment. 33

Figure II-12 (a) The saturated magnetic moment of YIG film decreased by about 30% at room temperature from low temperature (25 K). (b) The coercive field of YIG film was almost independent of temperature. 34

Figure II-13 In-plane angular dependence of magnetic remanence and coercive field of YIG/GGG(110) shows in-plane magnetic anisotropy. 35

Figure III-1 Illustration of the three main mechanisms that can give rise to AHE. [Nagaosa *et al.*, 2010] 39

Figure III-2 Typical AHE measurements of Fe_3O_4(53nm)/MgO(100). 40

Figure III-3 Typical ANE measurements of $Ga_{1-x}Mn_xAs$ (x=0.04-0.07). [Pu *et al.*, 2008] 42

Figure III-4 Illustration of Hall effect (top) and spin Hall effect (bottom) in conductive sample with electron-like charge carriers. [Hirsch, 1999] 43

Figure III-5 Experimental demonstrations of SHE (left) [Kato *et al.*, 2004] and ISHE (right) [Kimura *et al.*, 2007]. 44

Figure III-6 Illustration of the SSE induced by temperature gradient ∇T in the plane of the NiFe film, and the ISHE induced by Pt wires attached to the end of the film. J_s and E_{SHE} denote the spin current and ISHE voltage respectively. And the spin polarization direction σ lies along the direction of magnetic field H, which is in the film plane. [Uchida *et al.*, 2008] 46

Figure III-7 Illustration of conventional (transverse) SSE setup (top) and longitudinal SSE setup (bottom). Here, ∇T, M, Js, and E_{ISHE} denote the temperature gradient, the

magnetization of ferromagnet (F), the spatial direction of spin current across the F/normal metal (N) interface, and the electric field generated by ISHE in N, respectively. [Uchida *et al.*, 2010] 47

Figure III-8 Schematic illustration of the Pt-film/YIG-slab sample in (a) the in-plane magnetized (IM) configuration and (b) the perpendicular-magnetized configuration. In IM configuration, both the longitudinal SSE and proximity ANE are possible to contribute to the signal. In PM configuration, only proximity ANE is possible. [Kikkawa *et al.*, 2013] 49

Figure III-9 Schematic diagram of the patterned Hall bar for induced magneto-transport experiments. 51

Figure III-10 Schematic diagram of Hall bar device fabrication by etching method. 53

Figure III-11 In-plane low-field MR of Pd(2 nm)/YIG (red squares), MR of Cu/YIG reference sample (black squares), and in-plane hysteresis loop (blue squares). The positions of MR peaks are the same as the coercivity of YIG film. 55

Figure III-12 Low-field MR of Pt(2nm)/YIG with (a) in-plane and (b) perpendicular magnetic field. The transverse MR is offset for clearance. 55

Figure III-13 Temperature dependence of MR ratio of Pd(2 nm)/YIG. 56

Figure III-14 Thickness dependence of (a) MR and (b) Hall resistance of Pd(x nm)/YIG. (c) MR ratio as function of inverse 2D density shows interfacial effect. 57

Figure III-15 (a) In-plane and (b) out-of-plane high-field MR of Pd(2nm)/YIG at different temperatures. The MR of two magnetic field directions are similar. 58

Figure III-16 (a) MR ratio at H=10 kOe as a function of temperature. Red and blue regions represent positive and negative MR ratios respectively. The devices with different thickness of Pd layer show similar behavior. 59

Figure III-17 (a) Out-of-plane high-field MR of Pt(2nm)/YIG at different temperatures. (b) Temperature dependence of MR ratio at H=10 kOe for different thickness of Pt layer. 60

Figure III-18 (a) Hall Resistance of Pd(2nm)/YIG at different temperatures without linear background removal. (b) Temperature dependence of longitudinal resistance at zero field and carrier density calculated from ordinary Hall resistance. 61

Figure III-19 Field dependence of the AHE-like Hall resistance R_H of Pd(2nm)/YIG at different temperatures with linear background removal. Lines are the Brillouin function

fits. Inset: Normalized R_H as a function of B/T shows changing total angular momentum at different temperatures. 62

Figure III-20 Temperature dependence of *gJ* (red solid squares) and the saturation AHE-like signal (blue solid circles) obtained from the Brillouin fitting. Lines are guides to the eyes. 63

Figure III-21 Pd thickness dependence of the Hall resistance R_H at T=5 K. The inset shows the zoom-in data for Pd thicknesses from 4 to 10 nm..... 64

Figure III-22 AHE-like resistivity as a function of temperature for different thickness of Pd layer..... 64

Figure III-23 AHE-like signal for several reference samples at T=5 K. All metal layers (except the Cu-layer in Pd/Cu/YIG) are 2 nm thick. The inset shows zoom-in data for reference samples. 65

Figure III-24 (a) Field dependence of the Hall resistance R_H of Pt(2nm)/YIG at different temperatures with linear background removal. (b) AHE-like resistivity as a function of temperature for different thickness of Pt layer. 66

Figure III-25 Resistivity of Pd(2nm)/YIG at low temperatures as a function of log(T). The inset shows the full range temperature dependence. The Kondo-like effect is enhanced after annealing..... 67

Figure III-26 Hall resistivity as a function of longitudinal resistivity. 68

Figure IV-1 In-plane rotation AMR (black) and PHE of MgO(4nm)/Ni(10nm)/MgO(001) with current along <100> direction and magnetic field H=10 kOe. 71

Figure IV-2 Illustration of the mechanism of SMR. (a), (b) and (c) Illustration the magnetic control of the electrical conductivity of non-magnetic metal (N) by SHE/ISHE with strong spin-orbit interaction. (d) and (e) Illustration the geometric relation between the magnetization *M* in the magnetic insulator (F) and the spin current J_s, and the additional charge current J_e due to ISHE (f) Illustration the spin accumulation due to SHE in N. [Nakayama *et al.*, 2013]..... 73

Figure IV-3 Schematic diagram of the patterned Hall bar and notations for field rotations for AMR/SMR experiments. 76

Figure IV-4 Schematic diagram of Hall bar device fabrication by lift-off method. 77

Figure IV-5 Low-field MR (black) and Hall resistance (blue) of Pd(2nm)/YIG with magnetic field applied in directions of (a) longitudinal, (b) transverse. 79

Figure IV-6 Comparison of two sets of typical field rotation data of Pd(2 nm)/YIG in three orthogonal planes (upper: H=10 kOe, T=100 K; lower: H=100 kOe, T=3 K). The notations α, β and γ denote xz-, yz- and xy-plane rotation. 80

Figure IV-7 Typical field rotation data of Pd(2 nm)/YIG at high-field (100 kOe) and low-temperature (3 K) in three orthogonal planes: (a) xz-plane (AMR); (b) yz-plane (SMR); and (c) xy-plane (combined). The longitudinal resistance is shown in black and transverse (Hall) resistance is shown in blue. 82

Figure IV-8 Rotation data from two perpendicular devices of Pd(2 nm)/YIG on the same chip are consistent (H=100 kOe, T=100 K). It indicates the rotation MR depends on the direction of magnetic moment, not the crystalline orientation of YIG film. 83

Figure IV-9 Low-field (10 kOe) rotation MR of Pd(2 nm)/YIG at different temperatures in three orthogonal planes: (a) xz-plane (AMR); (b) yz-plane (SMR); and (c) xy-plane (combined). 85

Figure IV-10 Temperature dependence of low-field (10 kOe) rotation MR ratio of Pd(2 nm)/YIG. 86

Figure IV-11 High-field (100 kOe) rotation MR of Pd(2 nm)/YIG at different temperatures in three orthogonal planes: (a) xz-plane (AMR); (b) yz-plane (SMR); and (c) xy-plane (combined). 87

Figure IV-12 Temperature dependence of high-field (100 kOe) rotation MR ratio of Pd(2 nm)/YIG. 88

Figure IV-13 Pt(2 nm)/YIG temperature dependence of high-field (100 kOe) rotation MR ratio. Inset: High-field (100 kOe) rotation in xz- and yz-plane at 3 K. 89

Figure IV-14 Field dependence of rotation MR of Pd(2 nm)/YIG at 3K in (a) xz-plane (AMR) and (b) yz-plane (SMR). 90

Figure IV-15 Field dependence of MR ratio of Pd(2 nm)/YIG at 3 K. 91

Figure V-1 Overview of LIMs, the sub-systems are shown in sub folders. 94

Figure V-2 LIMs sub-system of <sys> includes system level interfaces supporting instruments drivers. 95

Figure V-3 LIMs sub-system of <math> includes mathematical library supporting experiments. 95

Figure V-4 LIMs sub-system of <util> includes procedure level utility library. 96

Figure V-5 LIMs sub-system of <instr> includes all drivers of the supported instruments. 96

Figure V-6 LIMs sub-system of <proc> includes the basic procedures and functions for projects. 97

Figure V-7 LIMs sub-system of <~proj> includes experiment project level codes and information. 98

List of Tables

Table I-1 Growth Parameters of LSMO/STO(110) by PLD 11

Table I-2 Growth Parameters of Fe_3O_4/MgO(100) by PLD 19

Table II-1 Growth Parameters of YIG films by PLD 37

Table III-1 Sputter deposition parameters 52

Chapter I

Magnetic Thin Film Growth and Characterization

1.1 Pulsed Laser Deposition

Pulsed Laser Deposition (PLD) has been regarded as a versatile physical vapor deposition (PVD) technique in thin film deposition [1–5], compared to other techniques such as e-beam evaporation and sputtering deposition. In a general PLD system, a high-power pulsed laser beam is focused into a vacuum chamber, strikes the target material which is to be deposited, and vaporizes the material from target as a plasma plume. The material vapor is then deposited onto the substrate as a thin film. Depending on the material to deposit, the chamber during the growth can be either in ultra high vacuum (UHV) or in the present of a background gas, such as oxygen commonly used to maintain oxygen stoichiometry in oxide deposition. The schematic illustration of PLD system is shown in Figure I-1. A reflection high-energy electron diffraction (RHEED) system is included for real-time growth monitoring.

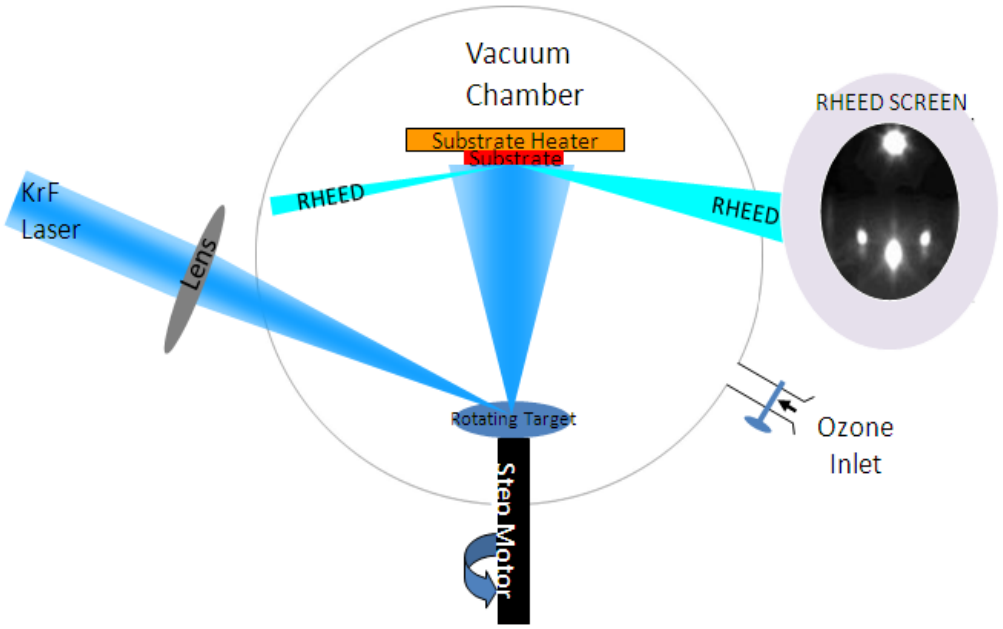


Figure I-1 Schematic illustration of Pulsed Laser Deposition system.

Our homemade PLD system is shown in Figure I-2. The UHV chamber, with ozone capability and 4 rotating targets controlled by step motors, can reach a base pressure up to $8x10^{-8}$ Torr. A KrF excimer laser (Coherent COMPexPro 102F) that works at 248nm is used as the ablation source. The laser pulse length is 10-50 ns, the maximum pulse power is 200 mJ per pulse, and the maximum repetition rate is 20 Hz. A STAIB RHEED system is used for real-time growth monitoring, with the highest electron energy of 30 keV. The RHEED system is configured with a differential pumping stage to accomplish oxide growth in ambient pressure of oxygen up to 100 mTorr, as shown in Figure I-3.

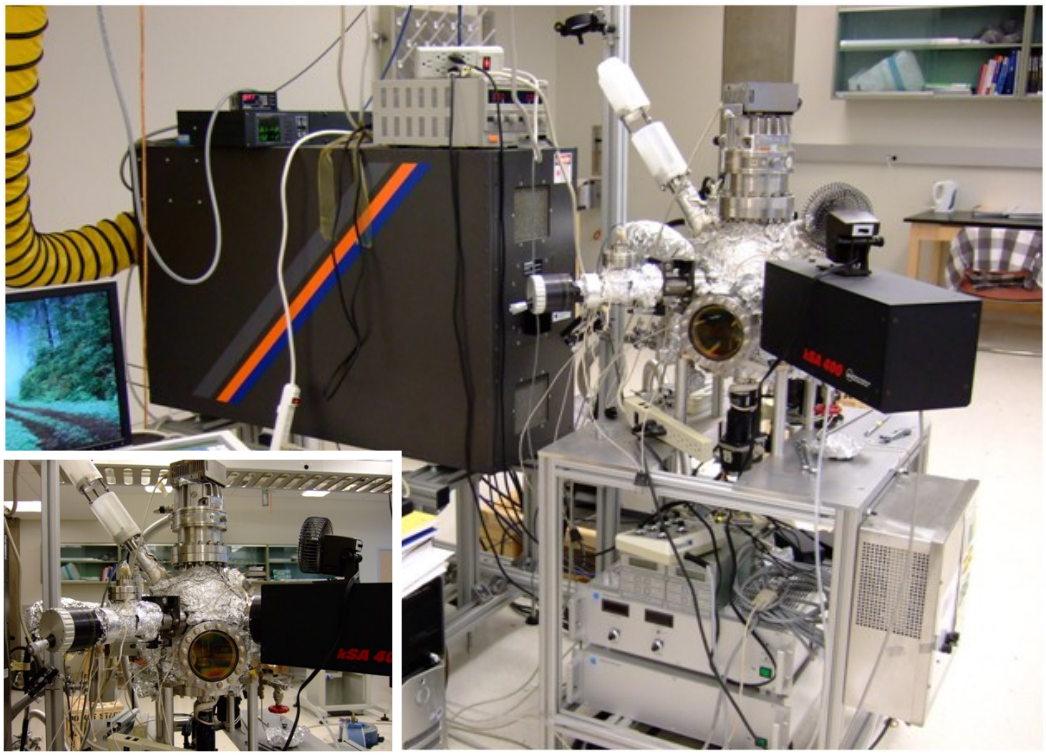


Figure I-2 Picture of our homemade PLD system. Inset: Zoom view of the main UHV chamber.

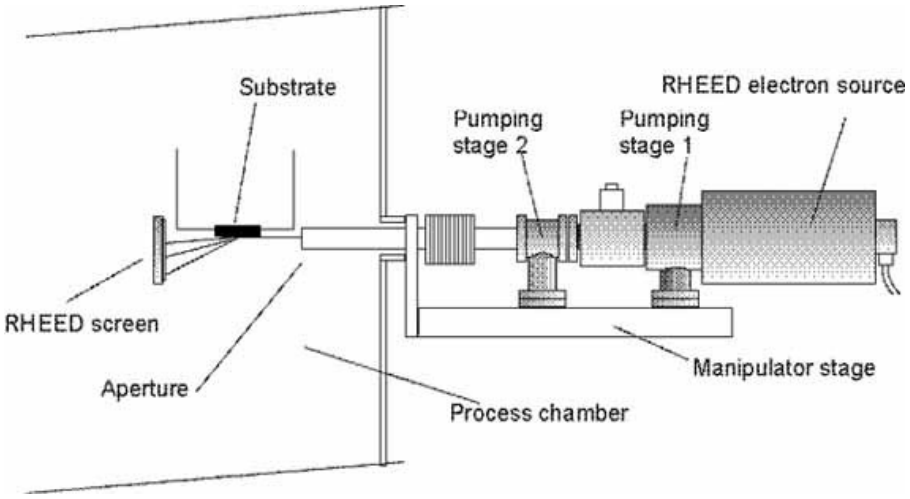


Figure I-3 Schematic illustration of STAIB® RHEED system with differential pumping stage. [staibinstruments.com]

Comparing to other thin film deposition techniques, especially molecular beam epitaxy (MBE), the basic setup of PLD is relatively simple while the quality of the grown film is very high, in addition to other advantages. PLD systems can utilize non-volatile, multi-component ceramics targets and multi-targets for multi-layer or alloy films, with small target size and stoichiometry transfer from target to deposit film. Furthermore, PLD systems can operate under any ambient gas, and generally low substrate temperature, with reasonable growth rate, which is important in oxide growth particularly. On the other hand, PLD has some disadvantages such as small growth area, formation of particulates and target surface modification.

The physical process of laser-target interaction and the kinetics of film growth in PLD are quite complex. In general, the process can be divided into four stages and each of these steps is crucial for the crystallinity, uniformity and stoichiometry of the resulting film [6]: (1) target material plasma creation by laser ablation; (2) dynamic evolution of the plasma plume; (3) deposition of the material plume onto the substrate; (4) nucleation and formation of the thin film on the substrate surface. The typical plume of yttrium iron garnet (YIG) target is shown in Figure I-4. The details of PLD growth procedures and parameters of different materials will be discussed later.

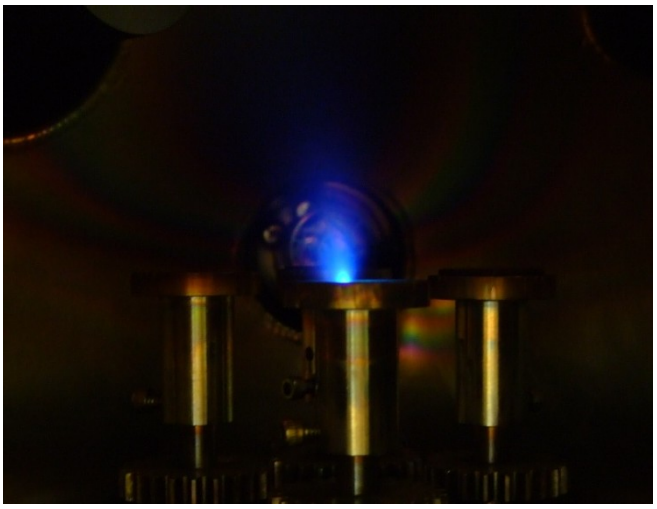


Figure I-4 Plume injected from yttrium iron garnet (YIG) target during the deposition.

1.2 $La_{1-x}Sr_xMnO_3$ (LSMO) Thin Film Preparation and Property Measurements

Transition metal oxides have been extensively studied in the past decades due to their rich crystallographic, electronic and magnetic properties [7–9]. Among the various transition metal oxides, $RaMnO_3$ manganite has particular study interests due to its strong electron-electron interaction, electron-lattice coupling and rich magnetic properties under proper doping. The $RaMnO_3$ manganite has a perovskite lattice structure, as shown in Figure I-5, where 8 rare earth element atoms Ra (green) are at the corner of the cubic unit cell, 6 oxygen atoms (red) are in the center of the six faces, and manganese atom Mn (purple) is at the cubic center. Clearly, manganite has a layered structure feature along the cubical axis with a stacking sequence of RaO and MnO_2.

The alkali metal Sr-doped $La_{1-x}Sr_xMnO_3$ (LSMO), is extensively studied recently for its relatively high Curie temperature (T_C) and ease of epitaxial growth [10]. By choosing proper growth parameters, LSMO films will have 100% spin polarization [11] due to double exchange [12–15]. The ferromagnetic state with highest T_C=370K is achieved at optimal Sr doping level x=0.33, which is the object in this section.

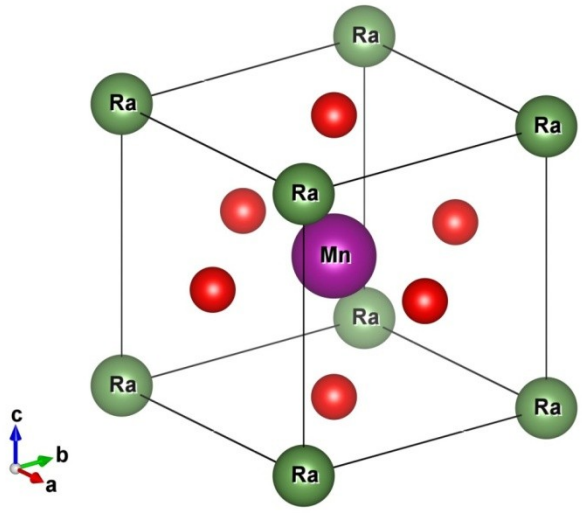


Figure I-5 Schematic illustration of a unit cell of $RaMnO_3$ in real space. The rare-earth Ra atoms are at the corners with one Mn atom at the center of the cubic. Six oxygen atoms are at the center of the faces.

The nominal composition of $La_{0.67}Sr_{0.33}MnO_3$ target was prepared by solid phase synthesis. The stoichiometric ratio (molar ratio 0.335:0.33:1) of La_2O_3 (≥99.99%), $SrCO_3$ (≥99.99%) and MnO_2 (≥99.997%) powders were mixed in isopropyl alcohol with intermediate grindings for 2 hours. The mixture was heated up at 1000 °C for 48 hours to form single phase LSMO powders. To make LSMO targets, the powders were pressed

into pellets and sintered at 1200 °C for 72 hours in air. The target was put on a rotation holder controlled by a step motor with 3 degrees/second rotating speed, to minimize target surface modification.

The commercial available (110)-orientation $SrTiO_3$ (STO) substrates from Crystec were chosen for LSMO growth as the lattice (3.905 Å for STO and 3.876Å for LSMO) matches very well. The substrates were ultrasound cleaned in acetone for 15 minutes, chemically etched by buffered oxides etchant (BOE) and annealed in oxygen at 850 °C for 12 hours, to obtain high quality Ti-O terminated surface with atomically flat terraces. Prior to growth, the substrates were baked in the UHV chamber at about 200 °C with base pressure of $8x10^{-8}$ Torr overnight and *in-situ* annealed at 800 °C ~ 850 °C in $7x10^{-3}$ Torr of oxygen for 30~60 minutes. With this substrate treatment procedure, a sharp RHEED pattern was observed as shown in Figure I-6(a), indicating high crystallinity and flat STO(110) surface. The LSMO film can be easily epitaxially grown on such substrates.

During the growth, the substrate temperature was kept at 800 ~ 850 °C, which has a great influence on the film crystallinity. And the chamber was filled with $7x10^{-3}$ Torr of oxygen with 12 wt% of ozone. Because of the chemically active ozone, the as-grown LSMO films have very good oxygen stoichiometry without employing high pressure of oxygen

reported by other groups (~ 100 mTorr). The LSMO films produced have little oxygen deficiency and high T_C in the as-grown state.

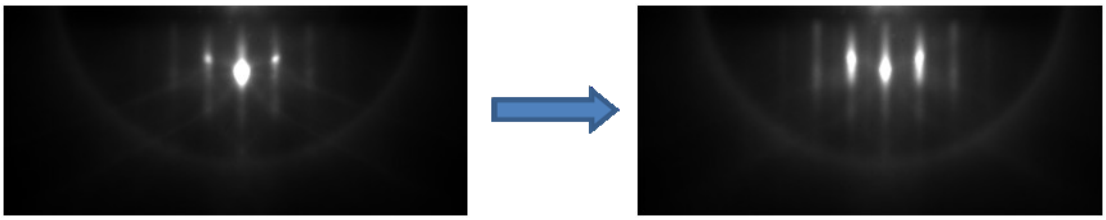


Figure I-6 RHEED patterns before (left) and after (right) deposition of LSMO on STO(110) are consistent, suggesting epitaxial growth of LSMO on STO(110).

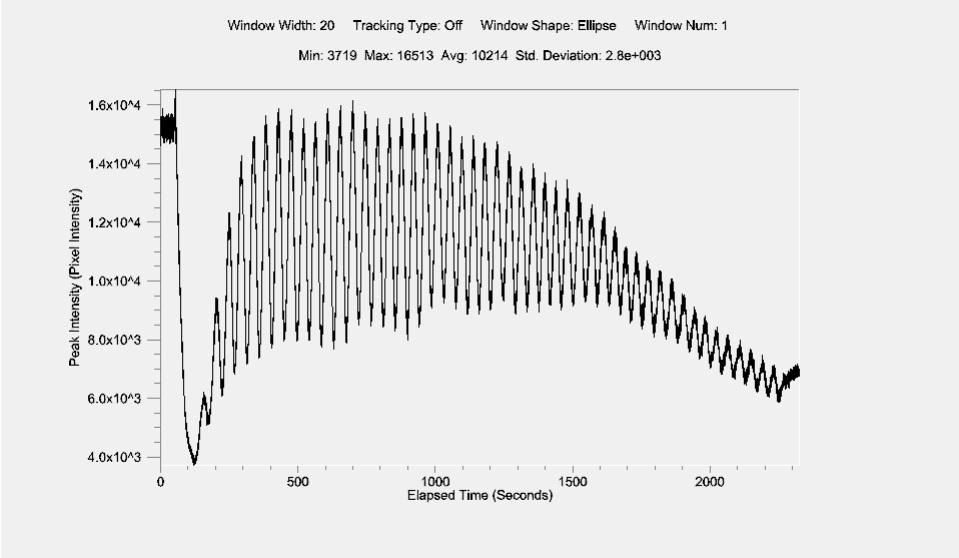


Figure I-7 RHEED intensity oscillations suggest layer by layer growth mode during LSMO/STO(110) deposition. Each period of the oscillation corresponds to one mono-layer of LSMO, with full coverage at peaks and half coverage at valleys.

To fully excite the target material plasma with good stoichiometry and target material flux density, the laser parameters are critical. The laser power was set to around 160 mJ per pulse and the repetition rate was 1-3 Hz. Under this condition, the laser molecular

beam epitaxy (Laser MBE) was achieved as shown in Figure I-6(b), and a well defined layer-by-layer growth mode was obtained as indicated by RHEED intensity oscillations shown in Figure I-7. The diffraction of the electrons reflected from the surface of the film is maximized (minimized) when the surface is fully-covered (half-covered) by single crystalline neutral layer of the material, thus each oscillation of the RHEED intensity corresponds to one mono-layer of LSMO. And such layer-by-layer structure can be clearly seen in the LSMO/STO superlattice samples by high resolution transmission electron microscopy (HRTEM) as shown in Figure I-8.

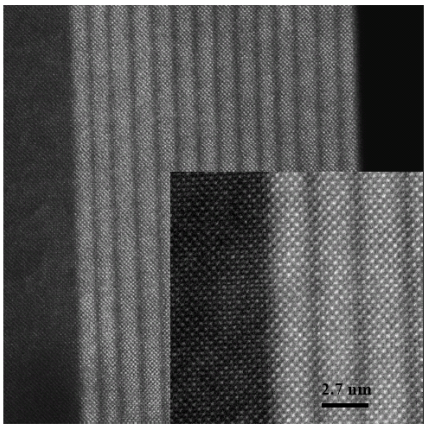


Figure I-8 HRTEM image of [LSMO(7ML)/STO(3ML)]$_{14}$/STO(110) superlattice sample with 14 periodic units in full range. The inset shows high resolution image near substrate. The dark and bright part corresponds to STO and LSMO layers respectively.

The growth condition of LSMO films was optimized that the Curie temperature T_C is about 340 K and the saturation magnetic moment M_s is about 3.7 μ_B/Mn in the as-grown state. The in-plane magnetism of film grown is shown in Figure I-9.

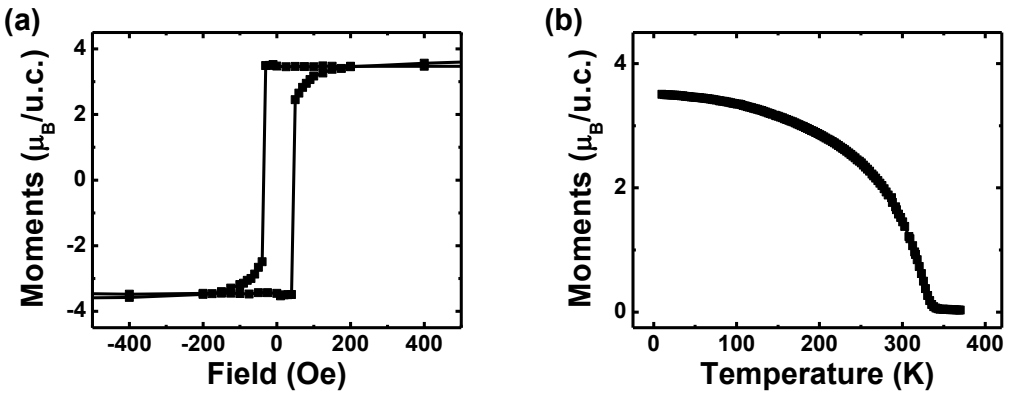


Figure I-9 (a) In-plane magnetic hysteresis loops of LSMO/STO(110) at 5K. (b) Temperature dependence of in-plane saturate magnetic moments of LSMO/STO(110).

The temperature dependence of LSMO film resistivity is shown in Figure I-10. Clearly, the film grown has a metallic behavior with the resistivity of about 8 mΩcm at room temperature, which is consistent with the reported value [15].

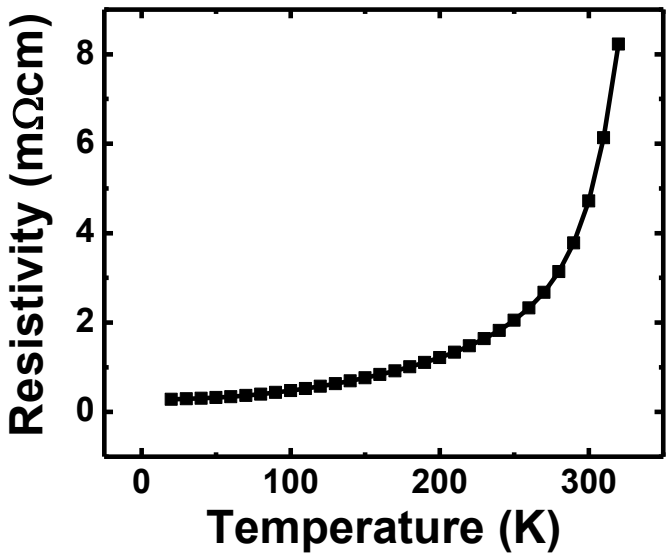


Figure I-10 Temperature dependence of resistivity of LSMO/STO(110) at zero field.

Furthermore, the in-plane magnetoresistance of LSMO/STO(110) thin film at different temperatures was studied and shown in Figure I-11(a). The MR ratio at 10 kOe, i.e. $MR = \frac{R(H)-R(H=0)}{R(H=0)}$, decreases when the temperature decreases, which is summarized in Figure I-11 (b).

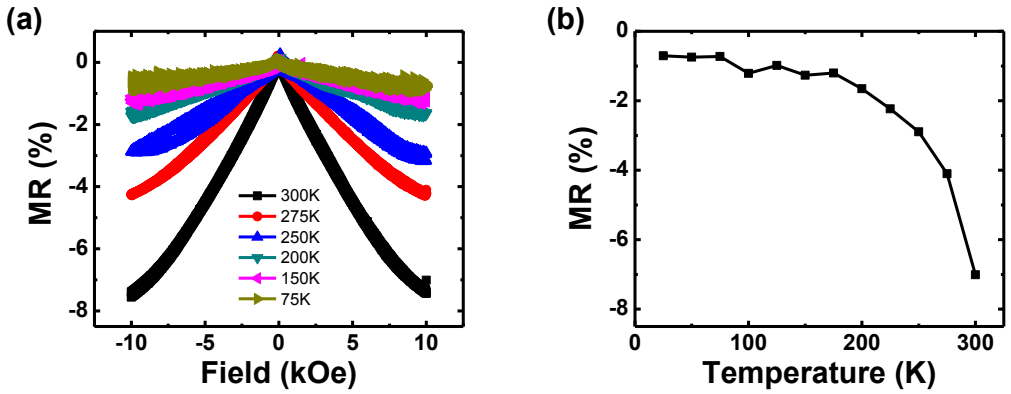


Figure I-11 (a) In-plane magnetoresistance of LSMO/STO(110) as function of field at different temperatures. (b) Temperature dependence of MR ratio (H = 10 kOe).

The growth parameters of LSMO/STO are summarized in Table I-1.

Substrate treatment	Chemical etching; annealing in oxygen at 850 °C for 12 hours
Base pressure	Better than $6x10^{-7}$ Torr
Background gas	0.7 mTorr of oxygen with 12 wt% of ozone
Substrate temperature	800 °C ~ 850 °C
Laser energy	160 mJ per pulse
Laser repetition rate	1~3 Hz
Surface coating	N/A

Table I-1 Growth Parameters of LSMO/STO(110) by PLD

1.3 Fe_3O_4 Thin Film Preparation and Measurements

Considerable interest has been focused on half-metallic materials with 100% spin polarization of the charge carriers at the Fermi level, due to their potential applications in spintronics. Among many candidates (e.g. magnetite, CrO_2, Mn based Heusler alloy, doped manganite, and double perovskite), magnetite (Fe_3O_4) has high Curie temperature (T_C ~ 850 K), low magneto-crystalline anisotropy, and relative low growth temperature with high film quality, which is compatible with semiconductor spintronics device integration. Great effort has been made to grow Fe_3O_4 films by PLD on different substrates with and without a buffer layer [16–21], and successful layer-by-layer epitaxial growth was reported with four molecular layers per unit cell [22].

Fe_3O_4 belongs to cubic ferrite family, with an inverse spinel crystallographic structure (lattice constant=8.397 Å), as shown in Figure I-12, which includes a face-centered-cubic (fcc) oxygen lattice, and the tetrahedral (8-fold) positions are occupied by Fe^{3+} cations, while octahedral (16-fold) positions are equally occupied by Fe^{3+} and Fe^{2+} cations. Each unit cell of Fe_3O_4 consists of 8 formula units. It is ferrimagnetic at room temperature, with 4 μ_B per formula unit predicted.

It has attracted extensive research interests of the magnetic and transport properties of Fe_3O_4, especially for the understanding of the Verwey transition [23,24], and for studying the scaling relation of the anomalous Hall effect (AHE) in the so-called dirty

regime [25–28]. For general consideration, AHE conductivity is known to yield a relation of $\sigma_{xy} \propto \sigma_{xx}$ or $\sigma_{xy} = const$ in clean and intermediate regimes, where the longitudinal conductivity $\sigma_{xx} > 10^6\ \Omega^{-1}\text{cm}^{-1}$ or $\sigma_{xx} > 10^4\ \Omega^{-1}\text{cm}^{-1}$ respectively. The details of AHE will be discussed in §3.1.1. In the dirty regime ($\sigma_{xx} < 10^4\ \Omega^{-1}\text{cm}^{-1}$), a relation $\sigma_{xy} \propto \sigma_{xx}^{1.6}$ is predicted due to the damping of the intrinsic contribution [29], which agreed with our experimental data.

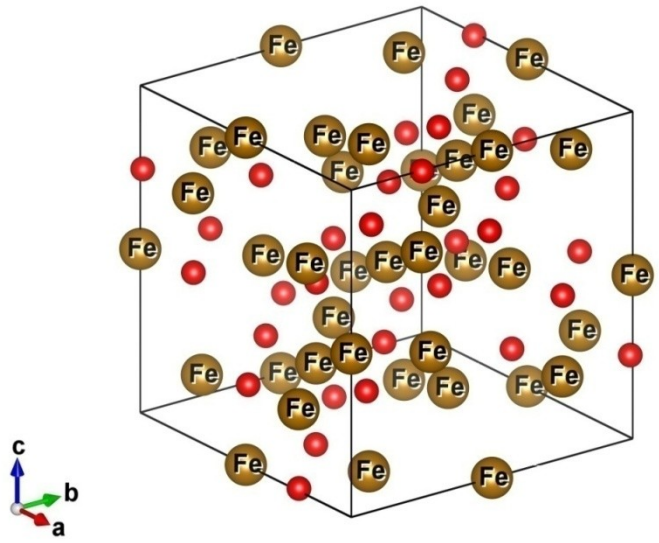


Figure I-12 Schematic illustration of a unit cell of Fe_3O_4 in real space.

The Fe_3O_4 and Fe_2O_3 targets were prepared from commercial available stoichiometric powders (≥99.997%). The powders were intermediately grinded in isopropyl alcohol for 30-60 minutes, and then pressed into pellets and sintered at 900 °C for 48 hours in air. The target was put on a rotation holder controlled by a step motor with 5 degrees/second

rotating speed, to minimize target surface modification. It is interesting that both Fe_3O_4 target and Fe_2O_3 target will produce Fe_3O_4 films with the optimal growth parameters below, while the stoichiometry is still good.

The commercially available (100)-orientation MgO substrates from SPI Supplies were chosen for Fe_3O_4 growth, as the lattice constant of Fe_3O_4 (8.397 Å) matches twice of MgO (4.212 Å) and they are both inverse spinel cubic structure, so it is preferable in epitaxial growth. The substrates were ultrasound cleaned in isopropyl alcohol for 15 minutes and then immediately placed into the UHV chamber. Prior to growth, the substrates were baked in the UHV chamber at about 200 °C with a base pressure of $8x10^{-8}$ Torr overnight and *in-situ* annealed at 800 ~ 850 °C for about 2 hours in 1 mTorr of oxygen to avoid oxygen deficiency and improve the surface crystallinity. With this substrate treatment procedure, a sharp RHEED pattern was observed as shown in Figure I-13(a), indicating high crystallinity and flat MgO(100) surface. During the growth, the substrate temperature was kept at 400 °C ~ 450 °C, which is optimal for epitaxial film growth. And the chamber was pumped to a high vacuum of better than $2x10^{-7}$ Torr.

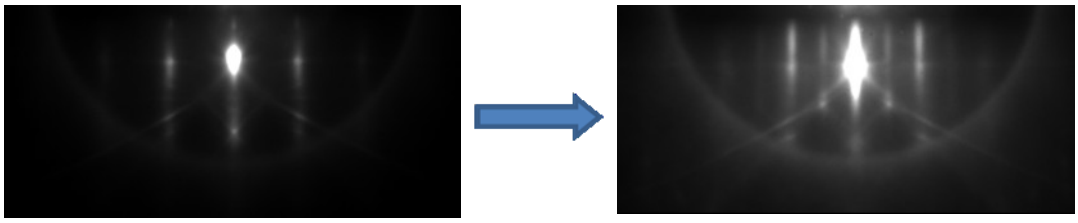


Figure I-13 RHEED patterns before (left) and after (right) deposition of Fe_3O_4 on MgO(100) are consistent, suggesting epitaxial growth of Fe_3O_4 on MgO(100).

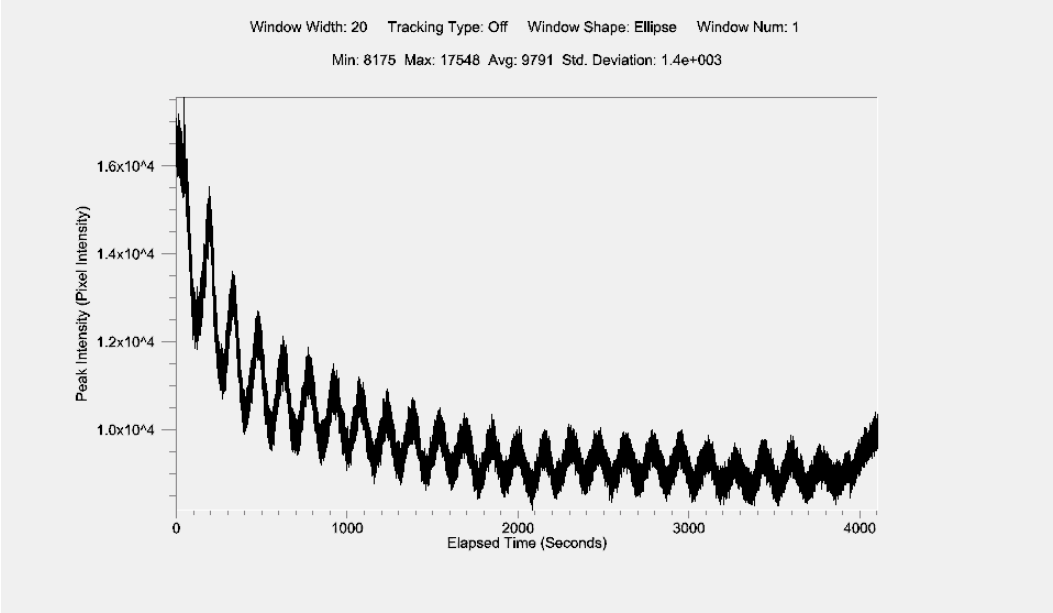


Figure I-14 RHEED intensity oscillations suggest layer-by-layer growth mode during Fe_3O_4/MgO(100) deposition. Each period of the oscillation corresponds to one mono-layer (1/4 unit cell) of Fe_3O_4, with full coverage at peaks and half coverage at valleys.

The laser power was set to around 180 mJ per pulse and the repetition rate was 5-10 Hz. These parameters are optimized for stoichiometry and epitaxial growth. Under this condition, the laser molecular beam epitaxy (Laser MBE) was achieved as shown in Figure I-13(b). Note that the lattice constant of Fe_3O_4 is twice of MgO substrate, thus additional patterns appear in the center of each strips corresponding to MgO lattice,

which suggests the Fe_3O_4 lattice formation of the film. The layer-by-layer growth mode was obtained as indicated by RHEED intensity oscillations shown in Figure I-14. Be noted that in the Fe_3O_4 growth, there are four oscillations per unit cell [22]. Each building block of the molecular layer consists the composition of $Fe(A)_2^{3+}Fe(B)_2^{3+}Fe(B)_2^{2+}O_8^{2-}$, and cannot be mapped onto each other by lattice translation. The letters A and B refer to the tetrahedral A-site and the octahedral B-site. After the growth of Fe_3O_4 film, the film was covered by 4-10 nm thick STO cap layer in order to prevent surface oxidation.

The growth condition of Fe_3O_4 films were optimized that the saturation magnetic moment M_s is about 3.6 μ_B per formula unit at room temperature. The in-plane and out-of-plane magnetic moment hysteresis loops are shown in Figure I-15, and clear in-plane anisotropy of the magnetism was observed.

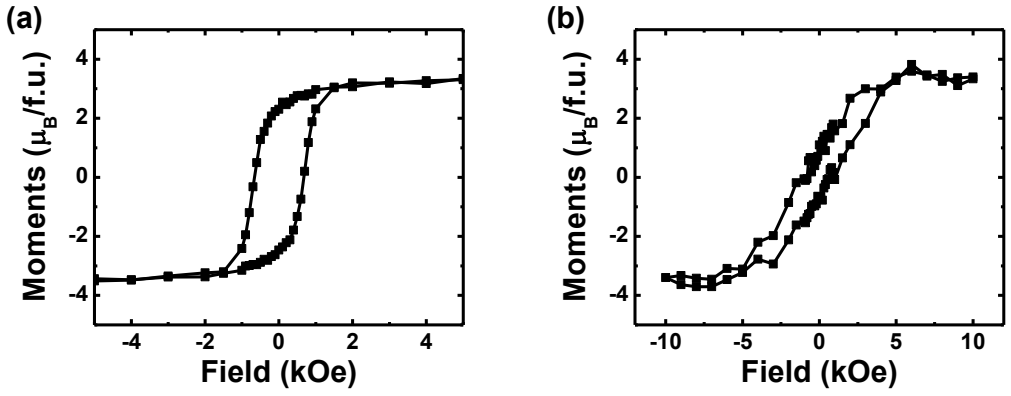


Figure I-15 (a) In-plane and (b) out-of-plane magnetic hysteresis loops of Fe_3O_4/MgO(100) thin film at 300K. The magnetization has in-plane anisotropy.

The temperature dependence of Fe_3O_4 film resistivity is shown in Figure I-16 and a semiconducting behavior of the resistivity is observed in the film as occurs in the bulk samples. By fitting the temperature dependence of resistance to general semiconducting samples $\rho \propto exp(E_{gap}/k_BT)$, the band gap of the Fe_3O_4 film is determined to be about 60 meV, which agrees with the reported value of 100 meV. The Verwey transition is imperceptible in the epitaxial thin films (<20 nm), which has been associated to the stress caused by the substrate and the inhibition of long range order for ultrathin films, as a consequence of the high density of antiphase boundaries [28,30,31].

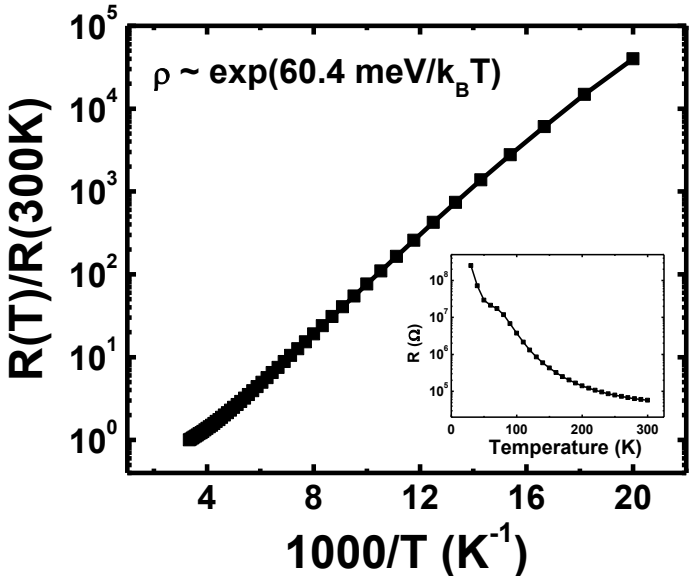


Figure I-16 Normalized resistivity of Fe_3O_4/MgO(100) thin film as a function of inversed temperture. Inset: Temperature dependence of resistance of Fe_3O_4/MgO(100) thin film.

Furthermore, the magnetoresistance and anomalous Hall effect of Fe_3O_4/MgO(100) thin film at different temperatures were studied and shown in Figure I-17. It is clear that both the MR ratio at 10 kOe and AHE resistance increase when the temperature decreases.

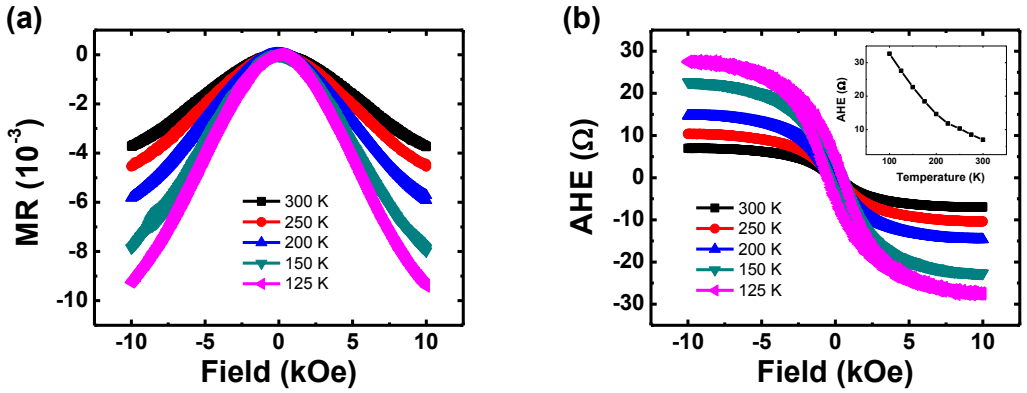


Figure I-17 (a) Magnetoresistance and (b) anomalous Hall effect of Fe_3O_4/MgO(100) thin film at different temperatures. Inset: Temperature dependence of AHE resistance.

The longitudinal conductivity and anomalous Hall conductivity are calculated as $\sigma_{xx} = \frac{\rho_{xx}}{\rho_{xx}^2+\rho_{xy}^2}$ and $\sigma_{xy} = \frac{\rho_{xy}}{\rho_{xx}^2+\rho_{xy}^2}$ respectively, and the scaling of the logarithm of the two conductivities is plot in Figure I-18. Four different samples and one with different driven current are shown. It is shown that $\sigma_{xy} \propto \sigma_{xx}^{1.68}$ in our samples, which agree well with the predicted value of $\sigma_{xy} \propto \sigma_{xx}^{1.6}$ in the dirty regime.

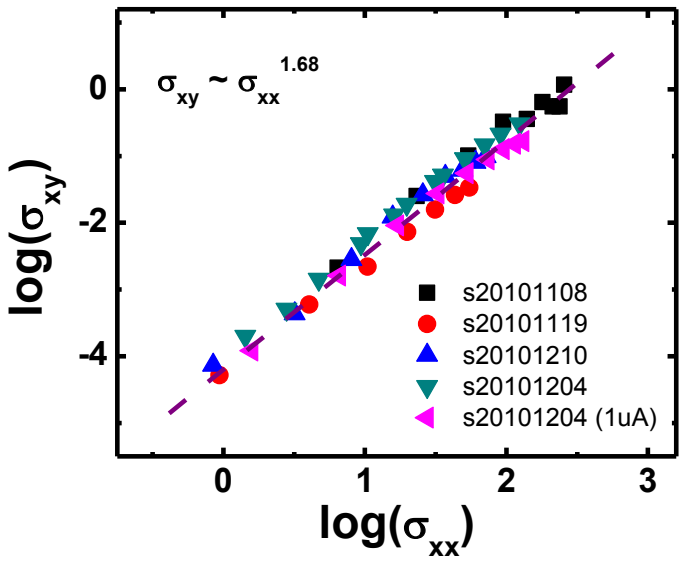


Figure I-18 Scaling of longitudinal conductivity and anomalous Hall conductivity. The typical driven current is 100 nA except one indicated.

The growth parameters of Fe_3O_4/MgO are summarized in Table I-2.

Substrate treatment	*In-situ* annealing in oxygen at ~800 °C for 2 hours
Base pressure	Better than $2x10^{-7}$ Torr
Background gas	None
Substrate temperature	400 °C ~ 450 °C
Laser energy	180 mJ per pulse
Laser repetition rate	5~10 Hz
Surface coating	STO

Table I-2 Growth Parameters of Fe_3O_4/MgO(100) by PLD

1.4Discussion

PLD is a powerful tool in thin film deposition, especially for complex magnetic oxides. The convenience of stoichiometry transfer and ambient gas pressure provides a unique capability to control the multi-components of the depositing material and allows easily

multi-layer or superlattice structure of the thin film. By carefully tuning the growth parameters, laser MBE mode can be obtained and very often layer-by-layer growth can be achieved, which is preferable in high quality magnetic oxides thin film growth and characterization. Some critical parameters in the growth include substrate surface morphology, background pressure, substrate temperature and laser energy. Typically, the surface flatness and crystallinity condition determines the nucleation process and growth of film, and single crystal substrates with atomically flat terraces from small mis-cut are used in our study. The background pressure and laser energy are critical in film stoichiometry, especially for oxygen deficiency of oxides. Low laser energy could result in off-stoichiometry of the film deposited. The substrate temperature, along with other factors, is important in film crystallinity and the growth mode (layer-by-layer, step-flow and island-formation).

In this chapter, it is demonstrated that single crystal LSMO films on STO and Fe_3O_4 films on MgO were successfully grown epitaxially in layer-by-layer mode, with parameters discussed. The magnetic and transport characteristics of the films were performed and showed that the films are of very high quality in crystallinity and magnetic properties. The technique developed allows us to prepare and study complex magnetic oxides films and spin-related devices based on the films. In the following chapters, the growth of magnetic insulators, especially yttrium iron garnet (YIG) films, will be discussed. And

based on YIG films, the non-magnetic metal / magnetic insulator structure devices were fabricated and the induced magneto-transport effects were explored, including induced magnet moments at the interface and spin Hall magnetoresistance effect.

Chapter II

Yttrium Iron Garnet Thin Film Growth

2.1 Introduction

Magnetic garnet thin films have attracted increasing interests in both fundamental research and device applications in the past few decades. The large class of iron garnet oxides (e.g. $Sr_3Fe_5O_{12}$, $Gd_3Fe_5O_{12}$, $Tb_3Fe_5O_{12}$, $Dy_3Fe_5O_{12}$) with high Curie temperature, especially yttrium iron garnet ($Y_3Fe_5O_{12}$, YIG) and its substitution (Bi:YIG, Ce:YIG et al.), has been applied to integrated magneto-optical devices, high performance nonreciprocal waveguide devices and microwave devices, because of the high Faraday rotation and low propagation loss [32–36]. Recently, the emergence of spintronics using magnetic insulators created a higher demand of YIG films, due to two significant features of YIG films: (1) extremely small intrinsic damping constant and (2) electrically insulating behavior. The damping constant in YIG is about $3x10^{-5}$ [37], which is desirable in spin-torque and spin-wave based devices. The electrically insulating feature enables the research and device applications utilizing pure spin current with lower power consumption, without Joule heating associated with charge currents. The recent pioneering works of spin Seebeck effect, spin Hall magnetoresistance and spin pumping

based on YIG show the importance of the growth of high quality YIG films and surface engineering [38–45].

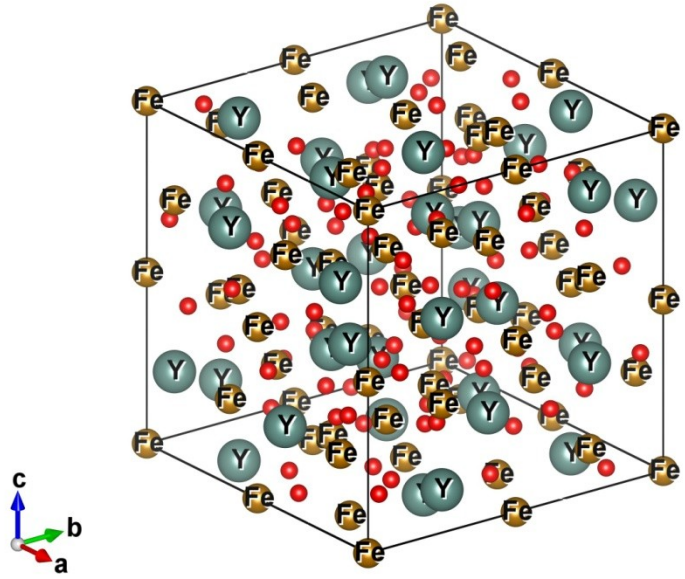


Figure II-1 Schematic illustration of a unit cell of YIG crystal structure in real space.

Garnet materials have a chemical formula of $A_3B_2C_3O_{12}$ with a cubic unit cell of $(A_3B_2C_3O_{12})_8$, where A is a large dodecahedral site, B is a moderately sized octahedral site, and C is a small tetrahedral site. The crystal structure of garnets belongs to the symmetry point group of $Ia\bar{3}d$, and the charge neutrality layer corresponding to each RHEED intensity peak is 1/4 of the unit cell length [46,47]. In YIG, the Fe^{3+} ions on the B and C sites are antiferromagnetically coupled to each other due to superexchange

interaction, which results in a ferrimagnetic state with net magnetic moment equivalent to one Fe^{3+} per formula unit. The crystal structure of YIG is shown in Figure II-1.

YIG films have been fabricated on different substrates by many techniques [37,46–53], including liquid phase epitaxy (LPE), PLD, and radio frequency magnetron sputtering, and the growth parameters have been explored [54–58]. Recently, the layer-by-layer growth of YIG film on gadolinium gallium garnet ($Gd_3Ga_5O_{12}$, GGG) substrate by PLD was realized with high laser repetition rate [47]. On the other hand, it is demonstrated that low laser repetition rate is preferable for high quality growth [37]. It is desirable to understand the effect of the optimal growth parameters.

2.2Sample Preparation and Characterization

The high density YIG targets were prepared from commercially available stoichiometric YIG powders (≥99.9%). The powders were intermediately ground in isopropyl alcohol for 30-60 minutes, and then pressed into pellets and sintered at 1200 °C for 72 hours in oxygen. The target was placed on a rotation holder controlled by a wobble wheel and a step motor with 5 degrees/second rotating speed, to minimize target surface modification. When too many the laser pulses hit the same spot of target, cone-like structure forms on the surface and leads to low deposition efficiency. The target material also tends to be off-stoichiometric due to yttrium enrichment process [59].

The commercially available (110)- and (111)-oriented GGG substrates from MTI were used for YIG growth, as the lattice constant of YIG (12.376 Å) matches GGG (12.383 Å) and it is preferable in epitaxial growth. The substrates were ultrasound cleaned in acetone, isopropyl alcohol and de-ion water for 15 minutes each, and annealed in oxygen at 1000 °C for 6 hours. Prior to growth, the substrates were baked in the UHV chamber at about 200 °C with base pressure of $8x10^{-8}$ Torr overnight. With this substrate treatment procedure, good crystallinity and flat GGG surface is obtained, as discussed later.

During the growth, the substrate temperature was kept at 650 ~ 750 °C, which is found to be optimal for epitaxial YIG film growth. And the chamber was filled with ambient oxygen pressure of $2.2x10^{-3}$ Torr with 12 wt% of ozone. The power of KrF laser (248 nm) was set to around 160 mJ per pulse and the repetition rate was 5-10 Hz. After the growth, the sample was slowly cooled down (≤10 °C /minute) to room temperature in the same oxygen environment. These parameters are optimized for stoichiometry and epitaxial layer-by-layer growth.

The crystalline structure of YIG film was simultaneously monitored by RHEED patterns, and the formation of atomic layers were indicated by intensity oscillations when applicable. The surface morphology was examined by atomic force microscope (AFM) in the tapping or contact mode. The magnetic properties were measured by either vibrating sample magnetometer (VSM) or superconducting quantum interference device (SQUID).

2.3 Optimization of Growth Parameters

2.3.1 Substrate Treatment

A high quality substrate with crystalline and flat surface is essential in epitaxial growth. In this part, different substrate treatments will be discussed, as shown in Figure II-2.

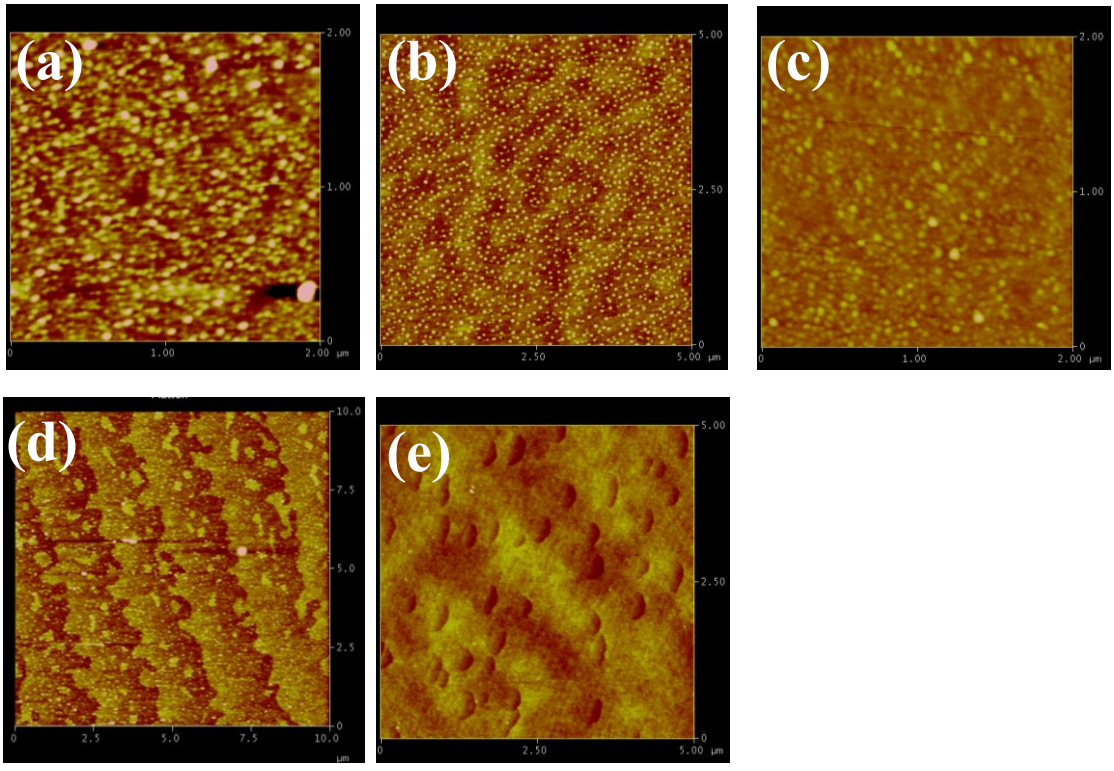


Figure II-2 AFM images of GGG(110) substrates under different treatments: (a) pristine substrate with mechanical polishing; (b) chemical etching; (c) annealing in oxygen at 600 °C; (d) annealing in oxygen at 1000 °C; (e) annealing in oxygen at 1300 °C.

The commercially available GGG substrates have been mechanically polished as our starting material. The chemical etching is generally applied to have properly terminated

layer of the surface in perovskite substrates. However, in the case of GGG, the etching by phosphoric acid does not improve the surface, as shown in Figure II-2(b), and this step is skipped in our recipe. The high temperature annealing in oxygen can greatly reduce oxygen vacancies and improve the crystalline condition on surface. A range of annealing temperature from 600 °C to 1300 °C was applied and the results are summarized in Figure II-2(c)~(e). The low temperature as 600 °C has little effect on the surface morphology and high temperature as 1300 °C creates bubbles and cracks that destruct the surface. Thus the optimal annealing temperature was determined to be 1000 °C, with atomically flat terraces on the surface due to small mis-cut. The roughness within the terraces was better than 1 Å by AFM images, which was smaller than a mono-layer.

2.3.2 Post-annealing Effects

The as-grown YIG film is usually amorphous if the growth parameters are not fully optimized, which could result in off-stoichiometry or non-crystalline material, as shown in Figure II-3(a). The color of as-grown amorphous YIG film was dark brown and there was no RHEED reflection pattern from the lattice. By subsequent *ex situ* annealing in atmosphere oxygen at high temperature from 600 °C to 1100 °C, the color became light yellow as the bulk material and the RHEED pattern reformed, as shown in Figure II-3(b), indicating the YIG film was epitaxially crystallized but the lattice of YIG film might not be locked to the substrate lattice.

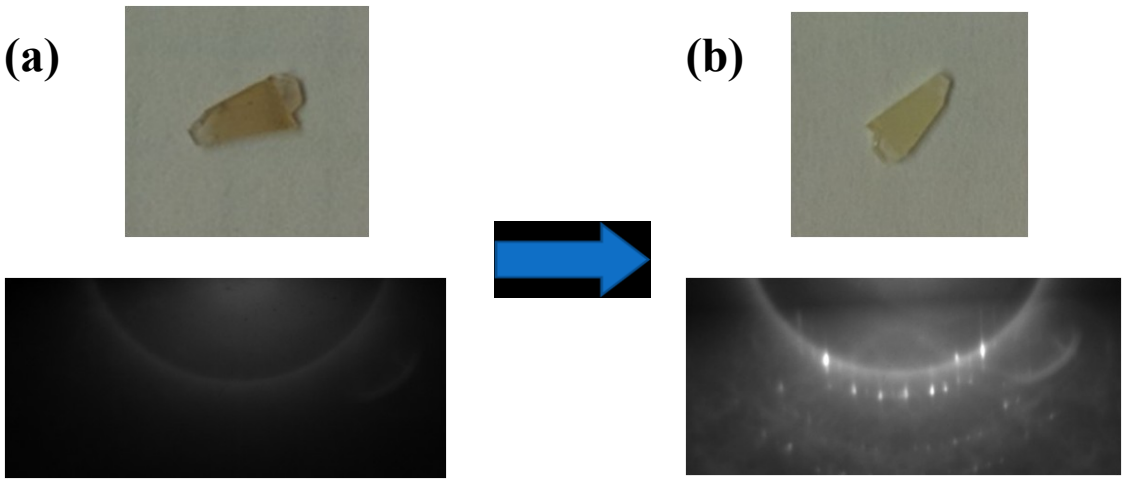


Figure II-3 (a) The color of as-grown YIG film (before parameters optimization) is dark brown (top), and the RHEED pattern disappears (bottom), suggesting amorphous YIG deposition. (b) After annealing in oxygen at 800°C for 6 hours, the color of YIG film become light yellow (top), and the RHEED pattern reforms (bottom), suggesting crystallization of the film.

Although the amorphous YIG film could be crystallized by post-annealing at a wide range of temperatures, the annealing temperature has a great impact on the magnetization of the film, as shown in Figure II-4. The heating and cooling rate were kept at 4 °C per minute and the holding time was 6 hours, with an atmosphere of ambient oxygen gas. The as-grown sample had a very weak magnetic moment, and it is clear that post-annealing greatly improved the magnetization of the film, especially between 600 °C and 900 °C. However, the annealing temperature higher than 1000 °C led to a chemical reaction of substrate and thin film materials, and caused the decreasing of magnetic moment. Thus the optimal post-annealing temperature was determined to be 800 °C.

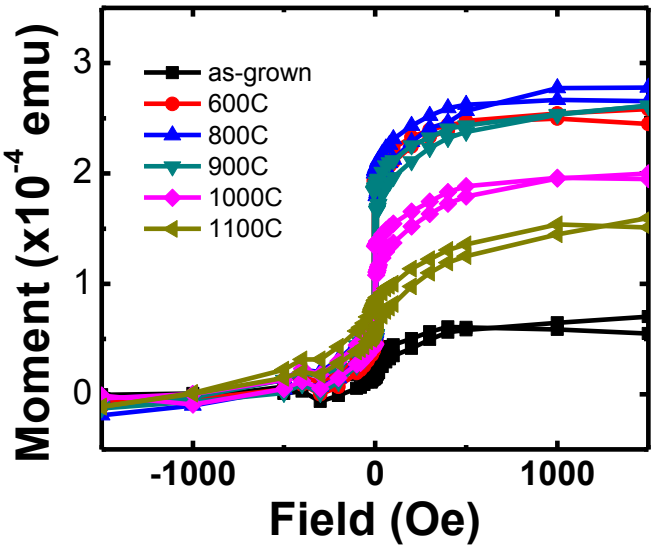


Figure II-4 The magnetic hysteresis loops of YIG film (before parameters optimization) with different annealing temperatures in oxygen for 6 hours. The optimal annealing temperature was determined to be 800°C. The curves are offset for clear comparison.

On the other hand, with the optimal growth parameters described in §2.2, high quality as-grown YIG films were obtained, as shown in Figure II-5. The color of as-grown film was the same as the post-annealed sample, suggesting epitaxial crystalline growth. The crystal structure was further verified by RHEED patterns and intensity oscillations, which will be discussed in details later. Furthermore, the magnetic moment of the as-grown sample was strong and did not improve with post-annealing procedure, indicating the growth parameters have been optimized for film magnetization.

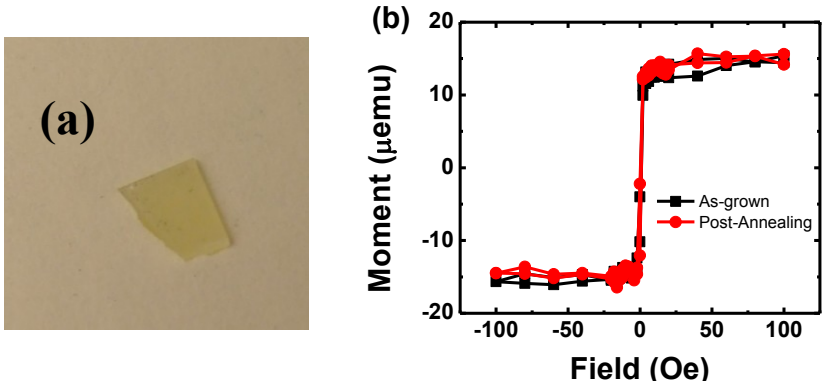


Figure II-5 With optimal growth parameters, high quality as-grown YIG films were obtained. (a) The color of as-grown film is light yellow, suggesting crystalline growth. (b) The magnetic hysteresis loop shows magnetic moment of as-grown film is the same as post-annealed at 800 °C.

2.3.3 Molecular Beam Epitaxy and Layer-by-layer Growth

The laser molecular beam epitaxy (laser MBE) is desirable to deposit high quality thin film, and layer-by-layer mode (Frank-van der Merwe growth) is preferred in thin film interface engineering and superlattice fabrication. By carefully tuning the growth parameters, the laser MBE growth was achieved as indicated by RHEED pattern in Figure II-6. It is clear that the crystal structure was consistent before and after the deposition, suggesting epitaxial growth of YIG film on GGG(110) substrate.

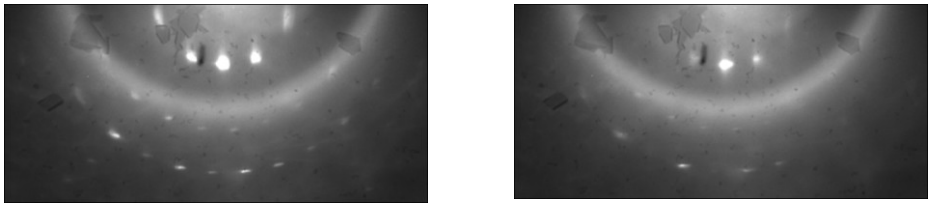


Figure II-6 With optimal growth parameters, RHEED patterns before (left) and after (right) deposition of YIG on GGG(110) are consistent, suggesting epitaxial growth of YIG on GGG(110).

Furthermore, the layer-by-layer growth mode was obtained, as shown in Figure II-7. The atomic layers were indicated by RHEED intensity oscillations, with maximum (minimum) intensity due to full (half) coverage of crystalline film. Note that each oscillation corresponds to one mono-layer, which is 1/4 of the unit cell length.

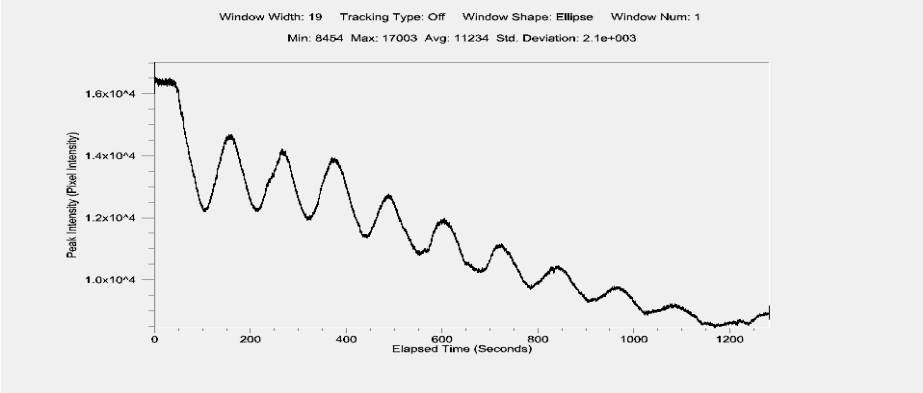


Figure II-7 With optimal growth parameters, RHEED intensity oscillations suggest layer-by-layer growth mode during YIG/GGG(110) deposition. Each period of the oscillation corresponds to one mono-layer (1/4 unit cell) of YIG, with full coverage at peaks and half coverage at valleys.

The proper parameters were determined in the growth on (111)-orientation GGG substrate as well, as shown in Figure II-8.

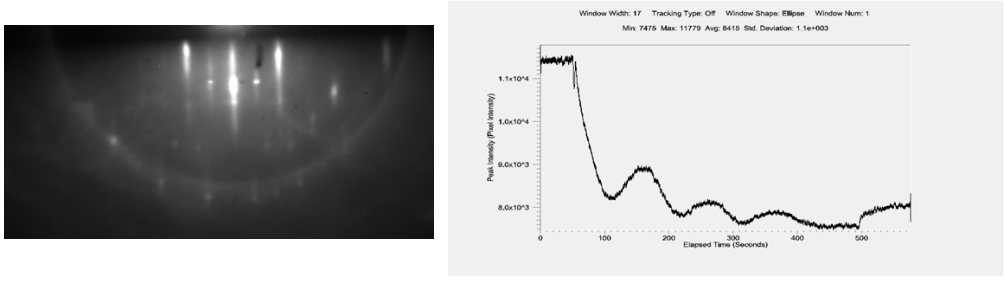


Figure II-8 With optimal growth parameters, (a) RHEED pattern and (b) RHEED intensity oscillations demonstrate high quality layer-by-layer epitaxy deposition of YIG/GGG(111) thin films.

2.3.4 Atomically Flat Terraces

With the capability of epitaxial layer-by-layer growth and the atomically flat GGG substrate, the atomically flat terraces were observed on the surface of grown films, as shown in Figure II-9. Note that in (110)-orientation, each mono-layer corresponds to 1/4 of unit cell face diagonal length, thus the height of each mono-layer is 4.375 Å ($12.376\ Å/4 \times \sqrt{2}$). The step height at the edge of the terrace was measured as 4.38 Å by AFM, which agreed well with the calculated atomic layer spacing. The roughness within the terraces was 0.6 Å, which is much smaller than the step height.

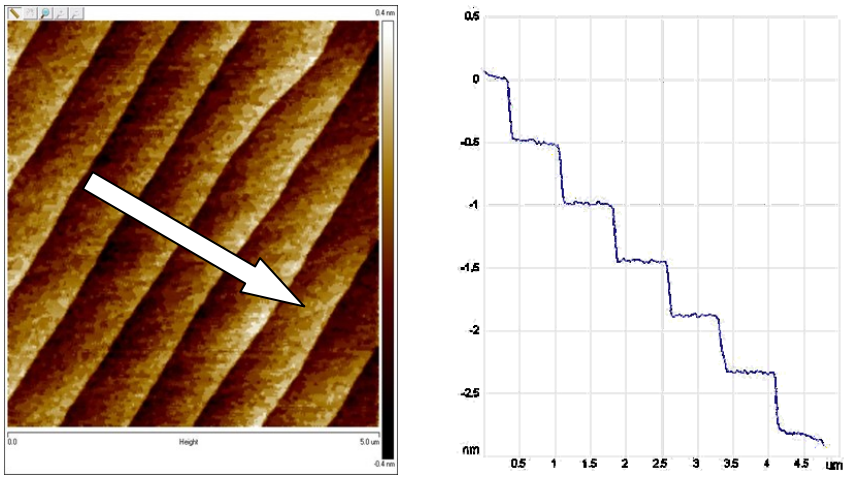


Figure II-9 Clear atomically flat terraces of YIG/GGG(110) were shown by AFM topography image (left) and cross-section of the steps (right). The height of each step (monolayer) is 4.38 Å, which agrees with YIG lattice constant (12.376 Å/4*√2 = 4.375 Å)

The atomically flat terraces were also observed on (111)-orientation YIG/GGG samples, as shown in Figure II-10.

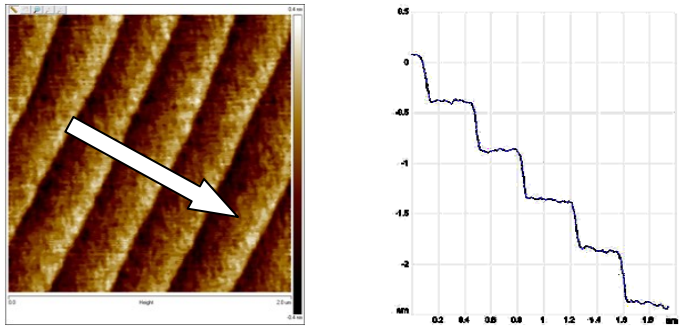


Figure II-10 AFM images of atomically flat terraces on YIG/GGG(111).

2.4Magnetic Properties

The magnetic properties of YIG/GGG films were measured and shown in Figure II-11, with both in-plane and out-of-plane magnetic fields applied. The magnetization had clear in-plane easy axis and the out of-plane saturation field was about 2000 Oe.

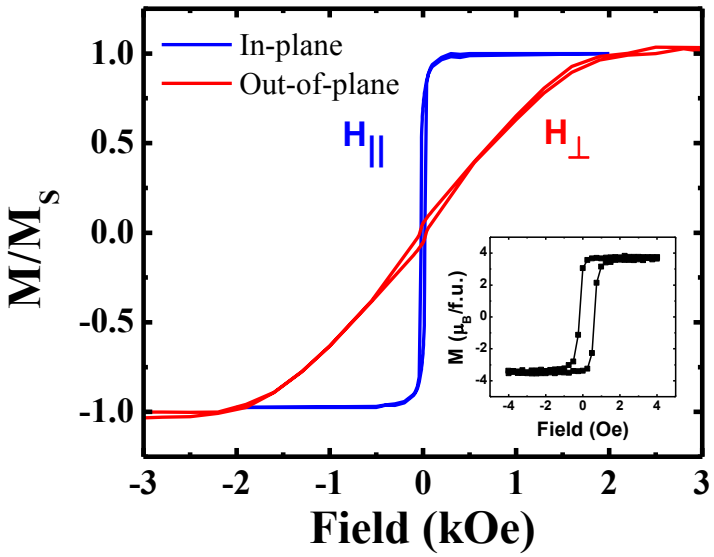


Figure II-11 In-plane and out-of-plane magnetic hysteresis loops of YIG/GGG(110) thin film at 300K. The magnetization has in-plane easy axis. Inset: Zoom in of in-plane magnetic moment.

Although the magnetically easiest axis in bulk YIG samples is <111>, in YIG thin films the shape anisotropy dominates and the easy axis is always in-plane. The in-plane coercive field of YIG/GGG(110) could be as low as less than 1 Oe and the shape of hysteresis loop was square. In YIG/GGG(111) samples, similar magnetic hysteresis loops as YIG/GGG(110) were observed.

The temperature dependence of the magnetization was explored and shown in Figure II-12. The saturated magnetic moment per formula unit (f.u.) was about 5 μ_B/f.u. at low temperature (25 K) and decreased by about 30% at room temperature, which is consistent with the reported value [47]. More interestingly, the coercive field was almost independent of the temperature in our measurement limits.

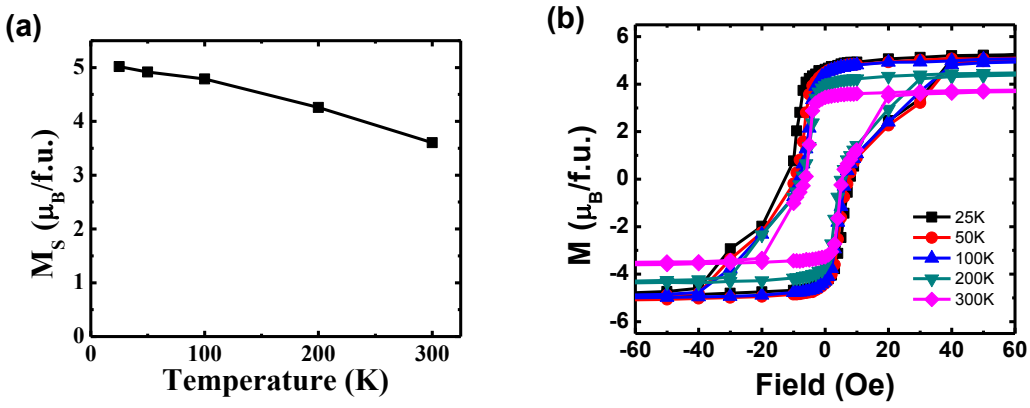


Figure II-12 (a) The saturated magnetic moment of YIG film decreased by about 30% at room temperature from low temperature (25 K). (b) The coercive field of YIG film was almost independent of temperature.

Furthermore, the in-plane magnetic anisotropy of YIG/GGG samples was investigated, as shown in Figure II-13. The external magnetic field was applied in the sample plane with rotating direction relative to the direction perpendicular to terraces, which is indicated by the arrow in Figure II-9, and the coercive field and remanence were measured from the hysteresis loops corresponding to each direction. The shape of hysteresis loops suggested that the easiest axis in plane was at 90° and the relative hardest axis was at 0° or 180°. Quantitatively, the coercive field was minimized or maximized at 90° or 0° respectively, changing by a factor of ~6, while the remanence was maximized or minimized at respective direction by a factor of more than an order.

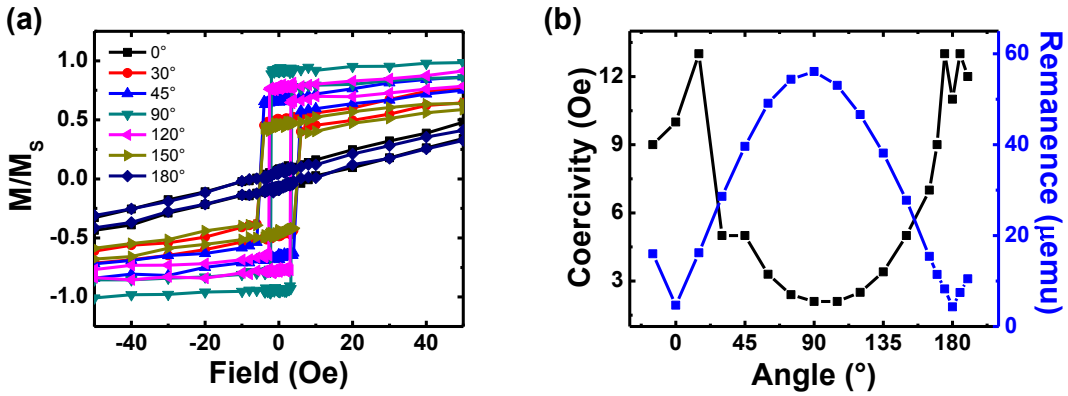


Figure II-13 In-plane angular dependence of magnetic remanence and coercive field of YIG/GGG(110) shows in-plane magnetic anisotropy.

2.5Discussion

The fabrication of high quality epitaxial YIG thin film is only feasible on ultra smooth crystalline substrates, with well prepared target materials. Besides those preparations, the

growth parameters have great impacts during the deposition. The substrate temperature is critical to obtaining the layer-by-layer growth mode, since lower temperatures generally cause polycrystalline or amorphous film and rougher surface, while higher temperatures lead to the step flow growth and a slow deposition rate. The ambient oxygen pressure is important in film stoichiometry. On the other hand, higher density of particulates are often induced with higher oxygen pressure, thus the chemical active ozone is helpful in reducing particulates while avoiding oxygen vacancies. The laser power is also taken into consideration to maintain stoichiometric material with a reasonable growth rate. High laser repetition rate (40 Hz) was reported necessary in epitaxial layer-by-layer YIG thin film growth and obtaining as-grown magnetization [47,60]. However, we demonstrated the layer-by-layer growth is feasible by using repetition rates as low as 5 Hz with other optimal parameters, while keeping high quality of magnetization and surface morphology.

In summary, the growth parameters of YIG thin films have been investigated, and high quality YIG thin films have been successfully epitaxially layer-by-layer grown on both (110)- and (111)-oriented GGG substrates with optimal growth conditions. The as-grown YIG films have bulk-like magnetization with in-plane anisotropy, and atomically flat terraces were obtained on the surface. The high quality YIG films and surface

engineering enable the further study of spintronics devices based on magnetic insulators.

The growth parameters of YIG/GGG are summarized in Table II-1.

Substrate treatment	Anneal in oxygen at 1000 °C for 6 hours
Base pressure	Better than $1x10^{-7}$ Torr
Background gas	2.2 mTorr oxygen with 12 wt% of ozone
Substrate temperature	650~750 °C
Laser energy	160 mJ per pulse
Laser repetition rate	5~10 Hz
Surface coating	N/A

Table II-1 Growth Parameters of YIG films by PLD

Chapter III

Induced Magneto-transport Effects at Interface

3.1 Introduction

3.1.1 Anomalous Hall Effect

The ordinary Hall effect (OHE) and anomalous Hall effect (AHE) were discovered by Edwin Hall more than a century ago. In general, both effects are the production of a voltage difference across the sample, with an electric current transverse to it and a magnetic field perpendicular to the current. The OHE is well understood as a result of Lorenz force deflecting the charge carriers in magnetic field $\boldsymbol{F} = q(\boldsymbol{E} + \boldsymbol{v} \times \boldsymbol{H})$, and the Hall voltage V_H is given by $V_H = -IH/net$ and the Hall coefficient is defined as $R_H = E_y/j_x H = -1/ne$. In semiconductors where the carriers are both electrons and holes, the expression becomes

$$R_O = \frac{p\mu_h^2 - n\mu_e^2}{e(p\mu_h + n\mu_e)^2} \tag{3.1}$$

The OHE has provided an elegant tool to measure carrier concentration of non-magnetic conductors in semiconductor physics and solid-state electronics since late 1940s.

On the other hand, the stronger AHE in ferromagnetic materials has been an enigmatic problem that attracts both theoretical and experimental interests for decades [61]. The empirical relation between ρ_{xy}, H_z and M_z is established by Pugh *et al.* [62],

$$\rho_{xy} = R_O H_z + R_{AH} M_z \tag{3.2}$$

The first term in above equation describe the OHE contribution, where R_O is the ordinary Hall resistivity. The second term represents AHE contribution due to spontaneous magnetization of the sample, where AHE resistivity R_{AH} is material dependent. Note that the second term is only due to material magnetization not total magnetic field, it is a convenient tool to study the magnetic properties of the material.

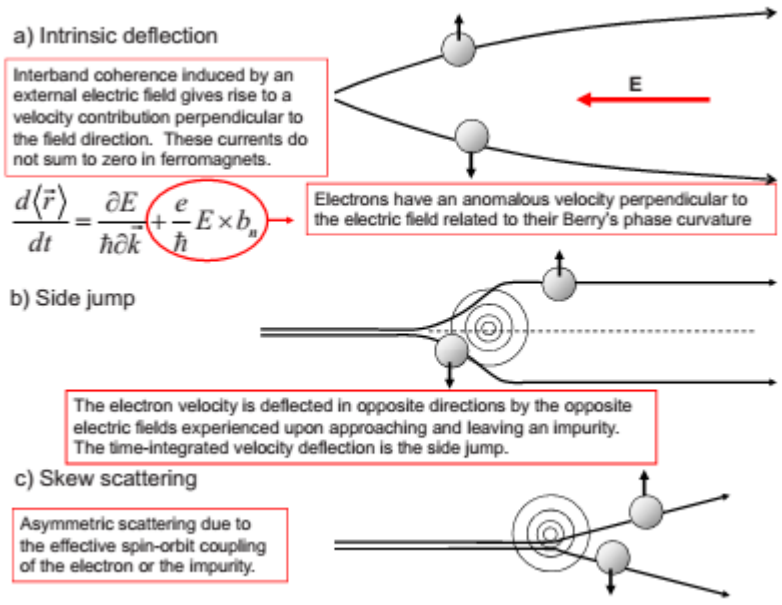


Figure III-1 Illustration of the three main mechanisms that can give rise to AHE. [Nagaosa *et al.*, 2010]

Many efforts have been made to understand the mechanism of AHE, and the three main mechanisms are illustrated as Figure III-1. The scaling of AHE resistivity in terms of the longitudinal resistivity ρ_{xx} of corresponding mechanism are: (1) intrinsic deflection [63], where $\rho_{int} \propto \rho_{xx}^2$; (2) extrinsic skew scattering at impurities [64], where $\rho_{sk} \propto \rho_{xx}$; (3) extrinsic side jump at impurities [65], where $\rho_{sj} \propto \rho_{xx}^2$. Despite the controversies [29,66], it is generally accepted that the total AHE resistivity consists of all the three terms.

$$\rho_{AH} = \rho_{int} + \rho_{sk} + \rho_{sj} \tag{3.3}$$

A typical AHE result of Fe_3O_4/MgO(100) film is shown in Figure III-2.

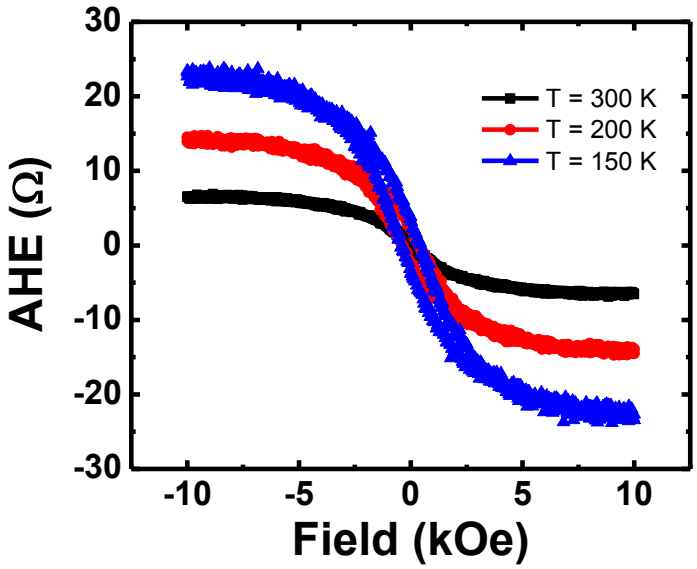


Figure III-2 Typical AHE measurements of Fe_3O_4(53nm)/MgO(100).

3.1.2 Seebeck Effect and Anomalous Nernst Effect

The thermoelectric effects reveal charge carrier transport phenomena induced by temperature differences. Discovered by Thomas Johann Seebeck in 1821, the Seebeck effect is the electric field $\boldsymbol{E}$ produced when the applied temperature gradient ∇T causes the charge carriers to diffuse from the hot side to cold side. The thermopower, or Seebeck coefficient, is expressed as $E = S\nabla T$. Note that there are charge carriers moving in the conductor, which is different from the spin Seebeck effect to be discussed later (see §3.1.4). The Nernst effect, discovered by Walther Nernst and Albert von Ettingshausen, describes the phenomenon of the transverse electric field produced, when a longitudinal temperature gradient and a perpendicular magnetic field are both applied to the conductor. In semi-classical picture [67,68], the effects can be expressed by the conservation of the charge current density $\boldsymbol{J_e}$ and the heat current density $\boldsymbol{J_Q}$ in present of a temperature gradient ∇T:

$$\begin{aligned} \mathbf{J}_{\mathrm{e}} &= \bar{\sigma}\cdot\mathbf{E} + \bar{\alpha}\cdot(-\nabla T) \\ \mathbf{J}_{Q} &= T\bar{\alpha}\cdot\mathbf{E} + \bar{\kappa}\cdot(-\nabla T) \end{aligned} \tag{3.4}$$

Here $\bar{\sigma}$, $\bar{\alpha}$, $\bar{\kappa}$ are electrical, thermoelectric and thermal conductivity tensors, respectively. The well known Mott relation, $S = \frac{\pi^2 k_B^2 T}{3e\sigma}(\frac{\partial\sigma}{\partial E})_{E_F}$, links the transport coefficients [69,70].

In the system steady state (i.e. $\boldsymbol{J_e} = \mathbf{0}$), the above equations gives $\boldsymbol{E} = \bar{\sigma}^{-1} \cdot \bar{\alpha} \cdot \nabla T$. And the Nernst coefficient is given:

$$N = \frac{E_y}{\nabla_x T} = \frac{\alpha_{xy}\sigma_{xx} - \alpha_{xx}\sigma_{xy}}{\sigma_{xx}^2 + \sigma_{xy}^2} \tag{3.5}$$

Similar to AHE, the anomalous Nernst effect (ANE), which is the Nernst signal corresponding to material magnetization, also provides an efficient tool to study the magnetism under temperature gradient [69–72].

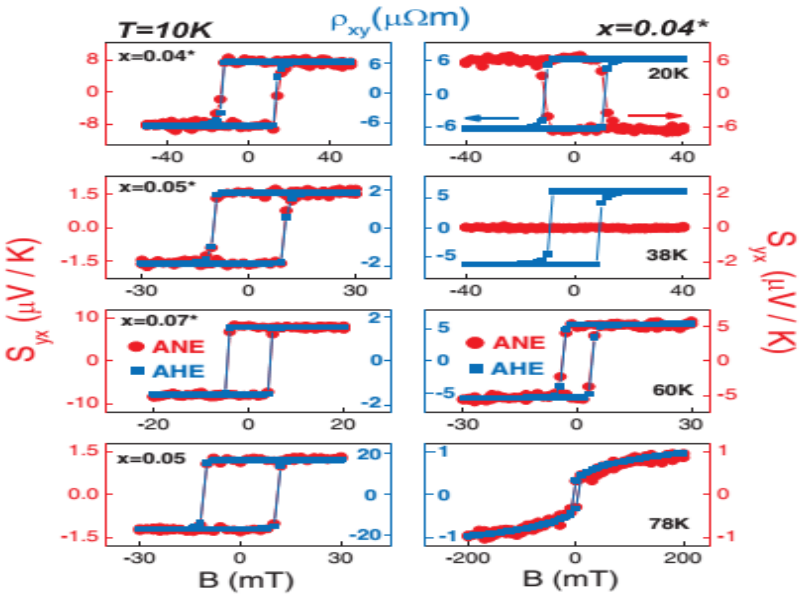


Figure III-3 Typical ANE measurements of $Ga_{1-x}Mn_xAs$ (x=0.04-0.07). [Pu *et al.*, 2008]

3.1.3 Spin Hall Effect and Inversed Spin Hall Effect

The spin Hall effect (SHE) was predicted by Dyakonov and Perel [73,74] and then introduced by Hirsch [75], and has recently attracted close attention both

theoretically [76–78] and experimentally [79–87]. When an electric current is applied in the sample, there appears spin accumulation on the lateral surface due to skew scattering of the magnetic moments for an extrinsic mechanism, and the signs of spin directions of the charge carriers are opposite at opposite boundaries, which forms spin current, as shown in Figure III-4. Note that the electric current direction, spin current direction and spin polarization direction are orthogonal.

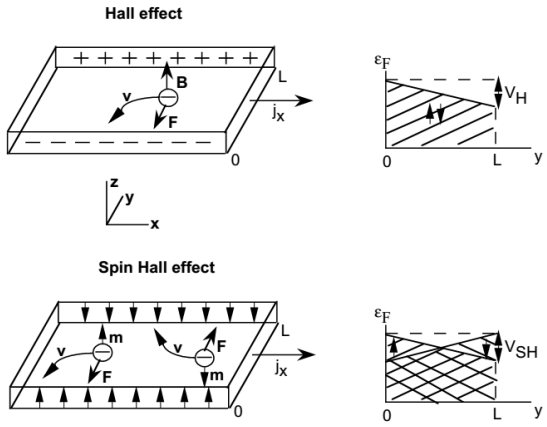


Figure III-4 Illustration of Hall effect (top) and spin Hall effect (bottom) in conductive sample with electron-like charge carriers. [Hirsch, 1999]

SHE is somewhat similar to the Hall effect, where the accumulation of the opposite *charges* is due to Lorenz force in magnetic field, and the hall voltage V_H is caused by the different Fermi level at the two edges, while the Fermi level of spin up and spin down electrons is the same. However, the accumulation of *spin* in SHE is due to skew scattering of the moving magnetic moments. It is not necessary to have external magnetic field and the signal is defined by the difference in the Fermi level for each *spin* limited by

spin relaxation at the boundaries. The reciprocal effect, that an electric current is induced by spin current in strong SOC material, with orthogonal directions, is called inversed spin Hall effect (ISHE).

Experimentally, SHE was first observed by Kato *et al.* in an n-type semiconductor [79] and Wunderlich *et al.* in a p-type semiconductor [80], and ISHE was first observed optically by Bakun *et al.* [81]. Saitoh *et al.* demonstrated ISHE in Py/Pt metal system by spin pumping and ferromagnetic resonance [82], Valenzuela *et al.* demonstrated direct electronic detection of SHE [83] and Kimura *et al.* demonstrated reversible SHE/ISHE [84] later. The empirical relation among the electric current $\boldsymbol{J_c}$, spin current $\boldsymbol{J_s}$ and spin-polarization vector σ is given by:

$$\mathbf{Jc} = D_{ISHE}\mathbf{Js}\times\sigma \tag{3.6}$$

Here D_{ISHE} is a coefficient representing the SHE/ISHE efficiency in a material.

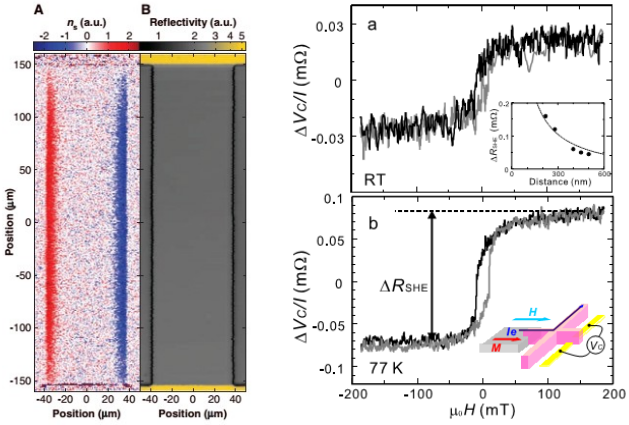


Figure III-5 Experimental demonstrations of SHE (left) [Kato *et al.*, 2004] and ISHE (right) [Kimura *et al.*, 2007].

3.1.4 Spin Seebeck Effect

Recently, the thermal spintronics or spincaloritronics [88] is of great interest, as spintronic devices reveal both heat and spin transport. Among many interesting phenomena, the spin Seebeck effect (SSE), which generates a spin voltage over a long distance through a temperature gradient in ferromagnetic materials, has received much attention [43,44,89–102]. These discoveries suggest possible ways to control spin current by means of heat current or *vice versa*.

In 2008, Uchida *et al.* first demonstrated SSE in a ferromagnetic metal film ($Ni_{81}Fe_{19}$) detected by ISHE of attached non-magnetic Pt layer [89]. This phenomenon invigorated the community, because the length scale of several millimeters in the experiments is much larger than the spin-flip diffusion length of conduction electrons, which suggests it is related to spin current besides conduction electrons. Similar effects are uncovered in more material systems subsequently. In 2010, Jaworski *et al.* studied the SSE in a semiconducting ferromagnet (Ga,Mn)As and showed that SSE does not originate from the charge flow in their experiments [90]. And Uchida *et al.* showed that SSE exists not only in conducting materials but also in ferrimagnetic insulators $LaY_2Fe_5O_{12}$ [43], where the charge carrier is irrelevant. These findings opened up a frontier in this field and more experiments are carried out with ferromagnetic metal Co_2MnSi [91], sintered

ferromagnetic insulator $(Mn,Zn)Fe_2O_4$ [92], and even ferromagnetic oxide magnetite (Fe_3O_4) at temperature below Verwey transition [93].

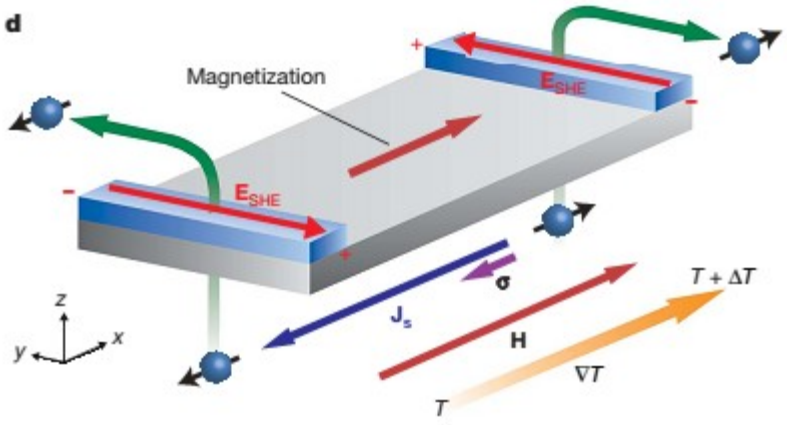


Figure III-6 Illustration of the SSE induced by temperature gradient ∇T in the plane of the NiFe film, and the ISHE induced by Pt wires attached to the end of the film. J_s and E_{SHE} denote the spin current and ISHE voltage respectively. And the spin polarization direction σ lies along the direction of magnetic field H, which is in the film plane. [Uchida *et al.*, 2008]

The schematic illustration of SSE from Uchida et al. [89] can be seen in Figure III-6. When a temperature gradient ∇T is applied, the localized spins in the ferromagnetic material are excited by the heat current and generate a finite spin voltage in the material. The spin current is then injected into the normal metal, where ISHE is induced. Two contributions from the heat current that excites localized spins have been recognized [94]: the magnon heat current and the phonon heat current, corresponding to the two relevant processes termed magnon-driven spin Seebeck effect [95,96] and phonon-drag spin Seebeck effect [97].

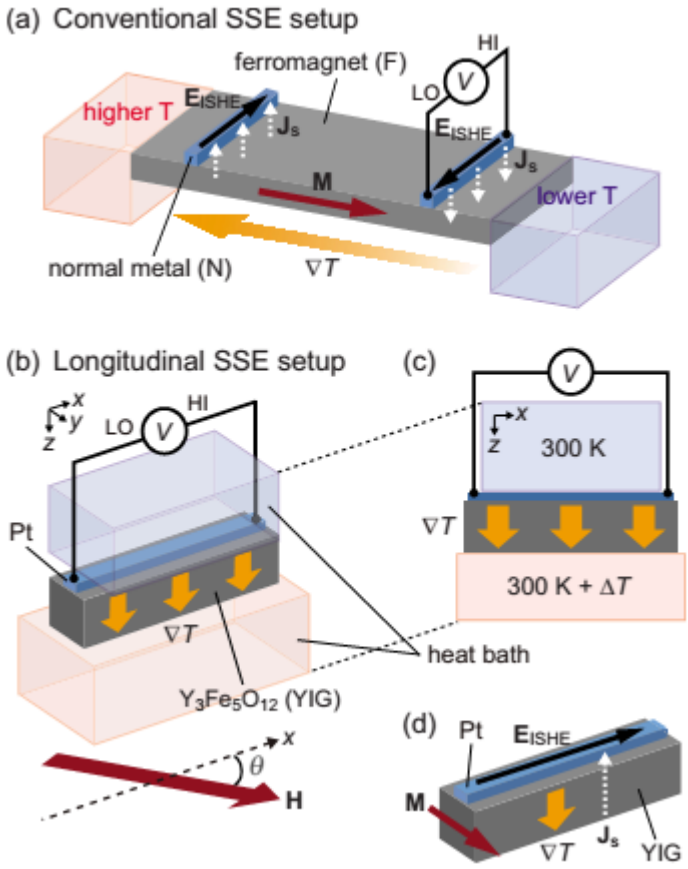


Figure III-7 Illustration of conventional (transverse) SSE setup (top) and longitudinal SSE setup (bottom). Here, ∇T, *M*, *Js*, and E_{ISHE} denote the temperature gradient, the magnetization of ferromagnet (F), the spatial direction of spin current across the F/normal metal (N) interface, and the electric field generated by ISHE in N, respectively. [Uchida *et al.*, 2010]

Several experimental techniques have been adopted since the discovery of SSE. The conventional setup, or so-called transverse SSE, was used in the first studies of SSE [43,89,90]. In this setup, the temperature gradient is applied in the plane of the ferromagnetic material, and the spin injection into the normal metal (spin current) is transverse to the temperature gradient, as shown in Figure III-7(a). The other setup is the longitudinal SSE setup [98], which has the temperature gradient perpendicular to the

material plane, so the spin current is in the longitudinal direction of the temperature gradient, as shown in Figure III-7(b). The longitudinal SSE setup has simple and versatile geometry, but it cannot be realized if the magnetic materials used are electrically conductive, as the geometry is identical to ANE and the phenomenon will be contaminated by ANE signal, as well as the ISHE signal will be shorted by the conductor. Recently, Uchida *et al.* developed another way to study SSE by acoustic spin pumping [99], which open the door to exploiting sound waves for constructing spin-based devices. And Kirihara *et al.* suggest an application of spin-current-driven thermoelectric coating in energy harvesting technologies by utilizing longitudinal SSE device [100].

3.1.5 Magnetic Proximity Effect vs. Spin Seebeck Effect

The spin polarization of a magnetic metal (e.g. Fe, Ni, or Co) could penetrates into a nonmagnetic metal or alloy with high exchange-enhanced spin susceptibility (e.g. Pd or Pt), known as magnetic proximity effect (MPE) [103], and it has been experimentally demonstrated by x-ray magnetic circular dichroism (XMCD) [104–107] or MFM [108]. Recently, SSE in magnetic insulators was challenged by a possible MPE [109] existing at the Pt/magnetic-insulator interface. It was shown that the MPE, along with the anomalous Nernst effect in the magnetized Pt interface layer can generate a significant SSE-like signal. Because the longitudinal SSE and ANE share the same device geometry, as shown

in Figure III-8(a), it is doubted the pure spin phenomenon measured by Pt could be contaminated.

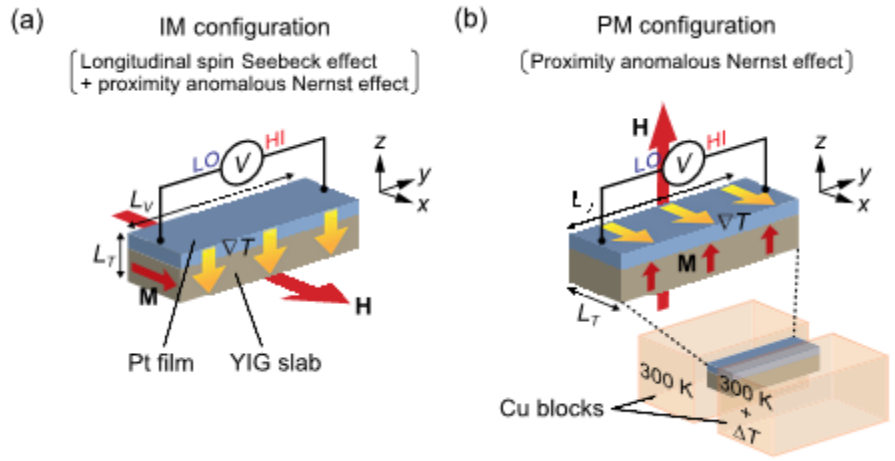


Figure III-8 Schematic illustration of the Pt-film/YIG-slab sample in (a) the in-plane magnetized (IM) configuration and (b) the perpendicular-magnetized configuration. In IM configuration, both the longitudinal SSE and proximity ANE are possible to contribute to the signal. In PM configuration, only proximity ANE is possible. [Kikkawa *et al.*, 2013]

More experiments have been carried out in different geometries to separate MPE from SSE, as shown in Figure III-8 [110]. It is shown that in perpendicular magnetized (PM) configuration, the signal is negligible relative to the SSE signal in in-plane magnetized (IM) configuration, and it is argued SSE dominates in the phenomenon. Furthermore, Au is known as a strong SOC metal and less prone to magnetic proximity effect. In an Au/YIG bilayer, SSE was still found to be present, which was believed to be strong evidence of intrinsic SSE without magnetic proximity contribution [110], and Au is suggested as detector of SHE/ISHE [44].

At the heart of the debate, one key question is whether MPE exists in spin current detector materials where the inverse spin Hall effect is used. Direct quantitative measurements of Pt magnetization by XMCD were performed by independent teams [111,112], but with conflicting conclusions. Thus more evidence with different material is necessary to understand the phenomenon.

3.2Device Fabrication and Measurements

Motivated by the recent experiments, we studied the magneto-transport properties of the normal metal/magnetic insulator bilayer structure. YIG is chosen as our magnetic insulator material, because of its large band gap (~2.85 eV) and high Curie temperature (~550 K) that has advantage in measurements, as discussed in previous chapter (see Chapter II). And Pd is chosen as the normal metal material for our study, while Pt/YIG device is discussed as well. First of all, Pd and Pt are transition metals and have large magnetic susceptibility which favors MPE. It is shown that MPE exists at Pd/ferromagnetic metal interfaces [113] and Pt/magnetic insulator interfaces [109,112]. Secondly, Pd and Pt have strong SOC and large spin Hall conductivity [114]. To address the issue of possible MPE in magnetic insulator based structures, Pd/YIG devices are fabricated and studied, as well as Pt/YIG devices.

Thin YIG films are grown on single crystal GGG substrates with both (110) and (111) orientations by Laser MBE, as described previously (see Chapter II). The thickness of YIG thin film is typically 100-200 nm in this study. After the deposition of YIG films, they are taken out of the PLD chamber and immediately placed into a high-vacuum sputtering chamber (AJA International ORION 5) for Pt or Pt deposition. In typical devices, YIG films are lightly sputter cleaned for 5~10 minutes before metal deposition, to remove any possible contamination and provide fresh and clean surface. The typical deposition parameters are summarized as in Table III-1. Metal (Pd or Pt) thin films with thickness range from 1.5 nm to 10 nm are used in the study. All Pd films are covered by 5 nm of MgO passive layer to protect from oxidation, and Pt films are sustainable from oxidation thus no protective layer is required.

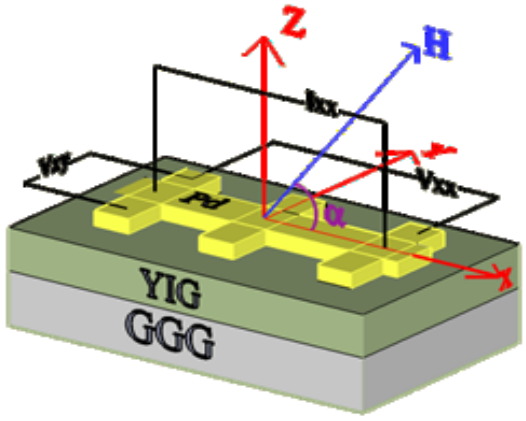


Figure III-9 Schematic diagram of the patterned Hall bar for induced magneto-transport experiments.

	Plasma strike	Deposition	Growth rate
Substrate cleaning	Ar: 30 mTorr RF: 10 W, 30 sec	Ar: 5 mTorr RF: 25 W	
Pd	Ar: 30 mTorr DC: 150 W, 5 sec	Ar: 2.1 mTorr DC: 18 W	0.385 Å/sec
Pt	Ar: 30 mTorr DC: 150 W, 5 sec	Ar: 5 mTorr DC: 37 W	0.768 Å/sec
Cu	Ar: 30 mTorr DC: 150 W, 5 sec	Ar: 5 mTorr DC: 37 W	0.667 Å/sec
Fe	Ar: 30 mTorr RF: 60 W, 10 sec	Ar: 5 mTorr RF: 60 W	0.0856 Å/sec
Ta	Ar: 30 mTorr DC: 150 W, 5 sec	Ar: 5 mTorr DC: 37 W	0.334 Å/sec
NiFe	Ar: 30 mTorr DC: 150 W, 5 sec	Ar: 5 mTorr DC: 48 W	0.37 Å/sec
IrMn	Ar: 30 mTorr DC: 150 W, 5 sec	Ar: 5 mTorr DC: 75 W	0.667 Å/sec
Al	Ar: 30 mTorr DC: 150 W, 5 sec	Ar: 5 mTorr DC: 37 W	0.167 Å/sec
MgO	Ar: 30 mTorr RF: 60 W, 10 sec	Ar: 4.4 mTorr RF: 300 W	0.121 Å/sec

Table III-1 Sputter deposition parameters.

After the deposition, Hall bars with the width of 200 μm and length of 1000 μm are patterned by photo-lithography (Karl Suss MA-6) and Ar ion milling through inductively coupled plasma (Oxford Plasmalab Multiplex ICP), as shown in Figure III-9. Thick photo-resist and optimal ion milling parameters are chosen to avoid ion implantation into the film. The detail procedures are described as follows and shown in Figure III-10.

(1) Sample cleaning: acetone with ultrasound (15 min); IPA with ultrasound (15 min); DI water (5min); then bake 5 min at 110 C on hot plate.

(2) Spin-coating with AZ® 5214 or 9245 photo-resist, 3 sec at 500 rpm, then 40sec at 4000 rpm. Bake for 3 min @ 90 C on hot plate.

(3) Exposure for 15~20 sec. Develop with MF-319 for 60 sec. Hard-bake for 3 min at 115 C on hot plate.

(4) ICP Etch: 10 mTorr Ar gas, 40 W RF power, 250 W ICP power. The etching rate is about 2 Å/min for MgO layer.

(5) Remove photo-resist and residues.

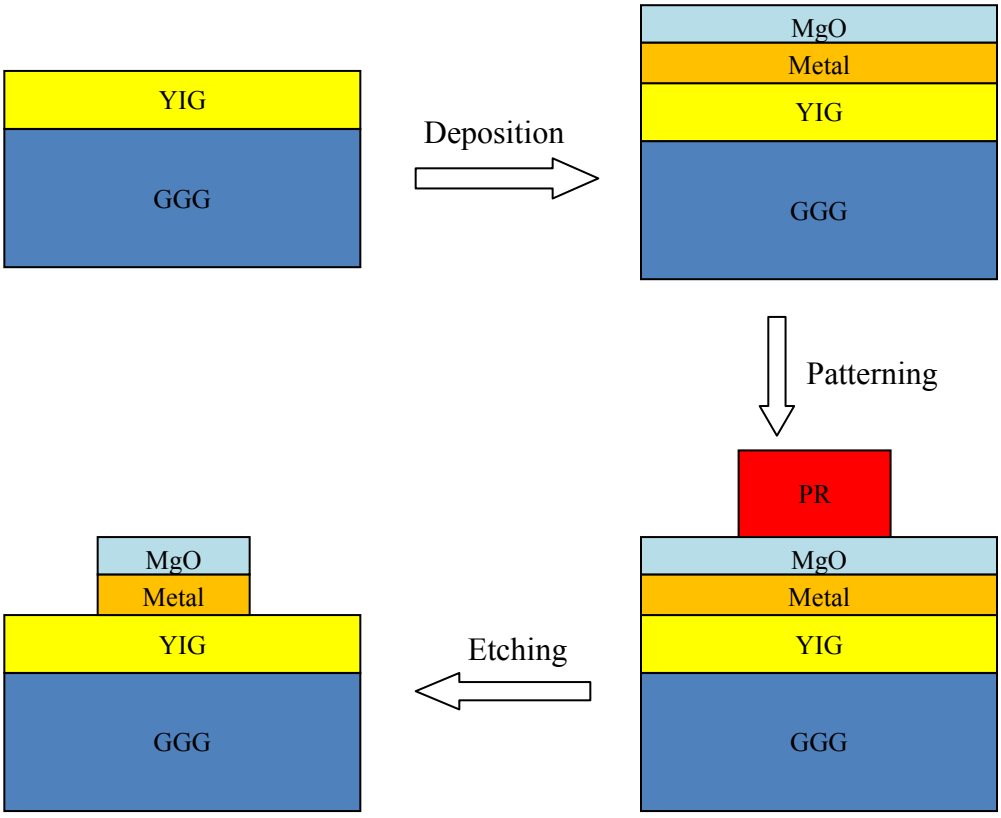


Figure III-10 Schematic diagram of Hall bar device fabrication by etching method.

The magnetic properties of YIG films are measured with either a vibrating sample magnetometer (VSM) or Quantum Design's magnetic property measurement system. The magneto-transport are conducted in either a close-cycled refrigerator with an electromagnet (<1 T) or Quantum Design's physical property measurement system (up to 14 T). In Hall bar devices, standard 4-probe method is used to measure both resistance and Hall voltage, and the van der Pauw method is utilized in unpatented films.

3.3 Low-Field Magneto-transport Effects

We first studied the low-field magneto-transport effects of Pd/YIG. As an in-plane magnetic field $H_{\parallel}$ is swept along the Hall bar direction, the magnetoresistance (MR), $\frac{\Delta\rho}{\rho} = \frac{\rho(H)-\rho(0)}{\rho(0)}$, of a Pd (2 nm)/YIG is shown in Figure III-11, along with the magnetization data of YIG. Two negative peaks appear at the coercive fields of YIG, which suggests the feature is linked with the magnetization of YIG film. This feature resembles the anisotropic MR effect in ferromagnetic conductors. Here the MR peak is only ~$6\text{x}10^{-6}$, several orders smaller than that of the anisotropic MR in ferromagnetic conductors. MR with similar magnitude was previously reported in Pt/YIG where the YIG films are polycrystalline [109]. For comparison, a 2 nm thick Cu film deposited on YIG does not show any measurable MR signal, which means such effects happen in the material with strong SOC. One possible cause of MR in Pd film is that the non-magnetic Pd film acquires a magnetic moment whose direction is dictated by the underlying YIG

film, i.e. the Pd interface layer adjacent to YIG acting as if it is magnetic. Another possibility is the so-called spin Hall magnetoresistance (see Chapter IV). Similar effects are observed in Pt/YIG bi-layer structure, as shown in Figure III-12.

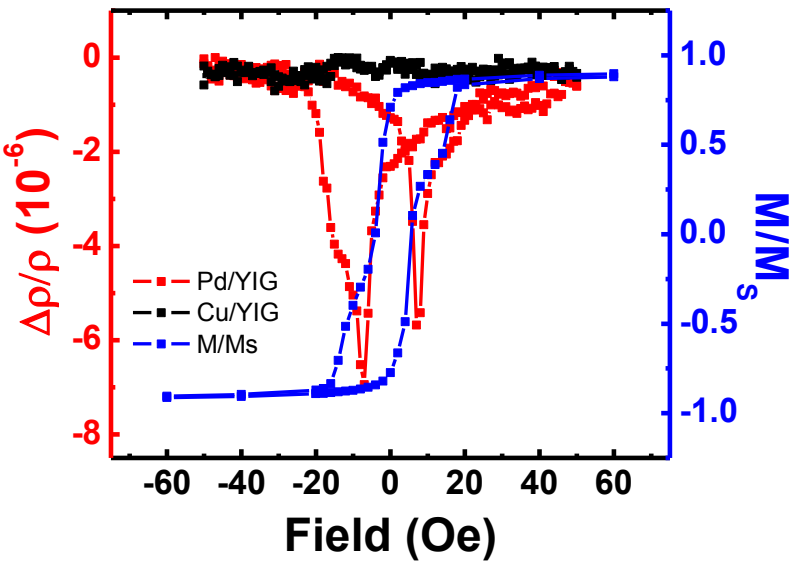


Figure III-11 In-plane low-field MR of Pd(2 nm)/YIG (red squares), MR of Cu/YIG reference sample (black squares), and in-plane hysteresis loop (blue squares). The positions of MR peaks are the same as the coercivity of YIG film.

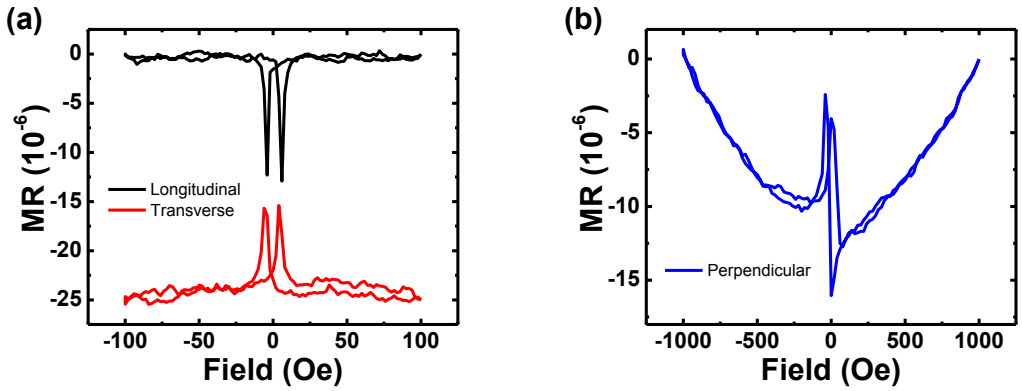


Figure III-12 Low-field MR of Pt(2nm)/YIG with (a) in-plane and (b) perpendicular magnetic field. The transverse MR is offset for clearance.

As shown in Figure III-13, the MR peaks are correlated with the coercive fields of YIG which do not change significantly with the temperature in this temperature range. However, the MR peak nearly doubles when the temperature is lowered to 30 K, which is consistent with reduced spin-flip scattering.

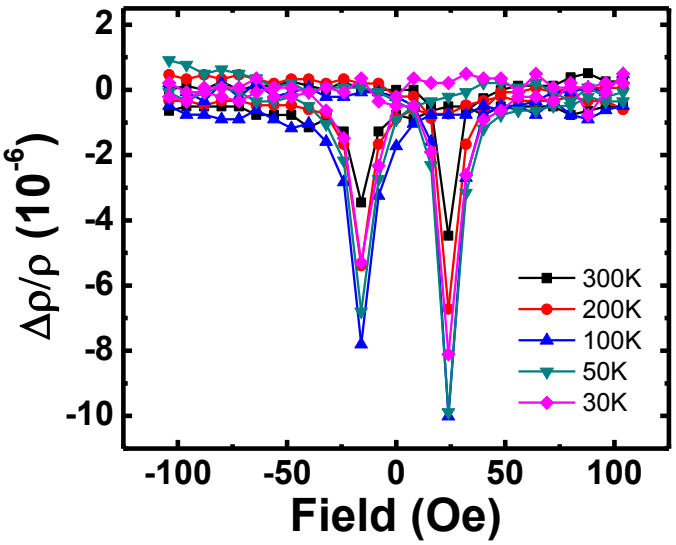


Figure III-13 Temperature dependence of MR ratio of Pd(2 nm)/YIG.

The Pd thickness dependence of the low-field MR is also studied to understand the interfacial contribution, as shown in Figure III-14. Three different thicknesses (2 nm, 5 nm, and 10 nm) of Pd are deposit on the same YIG sample and the in-plane MR and OHE are measured at room temperature. If the MR originates from the bulk magnetization of Pd, the MR ratio will be independent of the thickness. On the other hand, if it is an interfacial effect, assuming the change of interfacial magnetoresistance is independent of the Pd thickness and according to the formula of MR ratio, it is shown that

$$MR = \frac{\Delta R_{interface}}{R_{total}} \sim \frac{1}{R_{total}} \sim \frac{1}{n_{2D}} \tag{3.7}$$

The 2D carrier density is determined by Hall resistance $R_{yx} = -B/n_{2D}e$. It is clear from Figure III-14(c) that the low-field MR is linear in 2D carrier density and thus it is an interfacial effect.

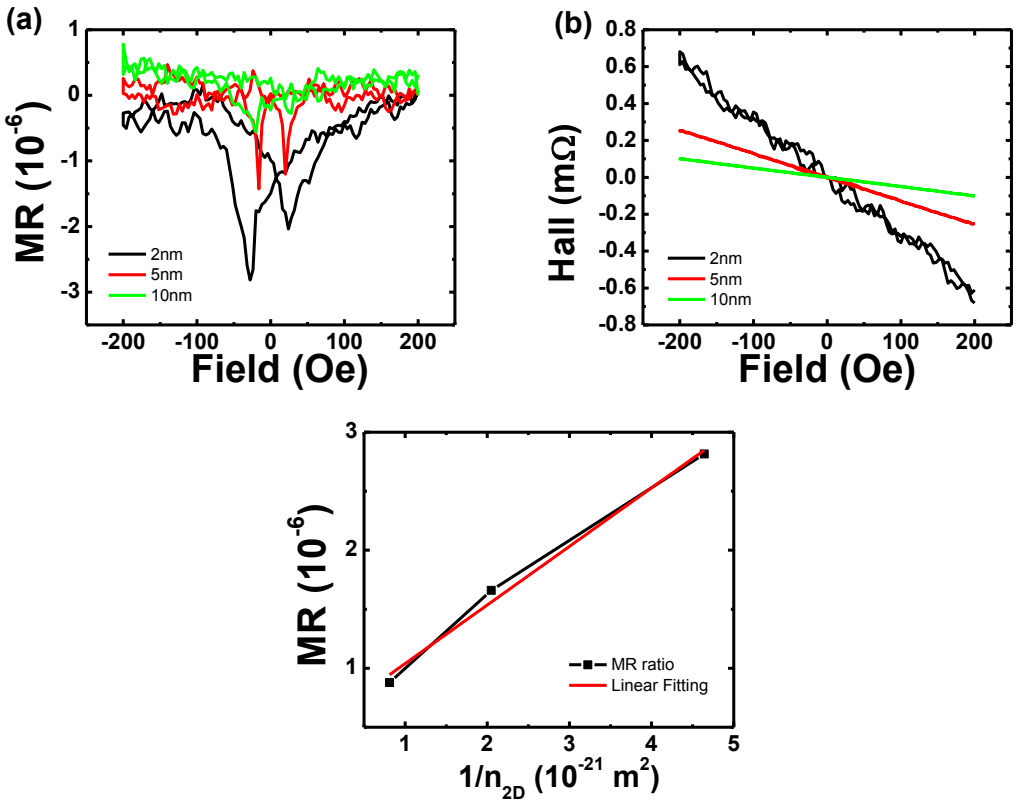


Figure III-14 Thickness dependence of (a) MR and (b) Hall resistance of Pd(x nm)/YIG. (c) MR ratio as function of inverse 2D density shows interfacial effect.

3.4High-Field Magneto-transport Effects

3.4.1 High Field Magneto-resistance

We have extended MR measurements to high fields. Figure III-15 shows MR of the same Pd/YIG sample with the magnetic field along the longitudinal direction in plane ($H_{\parallel}$) or perpendicular to the film $H_{\perp}$, and they are almost identical to each other.

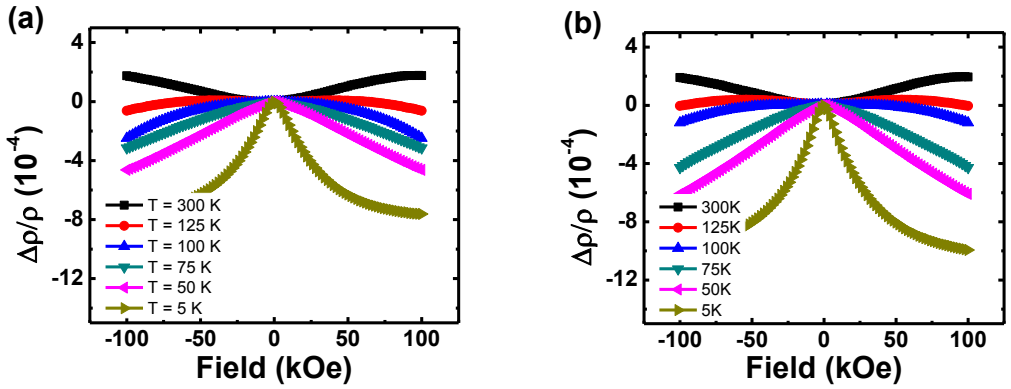


Figure III-15 (a) In-plane and (b) out-of-plane high-field MR of Pd(2nm)/YIG at different temperatures. The MR of two magnetic field directions are similar.

Surprisingly, there is a much larger high-field magnetoresistance (HFMR) background that completely dwarfs the low-field MR signal shown in Figure III-11. At high temperatures, the positive MR is probably the usual Lorentz force induced effect. As the temperature is lowered, this positive MR diminishes and turns to negative. Negative MR is usually seen in materials with random spins that can be aligned by an external field to cause suppressed scattering. At the lowest temperature, the HFMR ratio reaches ~ -10^{-3}, nearly two orders greater than that of MR at low fields. The comparison between the low-

and high-field MR reveals that in addition to the low-field phenomenon related to the YIG magnetization reversal, there is some spin-dependent process occurring at high fields. When additional spins are aligned with high fields, the MR ratio is consequently enhanced. It is interesting that the temperature dependence of HFMR (Figure III-16) is markedly different from that of the low-field MR.

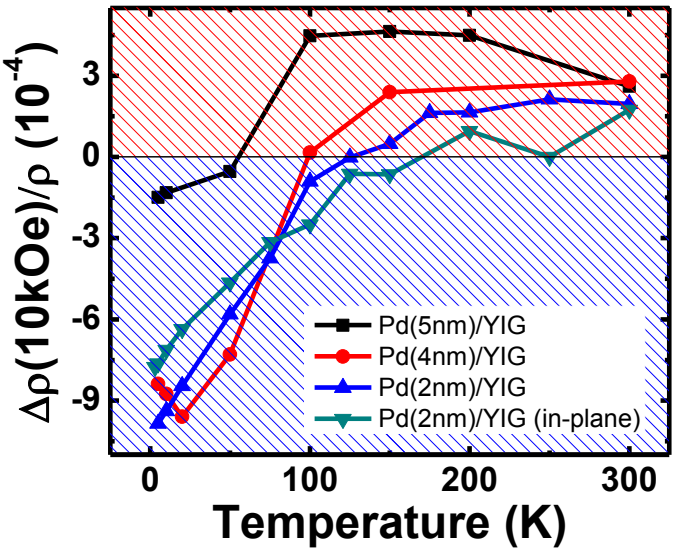


Figure III-16 (a) MR ratio at H=10 kOe as a function of temperature. Red and blue regions represent positive and negative MR ratios respectively. The devices with different thickness of Pd layer show similar behavior.

In Pt/YIG devices (Figure III-17), the HFMR behavior is in general the same as Pd/YIG, except the magnitude of HFMR is larger, which is possibly due to stronger SOC of Pt, and the temperature dependence of HFMR shows more clear competing mechanism at intermediate temperatures.

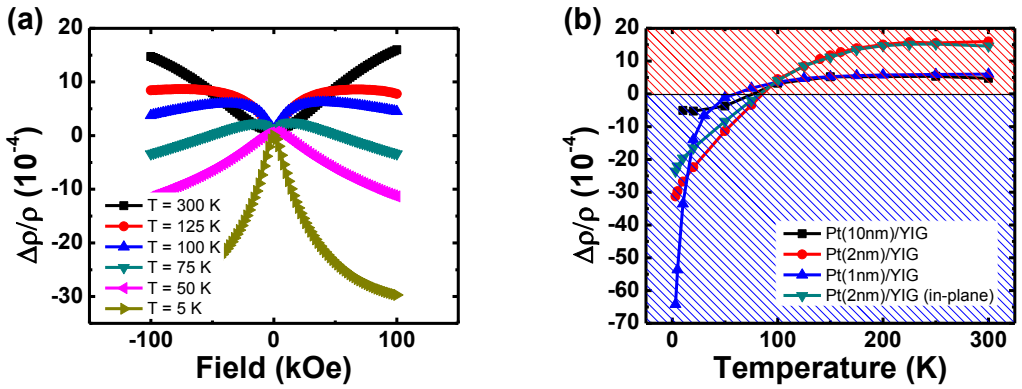


Figure III-17 (a) Out-of-plane high-field MR of Pt(2nm)/YIG at different temperatures. (b) Temperature dependence of MR ratio at H=10 kOe for different thickness of Pt layer.

3.4.2 AHE-like Effect

In ferromagnetic conductors, superimposed on the ordinary Hall effect that is linear in $H_{\perp}$, there is an anomalous Hall effect (AHE) that is proportional to the out-of-plane magnetization component. However, in the low field range (up to ~2 kOe) where the in-plane magnetization is rotated towards the perpendicular direction, we do not observe any definitive magnetization-related AHE signal. As we ramp up $H_{\perp}$ further, an unambiguous non-linear AHE-like signal arises on the linear ordinary Hall background, as shown in Figure III-18. The zero field longitudinal resistance and the carrier density calculated from the Hall resistance as a function of temperature is shown as well. It is noticeable that the resistance changes only about 18%, and the carrier density is almost unchanged at low temperature.

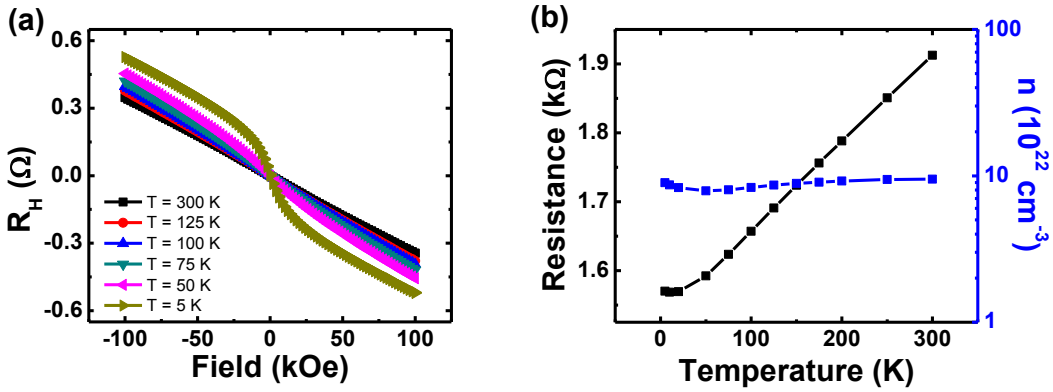


Figure III-18 (a) Hall Resistance of Pd(2nm)/YIG at different temperatures without linear background removal. (b) Temperature dependence of longitudinal resistance at zero field and carrier density calculated from ordinary Hall resistance.

After removing the linear background, the non-linear AHE-like resistances at different temperatures are shown in Figure III-19. At the lowest temperature, the saturation Hall resistivity reaches ~0.17Ω, equivalent to ~1x10^{-3} in the Hall angle. Note that the YIG magnetization saturates at $H_\perp \sim 2$ kOe. However, saturation of the AHE-like signal occurs at $H_\perp > 20$ kOe. Therefore, similar to the HFMR effect, the high-field Hall signal also reveals a response of the magnetic moments other than those in the Pd interface layer that are possibly exchange coupled to the YIG magnetization. We fit the Brillouin function, i.e. $B_J(x) = \frac{2J+1}{2J}\coth\left(\frac{2J+1}{2J}x\right) - \frac{1}{2J}\coth\left(\frac{1}{2J}x\right); x = \frac{g\mu_B JB}{k_B T}$, to the AHE-like data in Figure III-19 and the solid curves are the actual Brillouin fits. It is noted that the normalized AHE-like resistance does not scale as a function of B/T, as shown in the inset of Figure III-19, which means gJ changes at different temperatures.

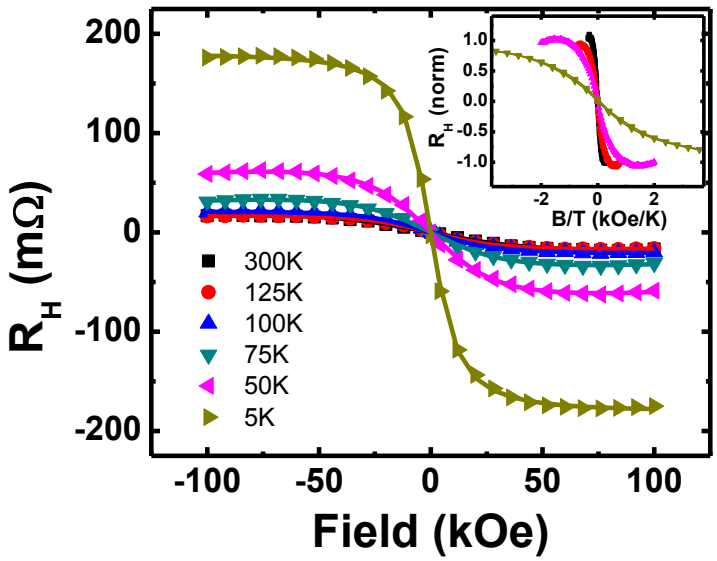


Figure III-19 Field dependence of the AHE-like Hall resistance R_H of Pd(2nm)/YIG at different temperatures with linear background removal. Lines are the Brillouin function fits. Inset: Normalized R_H as a function of B/T shows changing total angular momentum at different temperatures.

From the Brillouin function fitting in Figure III-19, we obtain parameter gJ at each temperature, here g being the Lande factor (fixed at 2 in the fitting), and J being the total angular momentum involved. The temperature dependence of saturation AHE-like resistance and gJ are displayed in Figure III-20. Interestingly, while the AHE-like resistance increases at low temperatures, the value of gJ decreases at low temperatures.

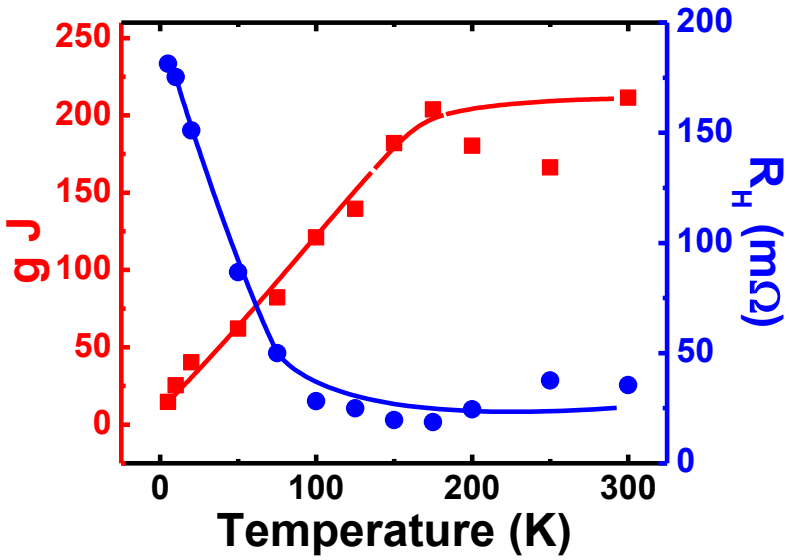


Figure III-20 Temperature dependence of *gJ* (red solid squares) and the saturation AHE-like signal (blue solid circles) obtained from the Brillouin fitting. Lines are guides to the eyes.

Figure III-21 shows the Pd thickness dependence of the AHE-like signal in Pd/YIG samples at low temperature (5 K). As the Pd thickness increases, the Hall magnitude sharply decreases. The inset shows the zoom-in plot of the AHE-like data for 4, 5, and 10 nm thick Pd. For 10 nm thick Pd, the Hall signal almost vanishes. The rapidly decreasing trend of the AHE-like signal clearly demonstrates the interfacial origin of the magnetic moments that are responsible for the high-field Hall effect, as the thicker Pd layers dilute the interface contribution. A summary of AHE-like resistance as a function of temperature for different Pd thickness is shown in Figure III-22. We note that the annealing of Pd(2 nm)/YIG destructs the AHE-like signal, which might relates to interface destruction.

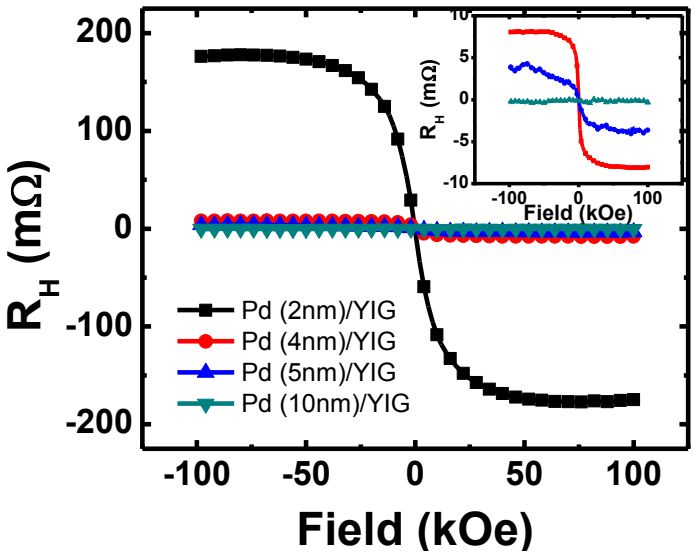


Figure III-21 Pd thickness dependence of the Hall resistance R_H at T=5 K. The inset shows the zoom-in data for Pd thicknesses from 4 to 10 nm.

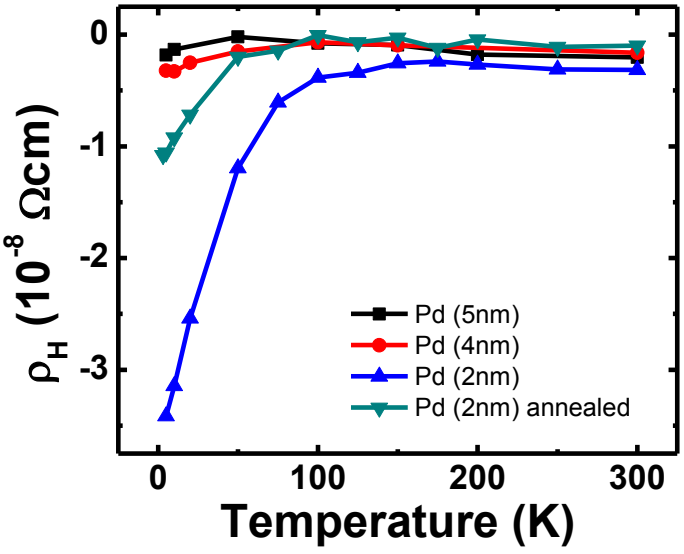


Figure III-22 AHE-like resistivity as a function of temperature for different thickness of Pd layer.

Figure III-23 further reveals the properties of the interface moments. First of all, Pd needs to be in direct contact with YIG. Pd on MgO does not produce any Hall signal; therefore,

the source of the interface moments must be YIG. Secondly, Cu either has no interface moments or does not produce any Hall signal even if it has interface moments. We cannot distinguish these two possibilities. If the latter is true, a 6 nm thick Cu layer is sufficiently thick so that Pd does not feel any effect from the magnetic moments at the Cu/YIG interface. It turns out that with 6 nm of Cu space layer, the AHE-like signal is negligible, if any.

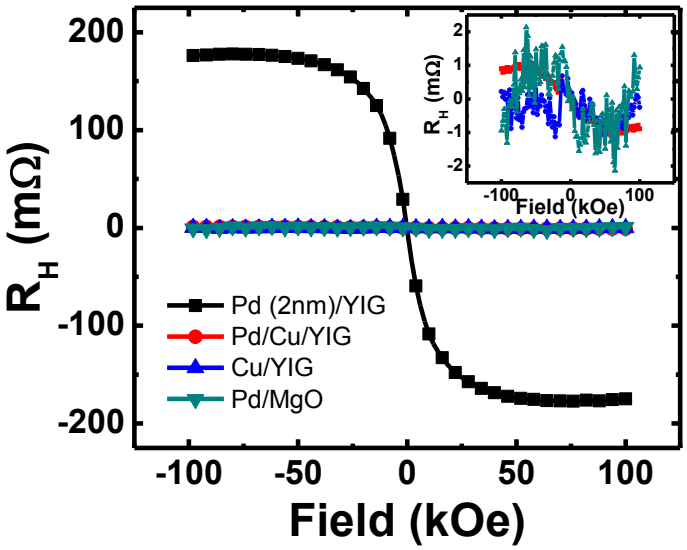


Figure III-23 AHE-like signal for several reference samples at T=5 K. All metal layers (except the Cu-layer in Pd/Cu/YIG) are 2 nm thick. The inset shows zoom-in data for reference samples.

In Pt/YIG devices, the high-field AHE-like phenomenon is qualitatively similar to that of Pd/YIG devices, as shown in Figure III-24. However, it is noted that R_H in Pt/YIG has a sign change at intermediate temperature, which suggests a competing mechanism depending on temperature and makes the quantitative analysis much more complicate.

The origin of the second mechanism is still unknown and requires more investigation. The temperature dependence of different Pt layer thickness implies optimal parameters for AHE-like experiments.

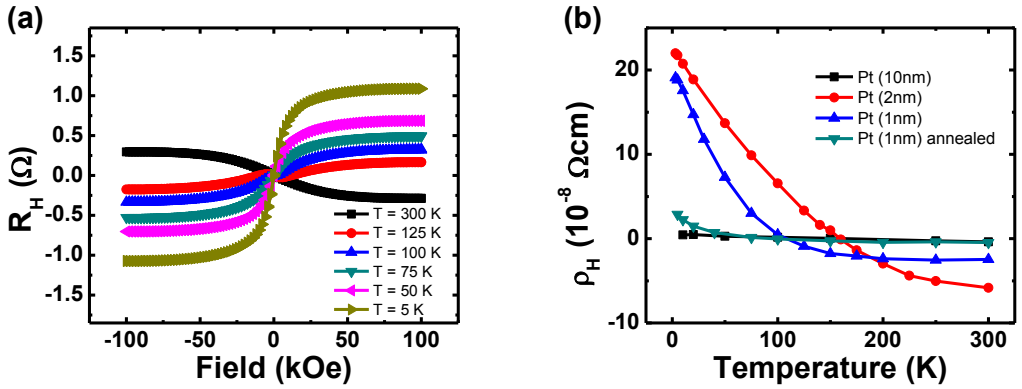


Figure III-24 (a) Field dependence of the Hall resistance R_H of Pt(2nm)/YIG at different temperatures with linear background removal. (b) AHE-like resistivity as a function of temperature for different thickness of Pt layer.

3.4.3 Possible Kondo Effect

In thin Pd films (<5 nm), we observe a resistivity minimum at a low temperature, below which the resistivity varies logarithmatically as shown in Figure III-25, indicative of the Kondo effect. The local moments at the Pd/YIG interface are likely the same source of the Kondo effect. We have also observed similar logarithmatic temperature dependence in Pt/YIG. In both systems, the AHE-like signal has steep temperature dependence at low temperatures. Similar enhanced low-temperature Hall signal was previously reported in other Kondo systems such as $CeCu_2Si_2$ [115]. Recently, it was theoretically shown that the skew scattering of Kondo impurities such as Fe can lead to a gigantic spin Hall angle

in Au films [116]. Nevertheless, more experimental investigations are needed in order to better understand the correlation between these two effects.

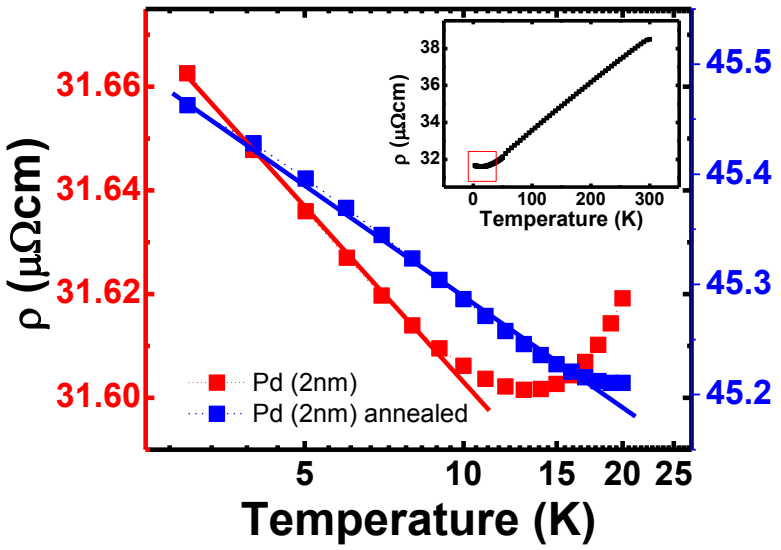


Figure III-25 Resistivity of Pd(2nm)/YIG at low temperatures as a function of log(T). The inset shows the full range temperature dependence. The Kondo-like effect is enhanced after annealing.

3.5Discussion

The high-field magneto-transport experiments strongly suggest that independent magnetic moments producing the high-field effects must originate from the normal metal/YIG interface moments that are not exchange coupled to the YIG spins; and those independent moments could be related to the regions of YIG protruding to normal metal. In ferromagnetic conductors, the carriers are spin polarized and AHE arises from either extrinsic or intrinsic mechanisms due to SOC. But the reverse is not necessarily true: the AHE-like signal does not prove ferromagnetism. In the framework of AHE, the

magnitude of AHE ρ_{xy}, scales with the resistivity, ρ_{xx}, either linearly or quadratically, i.e. $\rho_{xy} \sim \rho_{xx}^{n}$, with n=1 or 2, depending on the details of the mechanism (see §3.1.1). In our Pd/YIG, the longitudinal and Hall resistivity do not follow the power law, as shown in Figure III-26. In the meantime, we do not expect any sharp temperature dependence of the saturation magnetic moments. Therefore, the peculiar temperature dependence Figure III-20 argues against the AHE mechanism for spin-polarized carriers as in regular ferromagnets. Our experimental data in Pd/YIG are consistent with the skew scattering picture in which unpolarized electrons are deflected by local moments via SOC, similar to the noble metal-based dilute magnetic alloys [117].

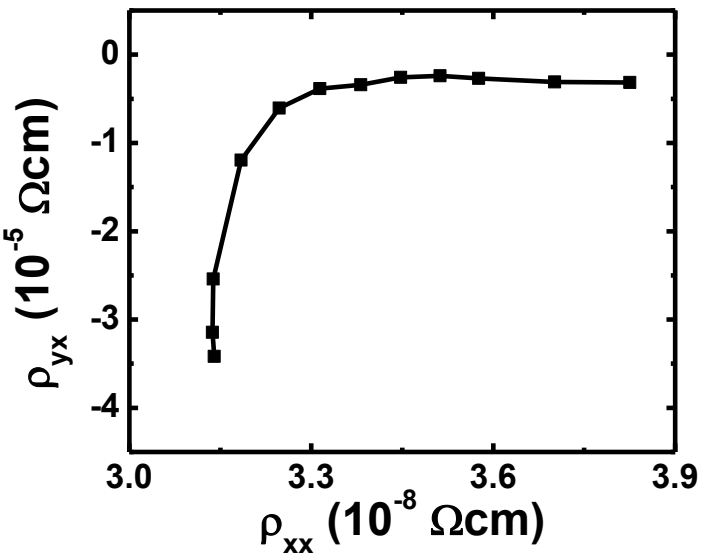


Figure III-26 Hall resistivity as a function of longitudinal resistivity.

We do not yet completely understand why gJ increases at higher temperatures. One possibility is that at low temperatures when the local moments are surrounded by

conduction electrons via an antiferromagnetic exchange, they act rather independently. At high temperatures where the Kondo screening becomes weaker, the ferromagnetic exchange between the d-electrons in Pd and the local moments increases. The polarized d-electrons in Pd therefore "dress" the local moments to result in an apparent increase in the size of the magnetic moments. It is well-known that a single Fe impurity can induce a local moment as large as 20 μ_B in Pd [118]. At Pd/YIG interface, it is possible that larger moments are induced by YIG molecules.

In summary, we have observed a low-field MR effect in Pd/YIG and Pt/YIG which track the bulk YIG magnetization reversal. In addition, we have also observed two different, much stronger magneto-transport effects that occur at high magnetic fields where the bulk YIG magnetization is already fully saturated. We attribute the observed Hall effect to the scattering of conduction electrons in Pd by local magnetic moments at Pd/YIG interface. At low temperatures, it is likely that the same local moments cause the Kondo effect observed in Pd/YIG samples which further enhance the Hall effect.

Chapter IV

Spin Hall Magnetoresistance

4.1 Introduction

4.1.1 Anisotropic Magneto-resistance (AMR)

When an external magnetic field is applied, a material can change its electrical resistivity, depending on either directly external field or its magnetization (controlled by the field). Such a property is called magnetoresistance (MR), first discovered by William Thomson in 1851. The former one is known as ordinary magnetoresistance (OMR), which arises from the circular motion of electrons in a magnetic field due to Lorenz force. The latter one includes several distinguished discoveries such as giant magnetoresistance (GMR) [119,120], colossal magnetoresistance (CMR) [121], magnetic tunnel effect (TMR) [122,123] and anisotropic magnetoresistance (AMR). We will discuss AMR in more details here.

The AMR effect describes the change of electrical resistivity due to the simultaneous action of magnetization and spin orbit interaction, depending on the orientation of the magnetization of the material. There have been great interests of AMR in diluted

magnetic semiconductors [124–126], low-dimensional semiconductors [127], magnetic metals [128–130] and oxides [131–134]. Another related effect is the planar Hall effect (PHE), which measures the transverse resistance when the magnetic field is applied in the plane. Both AMR and PHE share the same physical mechanism and have been used widely in the material magnetization study and magnetic sensors applications [134–137]. An example of AMR and PHE in epitaxial Ni film on MgO(001) substrate is shown in Figure IV-1.

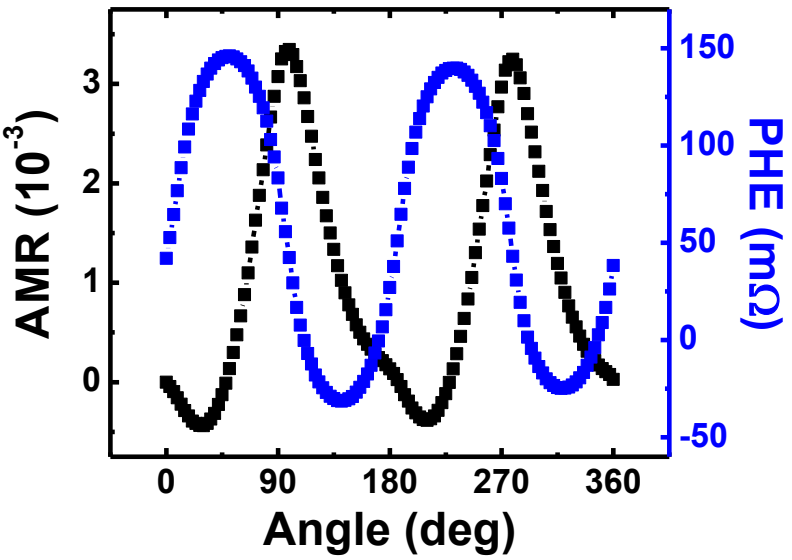


Figure IV-1 In-plane rotation AMR (black) and PHE of MgO(4nm)/Ni(10nm)/MgO(001) with current along <100> direction and magnetic field H=10 kOe.

If we consider the crystalline symmetry contribution and expand the magnetoresistance tensor, the AMR/PHE can be given by

$$\frac{\Delta\rho_{xx}}{\rho_{avg}} = A\cos(2\phi) + B\cos(4\varphi - 2\phi) + C\cos(2\varphi) + D\cos(4\varphi)$$
$$\frac{\Delta\rho_{xy}}{\rho_{avg}} = A\sin(2\phi) - B\sin(4\varphi - 2\phi) \quad (4.1)$$

Here $\Delta\rho_{xx} = \rho_{xx} - \rho_{avg}$, ρ_{avg} is the averaged longitudinal resistivity, ϕ is the angle between the magnetization $\boldsymbol{M}$ and the electric current $\boldsymbol{j}$, and φ is the angle between $\boldsymbol{M}$ and specific crystal axis. The first term is non-crystalline contribution and the second term is the crossed non-crystalline/crystalline contribution. The third and fourth terms are related to the crystal symmetry and only exist in single crystal sample. Thus in amorphous or polycrystalline samples, the above equations can be simplified as

$$\rho_{xx} = \rho_{\perp} + (\rho_{\parallel} - \rho_{\perp})\cos^2\phi = \rho_{\perp} + \Delta\rho_{AMR} m_x^2$$
$$\rho_{xy} = (\rho_{\parallel} - \rho_{\perp})\sin\phi\cos\phi = \Delta\rho_{AMR} m_x m_y \quad (4.2)$$

Here $\rho_{\parallel}$ and $\rho_{\perp}$ are the resistivities when the current direction is parallel and perpendicular to the magnetization, respectively. Note that both AMR and PHE have a period of 180° and are symmetric with respect to magnetization reversal. This symmetry is different from the AHE for magnetization normal to the film plane, which is anti-symmetric under magnetization reversal.

4.1.2 Spin Hall Magneto-resistance (SMR)

Recently, a new type of magnetoresistance was discovered by Nakayama *et al.* and Hahn *et al.* in normal metal (NM) and ferromagnetic insulator (FMI) hybrid structures [45,138],

termed as spin Hall magnetoresistance (SMR). The theoretical model was given by Chen *et al.* with more details [139], in terms of a non-equilibrium proximity effect at the NM/FMI interface caused by the simultaneous action of SHE and ISHE. It was pointed out that SMR, as an alternative mechanism, can result the magnetoresistance features observed previously [109,140], as discussed in §3.3, without involving the conventional AMR effects caused by the static magnetic proximity polarization in NM. Additional results were published for SMR in other magnetic insulator materials as nickel ferrite and magnetite [141], and the dependence on NM thickness and direction of magnetization was explored as well [142]. These developments may find new applications for insulator spintronics.

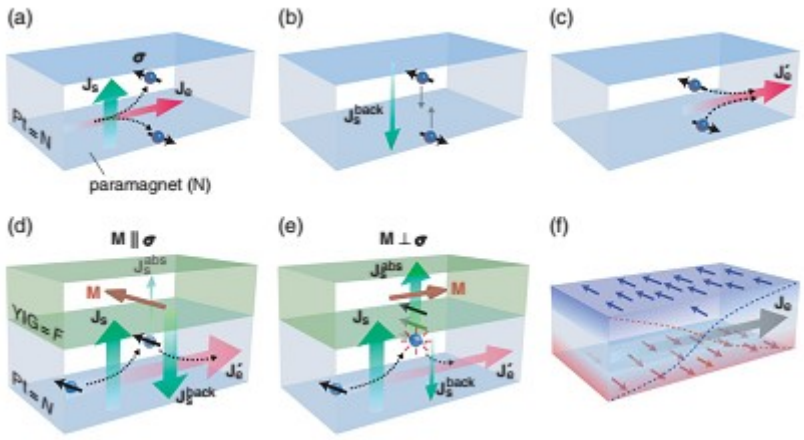


Figure IV-2 Illustration of the mechanism of SMR. (a), (b) and (c) Illustration the magnetic control of the electrical conductivity of non-magnetic metal (N) by SHE/ISHE with strong spin-orbit interaction. (d) and (e) Illustration the geometric relation between the magnetization *M* in the magnetic insulator (F) and the spin current J_s, and the additional charge current J_e due to ISHE (f) Illustration the spin accumulation due to SHE in N. [Nakayama *et al.*, 2013]

The physical origin of SMR can be explained based on simultaneous SHE/ISHE actions, and the spin-dependent scattering at NM/FMI interface. The illustration of the mechanism of SMR is shown in Figure IV-2. First, due to SHE, a charge current in NM flowing along the x-direction generates a y-polarized spin current, j_s, flowing along the z-direction. When the magnetization $\boldsymbol{M}$ in the FMI is collinear (perpendicular) to the spin polarization of j_s, the magnitude of reflected spin current j_s^{back} meets the maximum (minimum) through weak (strong) spin relaxation due to spin-transfer torque from NM into FMI. And subsequently, j_s^{back} yields a strong (weak) additional ISHE voltage superimposed on the longitudinal voltage signal in NM. It has been shown that SMR is well formulated with some approximations as

$$\begin{aligned} \rho_{long} &\approx \rho + \Delta\rho_0 + \Delta\rho_1(1-m_y^2) \\ \rho_{trans} &\approx \Delta\rho_1 m_x m_y \end{aligned} \tag{4.3}$$

where

$$\begin{aligned} \frac{\Delta\rho_0}{\rho} &= -\theta_{SH}^2 \frac{2\lambda}{d_N} \tanh\frac{d_N}{2\lambda} \\ \frac{\Delta\rho_1}{\rho} &= \theta_{SH}^2 \frac{\lambda}{d_N} \frac{2\lambda G_r \tanh\frac{d_N}{2\lambda}}{\sigma + 2\lambda G_r \coth\frac{d_N}{\lambda}} \end{aligned} \tag{4.4}$$

Here m_x and m_y are the x-component and y-component of the magnetization unit vector respectively, and is $\rho = \sigma^{-1}$ is the intrinsic electric resistivity of the bulk normal metal, and $\frac{\Delta\rho_1}{\rho}$ is related to the spin diffusion length λ, metal film thickness d, electrical conductivity of the metal film σ, spin Hall angle θ_{SH}, and the real-part of the

spin-mixing conductance G_r. Note that the formulas in (4.3) have the same form as AMR in (4.2) except for one difference: the longitudinal resistivity of SMR depends on m_y but AMR depends on m_x. However, they are not experimentally distinguishable by a sweeping or rotation in-plane external field.

In the common features of magnetoresistance effect observed in bilayer systems [44,45,109,139,140], it might be interpreted as favorable evidence for the mechanism each side advocates. Namely, it on one hand bears close resemblance with the conventional AMR effect, which implies the existence of the proximity induced magnetization at the interface. On the other hand, similar observation was attributed to SMR that is due to the magnetization-dependent spin current reflection at the SOC metal/YIG interface. If the magnetoresistance effect is indeed truly SMR instead of AMR, one could exclude the MPE in the bilayers, which further validates the earlier conclusion drawn in [110]. Hence, in the absence of the proximity induced magnetization, the SSE signal would be an intrinsic spin current effect free from any contamination by the anomalous Nernst effect. From here, we use the term AMR for the conventional AMR as discussed in §4.1.1, though SMR also shows the anisotropic behavior with different symmetry.

4.2Device Fabrication and Measurements

In this work, our main objective is first to distinguish and then to quantitatively separate the AMR and SMR effects in Pd/YIG and Pt/YIG bilayer systems. As discussed above, this study can be done by carefully rotating the magnetic field in the three orthogonal planes and measuring the corresponding rotation longitudinal MR and transverse Hall resistance, as shown in Figure IV-3. Besides, we notice that the proximity induced AMR should sensitively depend on the metal layer thickness for its interfacial nature, although SMR does not decay significantly within the spin diffusion length (~14 nm at 4.2 K for Pt [143]). Therefore, it is advantageous to determine the relative contributions from AMR and SMR in bilayer structure with a thin metal film as the spin diffusion length is systematically varied by lowering the temperature.

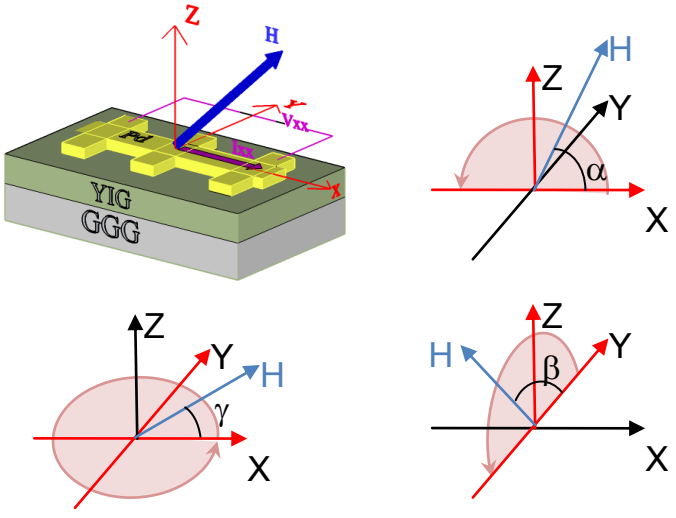


Figure IV-3 Schematic diagram of the patterned Hall bar and notations for field rotations for AMR/SMR experiments.

The YIG thin films are grown on GGG(110) substrates, as discussed in Chapter II, and morphology and the magnetic properties are discussed as well. However, we choose lift-off technique to fabricate the devices in this work, as shown in Figure IV-4, instead of the etching method described in §3.2. We have the advantage to define two Hall bars perpendicular to each other on the same chip by multiple photo-lithography exposures in the lift-off process, which is necessary in our study of the YIG crystalline orientation dependence of rotation MR discussed later.

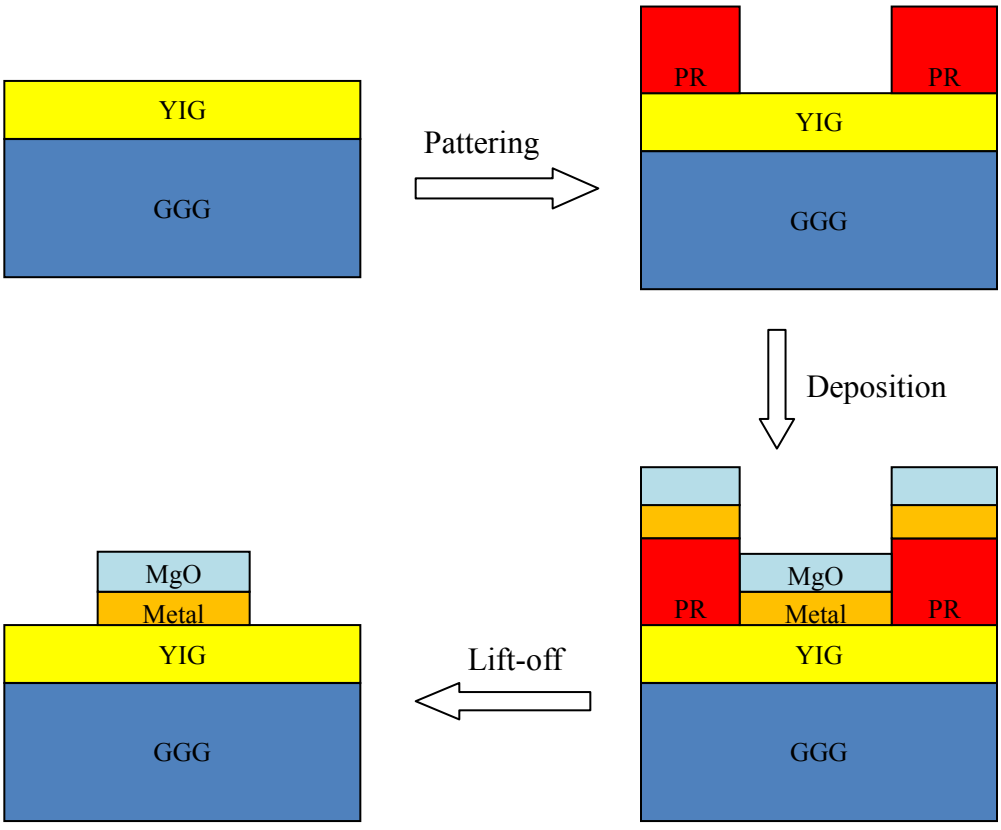


Figure IV-4 Schematic diagram of Hall bar device fabrication by lift-off method.

The two Hall bar patterns are patterned by photo-lithography twice using the same Hall bar mask. The process is similar to etching method described previously (see §3.2). However, the develop time of the first exposure-develop cycle is reduced to 20 seconds, except in the last cycle it is 60 seconds. The post-exposure baking is not necessary and not recommended in the lift-off method. The metal layers (Pd or Pt) are deposited with magnetron sputtering after light sputter cleaning of YIG surface. The thickness of the polycrystalline films of Pd or Pt ranges between 1.5 to 10 nm. In the case of Pd, a thin MgO layer is deposited on top to prevent oxidation. Magneto-transport measurements are performed in either a close-cycled refrigerator with an electromagnet (<1 T) or Quantum Design's physical property measurement system (<14 T) with a rotating stage.

4.3 Low-Field Magnetoresistance

Magnetoresistance of a Pd(2 nm)/YIG bilayer in an in-plane magnetic field, along longitudinal or transverse direction to the Hall bar, shows low-field dips (peaks) located at the coercive fields of YIG, as shown in Figure IV-5. This feature is reminiscent of the AMR effect in polycrystalline ferromagnetic materials, in which the resistivity has two-fold in-plane symmetry. In fact, the AMR-like feature in Pt/YIG was interpreted as evidence that Pt acquires a magnetic moment via MPE [109]. However, it was also pointed out that an alternative mechanism, i.e. SMR, can result in this resistivity feature, as discussed in §4.1.2.

Although originated from different mechanism, either AMR or SMR has the same dependence on magnetization for in-plane MR. Since the resistivity takes the maximum (minimum) value when the magnetization $\boldsymbol{M}$ is parallel (perpendicular) to the current direction, as an longitudinal field is swept through the coercive fields, $\boldsymbol{M}$ rotates from parallel to anti-parallel through transverse direction (as the in-plane magnetization anisotropy), and causes the resistivity dips to occur. It is similar for transverse magnetic field, though $\boldsymbol{M}$ rotate from transverse to anti-transverse through parallel (or anti-parallel) direction, causing resistivity peaks to occur. The magnitude of the MR ratio in the two geometries is supposed to be the same but may vary a little bit due to the sampling accuracy, as the magnetization flips at coercive field is very sharp and we can only measure an average signal around the coercive field.

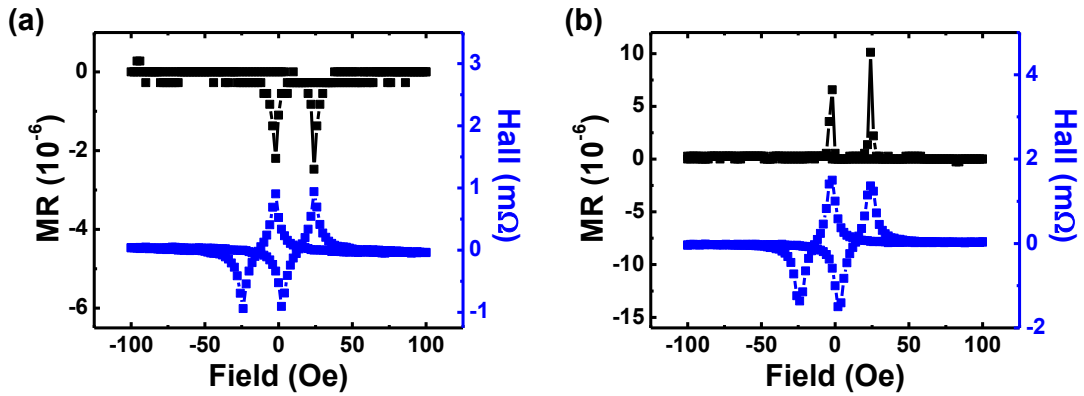


Figure IV-5 Low-field MR (black) and Hall resistance (blue) of Pd(2nm)/YIG with magnetic field applied in directions of (a) longitudinal, (b) transverse.

The transverse resistivity (Hall resistivity) has the same origin as the longitudinal MR, therefore it does not help to distinguish AMR from SMR, as shown in Figure IV-5 as well.

When magnetization rotates its relative direction to the current, both the positive and negative values of transverse resistivity occur near the coercive field, creating spikes.

4.4AMR vs. SMR

Clearly, the in-plane field sweep cannot distinguish AMR from SMR since both depend on the orientation of $\boldsymbol{M}$ in the xy-plane. By rotating $\boldsymbol{M}$ in specific planes, however, it is possible to differentiate these two effects.

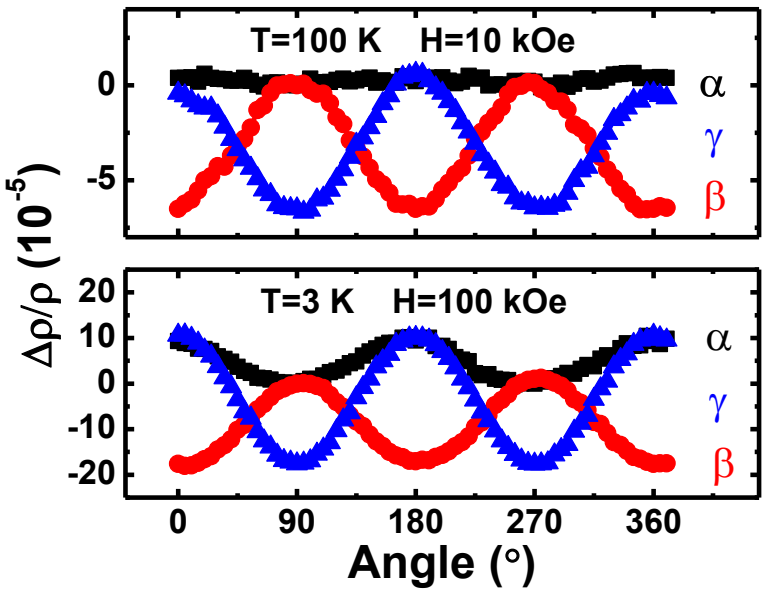


Figure IV-6 Comparison of two sets of typical field rotation data of Pd(2 nm)/YIG in three orthogonal planes (upper: H=10 kOe, T=100 K; lower: H=100 kOe, T=3 K). The notations α, β and γ denote xz-, yz- and xy-plane rotation.

As shown in Figure IV-2, if $\boldsymbol{M}$ is rotated in the xz-plane, only AMR is resulted, since m_y, and therefore, the reflection of j_s is unchanged. On the other hand, if $\boldsymbol{M}$ is rotated

in the yz-plane, only SMR is resulted, since the charge current is always perpendicular to $\boldsymbol{M}$. If $\boldsymbol{M}$ is rotated in the xy-plane, SMR and AMR are entangled. The three orthogonal planes are denoted as α (xz-plane), β (yz-plane), and γ (xy-plane) respectively, as shown in Figure IV-3.

Figure IV-6 shows two sets of typical field rotation data in the three orthogonal planes. First of all, it is noted that at high temperature (100 K) and low field (10 kOe), the phenomenon we observed (top panel) is consistent with the published experiments and the theoretical expectation of SMR [45,139,141,142]. In xz-plane rotation the longitudinal resistivity shows no significant change, which suggests negligible AMR contribution. In yz-plane rotation it shows a finite magnitude of oscillation with two-fold symmetry (period of 180°), which suggests finite SMR contribution. And the xy-plane rotation has the same magnitude as yz-plane, which suggests SMR dominates in the signal. On the other hand, it is surprising that new features arise when higher field or lower temperature is applied. It is shown in the bottom panel in Figure IV-6. The xz-plane rotation MR significantly increases and is distinguishable to yz-plane rotation MR, which suggests comparable AMR signal to SMR signal. And again, the in-plane rotation MR is the sum of the two.

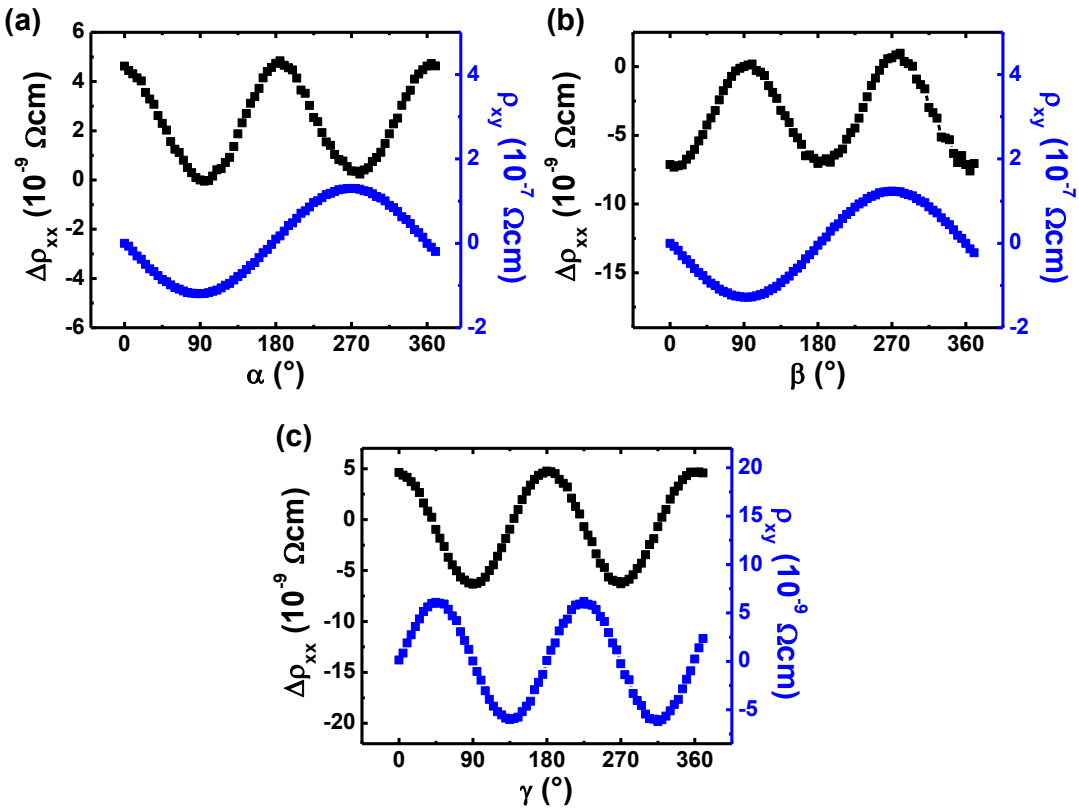


Figure IV-7 Typical field rotation data of Pd(2 nm)/YIG at high-field (100 kOe) and low-temperature (3 K) in three orthogonal planes: (a) xz-plane (AMR); (b) yz-plane (SMR); and (c) xy-plane (combined). The longitudinal resistance is shown in black and transverse (Hall) resistance is shown in blue.

It is also confirmed by examining the transverse (Hall) resistivity ρ_{xy} together with longitudinal resistivity ρ_{xx} in the three rotation planes, as shown in Figure IV-7. In the xz-plane and yz-plane rotation, the magnetic field rotates from in-plane to perpendicular to the sample plane, and OHE signal with uniaxial symmetry contributes to ρ_{xy} and it actually dominates, while ρ_{xx} of the two planes resemble AMR and SMR respectively. Nevertheless, in the xy-plane rotation, it is clear that ρ_{xy} has two-fold symmetry, which suggests ρ_{xy} in this case cannot originate from component of OHE. And it is noticeable

that the rotation phase of ρ_{xy} is 90° behind ρ_{xx}, and the magnitude of oscillation is the same as ρ_{xy}. All these phenomena are consistent with the expectation of PHE and SMR, as discussed in §4.1, though they are entangled in this geometry.

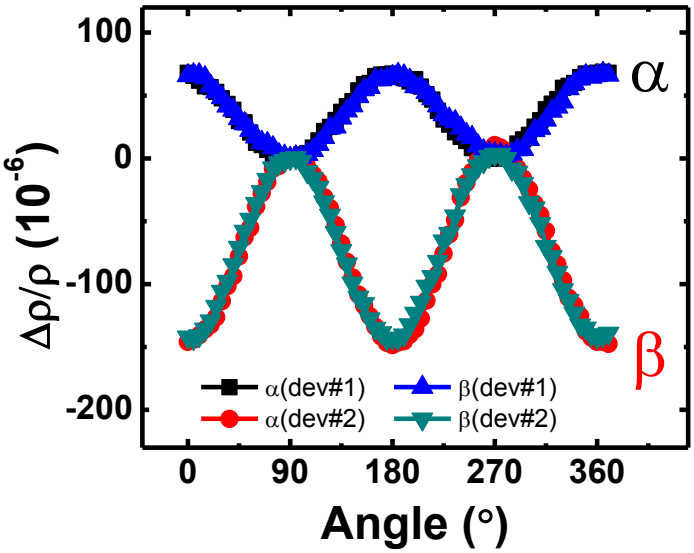


Figure IV-8 Rotation data from two perpendicular devices of Pd(2 nm)/YIG on the same chip are consistent (H=100 kOe, T=100 K). It indicates the rotation MR depends on the direction of magnetic moment, not the crystalline orientation of YIG film.

Furthermore, it is necessary to understand the crystalline orientation dependence of rotational MR. Even with all above demonstration, the phenomena are consistent with the model of combination of AMR and SMR, one question left unanswered is if SMR is related to crystalline anisotropy of AMR, which may break symmetry in the yz-plane and provide an extra feature in rotational MR. If this is true, AMR alone can explain the effects without invoking SMR. To answer this question, we first notice that the Pd or Pt films deposited on YIG are amorphous and the crystalline symmetry is not expected.

Furthermore, we prepared two devices perpendicular to each other on the same chip and measured the rotational MR at the same time. Figure IV-8 shows the results from such devices at T=100 K and H=100 kOe. It is clear that both the xz-plane and yz-plane rotational MR of the two devices are essentially identical, which suggests the effects do not depend on the crystalline orientation. We conclude that the rotational MR effects only depend on the relative direction between the current and the magnetization, thus indeed AMR and SMR.

4.5Temperature Dependence of AMR/SMR

Figure IV-9 shows a comparison of the relative changes of measured resistivity, $\frac{\Delta\rho}{\rho}$, below 100 K as a 10 kOe magnetic field is rotated in three orthogonal planes. The out-of-plane saturation field of YIG is ~ 2 kOe; therefore, the magnetic field of 10 kOe is sufficiently strong to align and rotate the YIG magnetization $\boldsymbol{M}$ in any direction. Figure IV-9(a) and (b) show $\frac{\Delta\rho}{\rho}$ as $\boldsymbol{M}$ rotates from the x- and y-directions towards the z-direction, respectively. $\frac{\Delta\rho}{\rho}$ is plotted relative to the resistivity when $\boldsymbol{M}$ is aligned with the z-axis, the common direction in these two cases. As $\boldsymbol{M}$ rotates from the x- to z-axis, the resistivity steadily decreases, as expected from AMR, i.e. $\rho_{\perp} < \rho_{\parallel}$. The resistivity oscillation is well fitted with, $\frac{\rho(\alpha)-\rho_z}{\rho_z} = 1 + \frac{\rho_x-\rho_z}{\rho_z} cos^2\alpha$, where ρ_x and ρ_z are the resistivity when $\boldsymbol{M}$ is along the x- and z- directions, respectively, and α is the angle between $\boldsymbol{M}$ and the x-axis in the xz-plane. However, as $\boldsymbol{M}$ approaches the z-axis from

the y-axis in the yz-plane, the resistivity increases instead, which is well fitted with $\frac{\rho(\beta)-\rho_z}{\rho_z} = 1 - \frac{\rho_z-\rho_y}{\rho_z} cos^2\beta$, where ρ_y is the resistivity when $\boldsymbol{M}$ is along the y-axis and β is the angle between $\boldsymbol{M}$ and the y-axis in the yz-plane. This is the situation when AMR is constant but the reflection of $\boldsymbol{j_s}$ varies from the strongest to weakest. Clearly we have $\rho_x > \rho_z > \rho_y$. When $\boldsymbol{M}$ lies in the xy-plane, the resistivity change is plotted as $\frac{\rho(\gamma)-\rho_y}{\rho_z} = 1 + \frac{\rho_x-\rho_y}{\rho_z} cos^2\gamma$, where γ is the angle between $\boldsymbol{M}$ and x-axis in the xy-plane. In this case, both AMR and SMR are present as γ is varied.

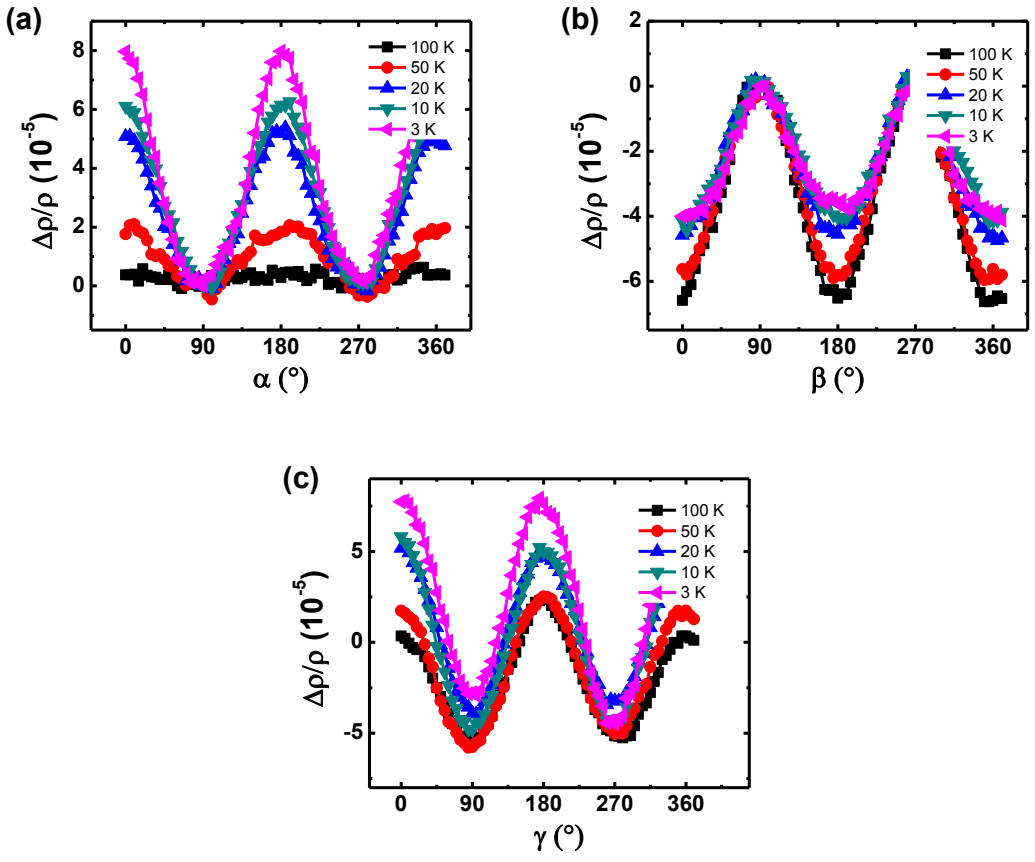


Figure IV-9 Low-field (10 kOe) rotation MR of Pd(2 nm)/YIG at different temperatures in three orthogonal planes: (a) xz-plane (AMR); (b) yz-plane (SMR); and (c) xy-plane (combined).

Figure IV-10 displays the temperature dependence of the three measured resistivity ratios: $\frac{\rho_x-\rho_z}{\rho_z}$, $\frac{\rho_z-\rho_y}{\rho_z}$, and $\frac{\rho_x-\rho_y}{\rho_z}$. Obviously, the sum of the first two which contains two independent AMR and SMR measurements should be equal to the third ratio. Both the sum and the experimentally measured third magnetoresistance ratio are also included in Figure IV-10.

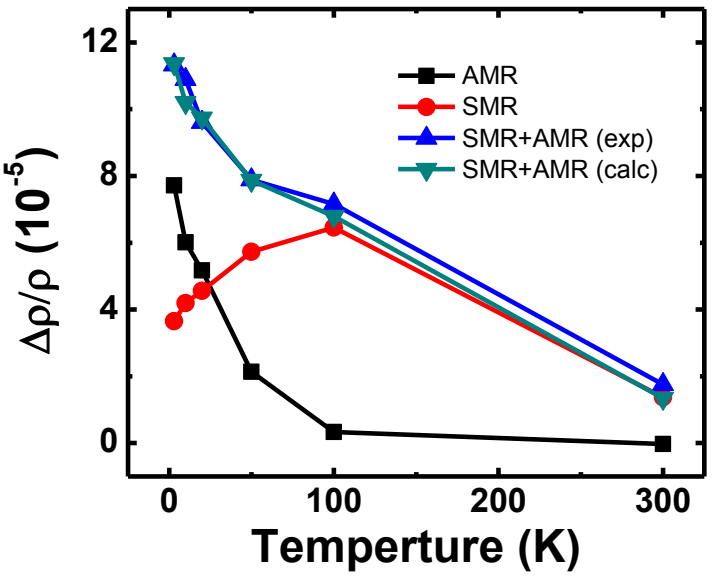


Figure IV-10 Temperature dependence of low-field (10 kOe) rotation MR ratio of Pd(2 nm)/YIG.

It is clear that at high temperatures, AMR is negligibly small and only SMR is present, which agrees with the previously reported observation [45] and seems to indicate the absence of AMR and therefore the proximity induced magnetization. However, as the temperature is lowered, AMR effect rises monotonically and does not appear to saturate, whereas SMR reaches its maximum at ~100 K and then starts to decrease. The fact that

they follow completely different temperature dependences suggests distinct physical mechanisms behind those two effects.

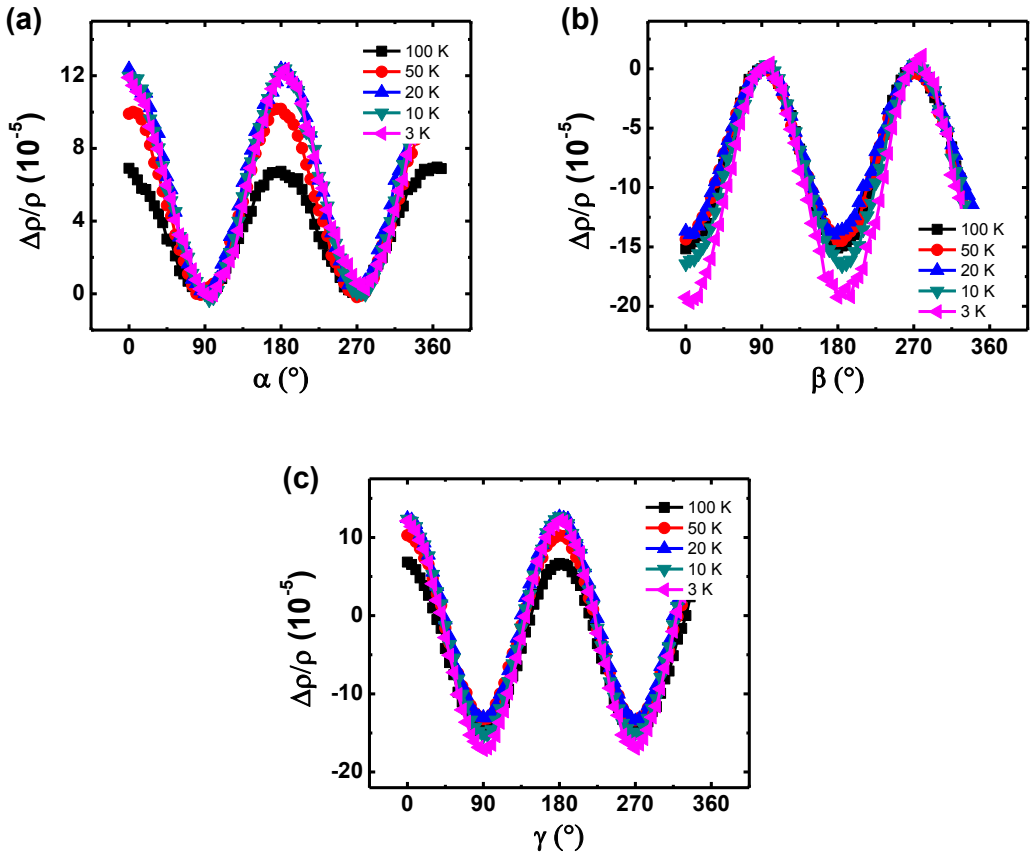


Figure IV-11 High-field (100 kOe) rotation MR of Pd(2 nm)/YIG at different temperatures in three orthogonal planes: (a) xz-plane (AMR); (b) yz-plane (SMR); and (c) xy-plane (combined).

The 10 kOe field is sufficiently strong to direct $\boldsymbol{M}$ of YIG along with the exchange induced magnetization in Pd at the interface, and the latter gives rise to AMR in Pd due to SOC. In the meantime, the aligned $\boldsymbol{M}$ of YIG can affect the reflection of $\boldsymbol{j_s}$; hence, to cause SMR as the direction of M rotates in space. In the previous work (see Chapter III), it is found that in addition to the induced magnetization in Pd which can be aligned with

relatively low fields, there are independent magnetic moments which can only be aligned with much higher magnetic fields (> 10 kOe), and they are shown to be related to the Pd/YIG interface. This high-field component should also produce additional AMR and SMR. Figure IV-11 reveals such high-field effects and shows similar rotational data to those in Figure IV-9. With a 100 kOe field, the resistivity changes show a large contrast with the 10 kOe results at all temperatures. Surprisingly, while AMR has only a moderate gain, SMR is greatly enhanced at all temperatures. The overall temperature dependence is summarized in Figure IV-12.

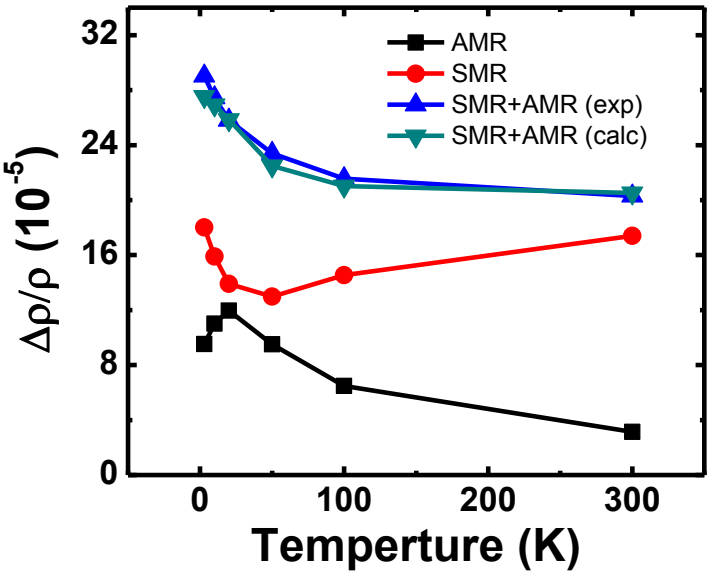


Figure IV-12 Temperature dependence of high-field (100 kOe) rotation MR ratio of Pd(2 nm)/YIG.

The coexistence of the proximity induced AMR and spin current related SMR is also found in Pt/YIG bilayer that was first studied. The overall behaviors such as temperature

and field dependences are qualitatively the same as in Pd/YIG, except that in Pt/YIG both SMR and AMR are larger in magnitude which is the consequence of a stronger SOC. The temperature dependence of both effects with a 100 kOe rotating field is shown in Figure IV-13.

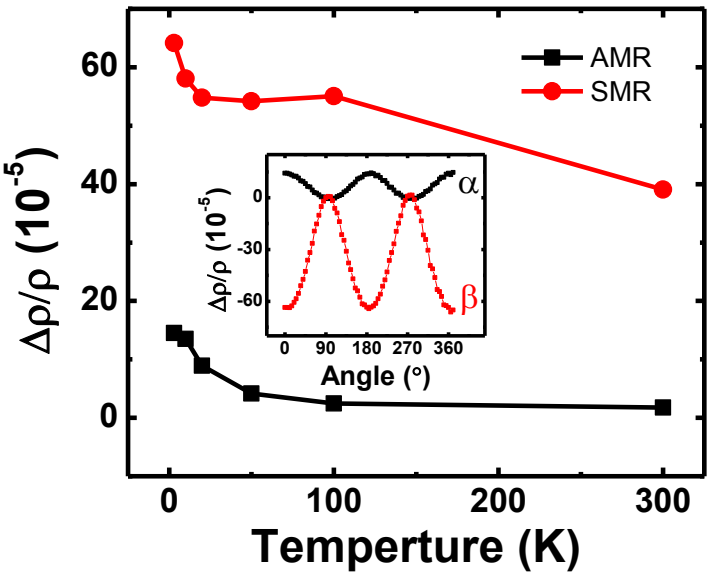


Figure IV-13 Pt(2 nm)/YIG temperature dependence of high-field (100 kOe) rotation MR ratio. Inset: High-field (100 kOe) rotation in xz- and yz-plane at 3 K.

4.6Field Dependence of AMR/SMR

As in conducting ferromagnetic materials, AMR associated with the proximity induced layer magnetization in Pd/YIG should saturate at relatively low fields. As the field rotates from x- to z-axis, it only needs to overcome the demagnetizing field to rotate the magnetization out of plane. Then the AMR ratio should not increase significantly as the

field strength is increased further. This is illustrated in Figure IV-14(a). The near saturation of AMR above 10 kOe suggests that the independent magnetic moments embedded in the Pd host do not produce any measurable AMR. Similar absence of AMR was also found in granular magnetoresistive solids which contain independent magnetic granules dispersed in non-magnetic metallic hosts [144]. We conclude that only the proximity-induced layer magnetization is responsible for the observed AMR effect. As shown in Figure IV-14(b), SMR does not have any sign of saturation up to 100 kOe; therefore, SMR must be associated with the independent moments at the interface that are also responsible for the anomalous Hall like signal, as discussed in Chapter III.

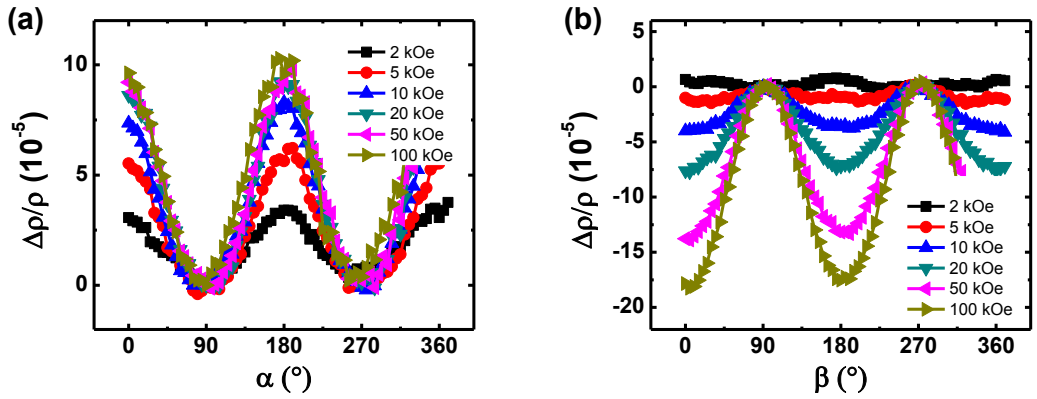


Figure IV-14 Field dependence of rotation MR of Pd(2 nm)/YIG at 3K in (a) xz-plane (AMR) and (b) yz-plane (SMR).

It is not difficult to understand that those independent moments can affect the spin current reflection as $\boldsymbol{j_s}$ approaches the interface region, which causes a large increase in SMR as

the magnetic moments are aligned by the increasing magnetic field. The comparison of SMR and AMR under a varying magnetic field is displayed in Figure IV-15.

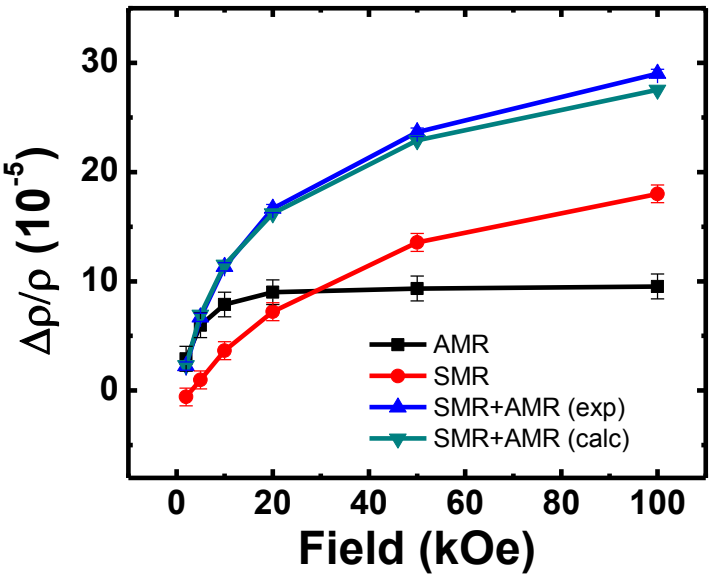


Figure IV-15 Field dependence of MR ratio of Pd(2 nm)/YIG at 3 K.

4.7Discussion

In the low field rotation experiments, AMR in general arises from spin-dependent scattering; and its magnitude increases as the temperature is lowered, which is caused by the suppression of the spin-flip scattering. In the normal metal/YIG devices, AMR only originates from the thin proximity induced interface layer which is diluted by the rest of the metal film. But as the mean-free-path increases at low temperatures, the interfacial contribution becomes more important. Hence, we expect a monotonic increase in AMR as the temperature is lowered. On the other hand, the spin diffusion length λ in the metal

increases at low temperatures (e.g. ~5.5 nm at room temperature [145] and ~25 nm at 4.2 K [143] for Pd). At some intermediate temperature, λ exceeds the metal film thickness d. As the temperature is further lowered, according to the SMR model [139], SMR $\sim\frac{1}{\sigma d+2\lambda^2 G_r}$, which actually starts to decrease, since both σ and λ increases at lower temperatures. This explains the observed temperature dependence of both effects. Clearly, the coexistence of these two effects unequivocally demonstrates the presence of the MPE in the bilayer devices.

In the high field rotation experiments, however, AMR and SMR show very different behavior, as shown before. The temperature dependence of AMR trends to saturate and even decrease, which might be associated to the Kondo screening of proximity-induced layer magnetization, as discussed in Chapter III. On the other hand, high field SMR does not saturate at low temperature, suggesting it is associated with the independent magnetic moments also responsible for AHE-like signal, which increases at low temperature. The different origins of the two effects can also be seen from the field dependence at low temperature in Figure IV-15.

In summary, we have disentangled the contributions between SMR and AMR by performing magnetoresistance measurements with rotating magnetic fields in three specific orthogonal planes. By lowering the temperatures, the spin-flip scattering is gradually suppressed; consequently, AMR is significantly enhanced. In the meantime,

SMR reaches a peak and starts to decrease. These results indicate that both the magnetic proximity effect and the spin current effect coexist in Pt/YIG and Pd/YIG bilayer systems, and could be analyzed quantitatively.

Chapter V

Appendix

5.1 Laboratory Instruments Management system (LIMs)

The Laboratory Instruments Management system (LIMs) is the framework designed for integrated and automatized instrumental control, data acquisition and analysis. LIMs is used in most of experiments in my works and some of the works of my colleagues. The current version of LIMs implementation is mostly in National Instruments LabVIEW, and some codes in Python, Delphi and FreeMat.

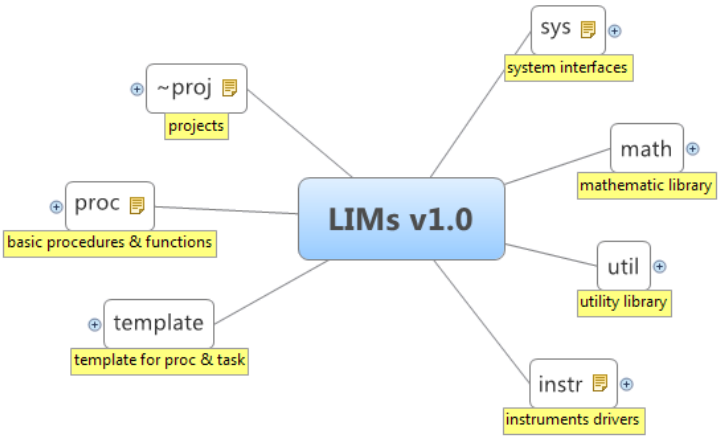


Figure V-1 Overview of LIMs, the sub-systems are shown in sub folders.

An overview of LIMs is list as Figure V-1. Seven sub-systems are included in the current version of LIMs, and each sub-system is grouped in individual folder, as described below.

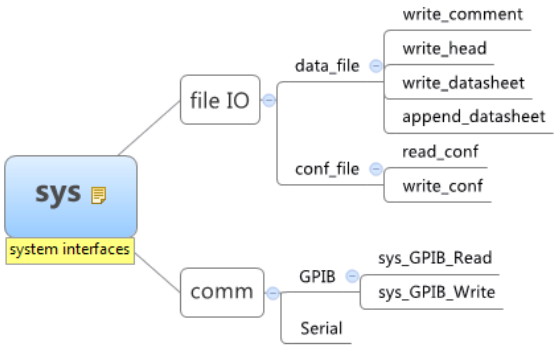


Figure V-2 LIMs sub-system of <sys> includes system level interfaces supporting instruments drivers.

The <sys> sub-system (Figure V-2) includes system level interfaces to support instruments drivers in <instr>. It is the abstraction of system dependent APIs so upper level sub-systems do not need to worry about the hardware and operating system. The "comm" sub-folder includes communication interfaces (GPIB, serial), and "file_IO" includes file manipulations. In LabVIEW implementation, <sys> is basically wrap functions of LabVIEW VIs.

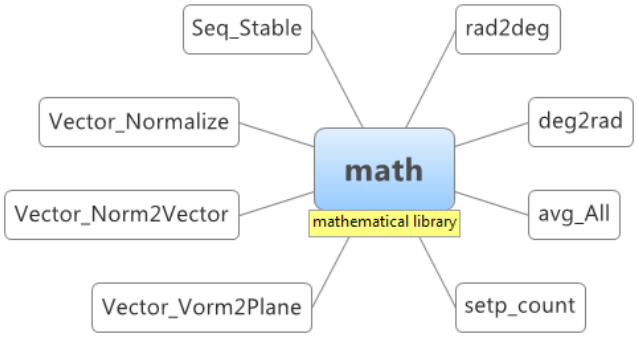


Figure V-3 LIMs sub-system of <math> includes mathematical library supporting experiments.

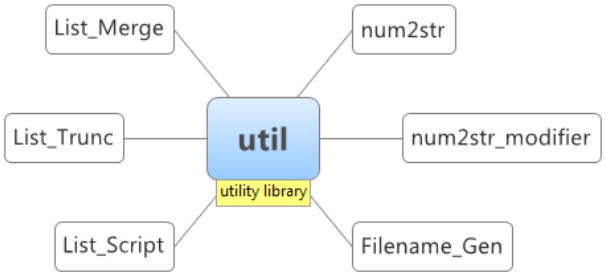


Figure V-4 LIMs sub-system of <util> includes procedure level utility library.

The <math> sub-system (Figure V-3) is the mathematical library supporting the experiments. And <util> sub-system (Figure V-4) includes other arbitrary utility library as string manipulation or list generation. These sub-systems provide fundamental functions in the upper level system implementation, and should not be specific to some experiment details.

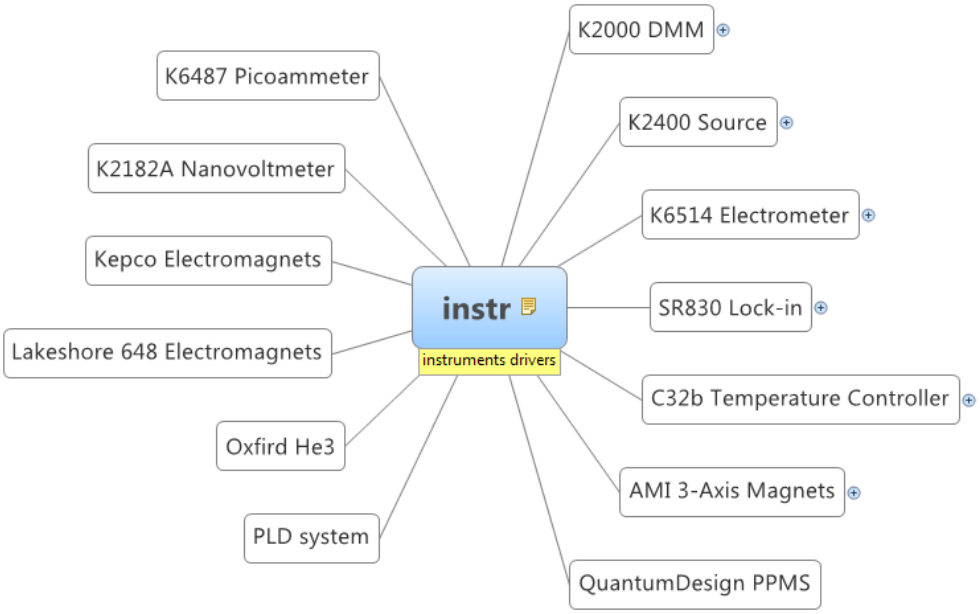


Figure V-5 LIMs sub-system of <instr> includes all drivers of the supported instruments.

The <instr> sub-system (Figure V-5) is the collection of all instrumental drivers. The folders are named as the name of systems supported. In general, the driver of each instrument consists of two sets of methods – "set" and "get", with a pre-fix of "set_" or "get_" respectively. The "set" methods set configurations or registers of the instrument, one function for one parameter, and "get" methods get data to registers from the instrument, depending on specific function of the instrument. It is recommended to get whole set of related data in one command, if supported by the hardware, to eliminate communication confliction.

The <template> sub-system defines templates for other sub-systems to simplify coding.

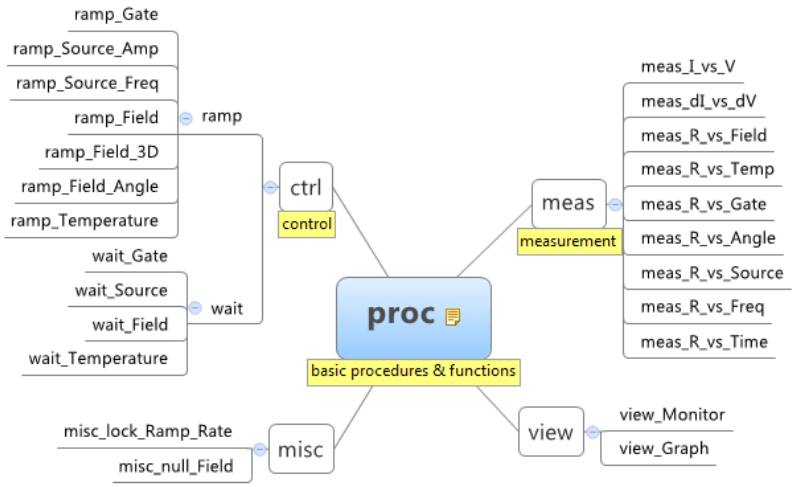


Figure V-6 LIMs sub-system of <proc> includes the basic procedures and functions for projects.

The <proc> sub-system (Figure V-6) includes the basic procedures and functions for advanced tasks. A "proc" is a route program to take a standard process, like a

measurement or control. Each proc is an abstract class of processing experiment. Therefore, it should be task-independent, and inhibit implemental details from higher-level application. In many cases, the <proc> sub-system can be merged into <~proj> folders as the operations are often task-dependent.

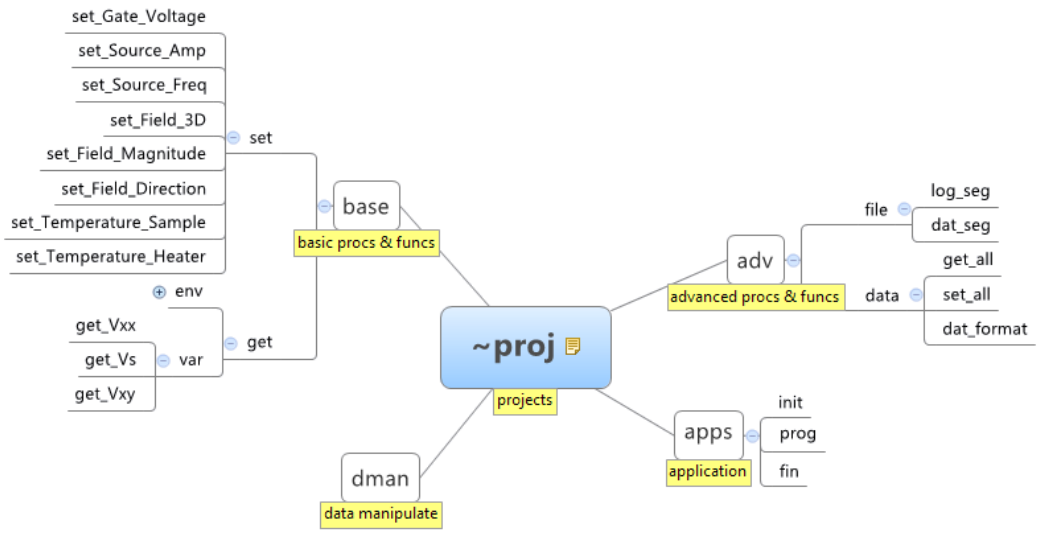


Figure V-7 LIMs sub-system of <~proj> includes experiment project level codes and information.

The <~proj> sub-system (Figure V-7) is the top level of LIMs and it has all information and codes of specific experiment project. Although logically it consists of "base", "adv", "dman" and "apps" sub-systems, its actual organization is the name of each project. The "base" includes basic methods of the project, as setting corresponding parameters or getting required data, and "adv" includes some enhanced methods derived from "base". "dman" stands for data manipulation and is mostly implemented in Python and FreeMat, which would be independent part, while some real-time data analysis and plotting is

included. And “app” is the integration of all sub-systems above to accomplish the project in a single application.

5.2 PLD Operational Manual

A brief summary of PLD operational manual will be listed in this section. The targets preparation and substrates treatment are discussed in each corresponding chapter of different materials.

5.2.1 Sample Loading

(1) Secure substrate onto the sample holder by tantalum clips. Check the cleanness of the holder and all accessories. Make sure the platinum foil is in place and the substrate is clipped evenly for good thermal contact.

(2) Mount holder firmly into the chamber with rotational arm at 270° (vertical position). Check electrical conductivity of the heater (sometimes a short voltage pulse of 3~5 V is helpful to remove oxidation layer on the contacts). Rotate arm to 0° (face down).

(3) Seal the chamber. Check *every* connection, windows and vent port of chamber and pumps before pumping. Any leakage will damage the system.

(4) Turn on mechanical pumps and monitor the system pressure. The pump-side pressure should reach less than $1x10^{-4}$ within 10 minutes and the chamber

pressure will be around 30 mTorr. Do not power on turbo pumps before the vacuum is roughly built.

(5) Turn on substrate heater and gradually increase the power to desire baking temperature. It is ok to power on turbo pumps while heating up the substrate, but pause heating up or slightly decrease heater power if the vacuum gets bad, to protect the pumps. Stop turbo pumps if necessary.

(6) Power on the two small turbo pumps of RHEED differential pumping stage. The pumps should reach normal speed of 1350 Hz within 5 minutes and the power should be no more than 9 W (usually 7-8 W). The chamber vacuum will be 20 mTorr or better.

(7) Power on the main turbo pump of the chamber. Check if low speed mode is selected and set to full speed. The pump should reach normal speed of 963 Hz within 5 minutes and the power should be no more than 10 W (usually 6 W). The chamber pressure will be better than 1 mTorr in 5 minutes and $5x10^{-6}$ Torr in 1 hour. The ion gauge could be turned on when vacuum is better than 10^{-5} Torr.

(8) Wait 1 hour to check the system is working properly. Leave it pumping overnight or for desire time.

5.2.2 System Startup

(1) Check system vacuum before your work. If it is abnormal, stop the system and check leakage. Turn off ion gauge if not deposit in UHV.

(2) Turn on laser system and let it warm up for 6 minutes. Open laser window lid. Check that the laser beam path is not obstructed and all optical components are clean.

(3) If background oxygen gas is necessary, open oxygen supply and tune the flow to 1-2 bubbles per second. Turn on ozone generator if necessary. Set main turbo pump to low speed (500 Hz).

(4) Gradually open leak valve to introduce oxygen into the chamber (when oxygen is necessary). Pause every quarter turn and let it stabilize for 2-3 minutes. The power of main turbo pump should not exceed 16 W.

(5) Gradually increase heater power to desire substrate temperature. Pause or decrease power if the chamber pressure increases too fast.

(6) Turn on RHEED and gradually set to desire grid high voltage (HV) and filament current (I_f), following the RHEED manual. It is recommended to pause every 2 kV of HV and 0.09A of I_f for 30-60 second, and pause at 20 kV of HV and 0.9 A of I_f for additional 5 minutes. Tune the RHEED to get clear pattern.

(7) Turn on step motors for target holder rotation.

5.2.3 Deposition Procedure

Follow the recipe of corresponding target material during deposition, as described in the text. During deposition, pay attention to the laser power, system vacuum, turbo pumps power, target plume, and substrate temperature, to ensure deposition conditions are satisfied for optimal film quality.

5.2.4 System Shutdown

(1) Turn off step motors for target holder rotation.

(2) Turn off laser system and close window lid.

(3) Gradually shut down RHEED system in the reverse procedure as starting up.

(4) Gradually turn off substrate heater power (or quench it if necessary).

(5) Gradually turn off oxygen leak valve. Pause every quarter turn. Be sure not to overly turn the valve. Close oxygen supply.

(6) Turn off ion gauge.

(7) Set main turbo pump to full speed (963 Hz). Wait until stable and then turn it off. Wait about 15 minutes and turn off the two small turbo pumps of RHEED system.

(8) Wait at least 60 minutes to let turbo pumps to slow down.

(9) Turn off mechanical pumps.

(10) Wait at least 60 minutes and then vent the chamber.

(11) Take the sample holder out of the chamber. Seal loading port. Remember to close the vent port.

(12) Pump the chamber following instructions in §5.2.1 if not to load new sample immediately.

Chapter VI

References

[1] R. Singh and J. Narayan, Phys. Rev. B **41**, 8843 (1990).

[2] H.-U. Krebs, M. Weisheit, J. Faupel, E. Süske, T. Scharf, C. Fuhse, M. Störmer, K. Sturm, M. Seibt, and H. Kijewski, in *Adv. Solid State Phys.* (Springer, 2003), pp. 505–518.

[3] E. Vasco, New J. Phys. **8**, 253 (2006).

[4] M. J. Aziz, Appl. Phys. **93**, 579 (2008).

[5] J. Ma, X. Liu, T. Lin, G. Gao, J. Zhang, W. Wu, X. Li, and J. Shi, Phys. Rev. B **79**, 174424 (2009).

[6] X. Liu, Experimental Studies of Oxide Magnetic Tunnel Junctions and Graphene, University of California, Riverside, 2012.

[7] *Colossal Magnetoresistive Manganites* (Kluwer Academic Publishers, Dordrecht ; Boston, 2004).

[8] T. Kimura and Y. Tokura, Annu. Rev. Mater. Sci. **30**, 451 (2000).

[9] J. M. D. Coey, M. Viret, and S. von Molnár, Adv. Phys. **48**, 167 (1999).

[10] A. Urushibara, T. Arima, A. Asamitsu, G. Kido, and Y. Tokura, Phys. Rev. B **51**, 14103 (1995).

[11] J.-H. Park, E. Vescovo, H.-J. Kim, C. Kwon, R. Ramesh, and T. Venkatesan, Nature **392**, 794 (1998).

[12] C. Zener, Phys. Rev. **81**, 440 (1951).

[13] C. Zener, Phys. Rev. **82**, 403 (1951).

[14] C. Zener, Phys. Rev. **83**, 299 (1951).

[15] T. A. Kaplan, S. D. Mahanti, and International Conference on Physics of Manganites, *Physics of Manganites* (Kluwer Academic/Plenum, 2010).

[16] R. J. Kennedy and P. A. Stampe, J. Phys. Appl. Phys. **32**, 16 (1999).

[17] S. Soeya, J. Hayakawa, H. Takahashi, K. Ito, C. Yamamoto, A. Kida, H. Asano, and M. Matsui, Appl. Phys. Lett. **80**, 823 (2002).

[18] E. J. Preisler, J. Brooke, N. C. Oldham, and T. C. McGill, J. Vac. Sci. Technol. B Microelectron. Nanometer Struct. **21**, 1745 (2003).

[19] D. Reisinger, M. Schonecke, T. Brenninger, M. Opel, A. Erb, L. Alff, and R. Gross, J. Appl. Phys. **94**, 1857 (2003).

[20] M. L. Paramês, J. Mariano, Z. Viskadourakis, N. Popovici, M. S. Rogalski, J. Giapintzakis, and O. Conde, Appl. Surf. Sci. **252**, 4610 (2006).

[21] S. Tiwari, R. Prakash, R. J. Choudhary, and D. M. Phase, J. Phys. Appl. Phys. **40**, 4943 (2007).

[22] D. Reisinger, B. Blass, J. Klein, J. B. Philipp, M. Schonecke, A. Erb, L. Alff, and R. Gross, Appl. Phys. Mater. Sci. Process. **77**, 619 (2003).

[23] G. Q. Gong, A. Gupta, G. Xiao, W. Qian, and V. P. Dravid, Phys. Rev. B **56**, 5096 (1997).

[24] D. Reisinger, P. Majewski, M. Opel, L. Alff, and R. Gross, Appl. Phys. Lett. **85**, 4980 (2004).

[25] T. Fukumura, H. Toyosaki, K. Ueno, M. Nakano, T. Yamasaki, and M. Kawasaki, Jpn. J. Appl. Phys. **46**, L642 (2007).

[26] A. Fernández-Pacheco, J. De Teresa, J. Orna, L. Morellon, P. Algarabel, J. Pardo, and M. Ibarra, Phys. Rev. B **77**, 100403 (2008).

[27] D. Venkateshvaran, W. Kaiser, A. Boger, M. Althammer, M. Rao, S. Goennenwein, M. Opel, and R. Gross, Phys. Rev. B **78**, 092405 (2008).

[28] A. Fernandez-Pacheco, in *Stud. Nanoconstrictions Nanowires Fe_3O_4 Thin Films* (Springer Berlin Heidelberg, Berlin, Heidelberg, 2011), pp. 51–82.

[29] S. Onoda, N. Sugimoto, and N. Nagaosa, Phys. Rev. Lett. **97**, 126602 (2006).

[30] W. Eerenstein, T. Palstra, T. Hibma, and S. Celotto, Phys. Rev. B **66**, 201101 (2002).

[31] F. Walz, J. Phys. Condens. Matter **14**, R285 (2002).

[32] S. Geller and M. A. Gilleo, J. Phys. Chem. Solids **3**, 30 (1957).

[33] V. Cherepanov, I. Kolokolov, and V. L'vov, Phys. Reports **229**, 81 (1993).

[34] T. Shintaku, A. Tate, and S. Mino, Appl. Phys. Lett. **71**, 1640 (1997).

[35] H. Hayashi, S. Iwasa, N. J. Vasa, T. Yoshitake, K. Ueda, S. Yokoyama, S. Higuchi, H. Takeshita, and M. Nakahara, Appl. Surf. Sci. **197**, 463 (2002).

[36] C.-Y. Tsay, C.-Y. Liu, K.-S. Liu, I.-N. Lin, L.-J. Hu, and T.-S. Yeh, J. Magn. Magn. Mater. **239**, 490 (2002).

[37] Y. Sun, Y.-Y. Song, H. Chang, M. Kabatek, M. Jantz, W. Schneider, M. Wu, H. Schultheiss, and A. Hoffmann, Appl. Phys. Lett. **101**, 152405 (2012).

[38] A. A. Serga, A. V. Chumak, and B. Hillebrands, J. Phys. Appl. Phys. **43**, 264002 (2010).

[39] B. Heinrich, C. Burrowes, E. Montoya, B. Kardasz, E. Girt, Y.-Y. Song, Y. Sun, and M. Wu, Phys. Rev. Lett. **107**, 066604 (2011).

[40] X. Jia, K. Liu, K. Xia, and G. E. W. Bauer, Epl Eur. Lett. **96**, 17005 (2011).

[41] C. Burrowes, B. Heinrich, B. Kardasz, E. A. Montoya, E. Girt, Y. Sun, Y.-Y. Song, and M. Wu, Appl. Phys. Lett. **100**, 092403 (2012).

[42] M. B. Jungfleisch, T. An, K. Ando, Y. Kajiwara, K. Uchida, V. I. Vasyuchka, A. V. Chumak, A. A. Serga, E. Saitoh, and B. Hillebrands, Appl. Phys. Lett. **102**, 062417 (2013).

[43] K. Uchida, J. Xiao, H. Adachi, J. Ohe, S. Takahashi, J. Ieda, T. Ota, Y. Kajiwara, H. Umezawa, H. Kawai, G. E. W. Bauer, S. Maekawa, and E. Saitoh, Nat. Mater. **9**, 894 (2010).

[44] D. Qu, S. Y. Huang, J. Hu, R. Wu, and C. L. Chien, Phys. Rev. Lett. **110**, 067206 (2013).

[45] H. Nakayama, M. Althammer, Y.-T. Chen, K. Uchida, Y. Kajiwara, D. Kikuchi, T. Ohtani, S. Geprägs, M. Opel, S. Takahashi, R. Gross, G. E. W. Bauer, S. T. B. Goennenwein, and E. Saitoh, Phys. Rev. Lett. **110**, 206601 (2013).

[46] Y. Krockenberger, H. Matsui, T. Hasegawa, M. Kawasaki, and Y. Tokura, Appl. Phys. Lett. **93**, 092505 (2008).

[47] Y. Krockenberger, K.-S. Yun, T. Hatano, S. Arisawa, M. Kawasaki, and Y. Tokura, J. Appl. Phys. **106**, 123911 (2009).

[48] M. Shone, Circuits Syst. Signal Process. **4**, 89 (1985).

[49] P. C. Dorsey, S. E. Bushnell, R. G. Seed, and C. Vittoria, J. Appl. Phys. **74**, 1242 (1993).

[50] R. Karim, S. A. Oliver, and C. Vittoria, Magn. Ieee Trans. **31**, 3485 (1995).

[51] A. Morimoto, Y. Maeda, T. Minamikawa, Y. Yonezawa, and T. Shimizu, Appl. Phys. **69**, S703 (1999).

[52] P. W. Jang and J. Y. Kim, Magn. Ieee Trans. **37**, 2438 (2001).

[53] N. Kumar, D. S. Misra, N. Venkataramani, S. Prasad, and R. Krishnan, J. Magn. Magn. Mater. **272-276**, E899 (2004).

[54] S. Yamamoto, H. Kuniki, H. Kurisu, M. Matsuura, and P. Jang, Phys. Status Solidi **201**, 1810 (2004).

[55] Y. Dumont, N. Keller, E. Popova, D. Schmool, M. Tessier, S. Bhattacharya, B. Stahl, R. Da Silva, and M. Guyot, Phys. Rev. B **76**, (2007).

[56] N. Kumar, S. Prasad, D. S. Misra, N. Venkataramani, M. Bohra, and R. Krishnan, J. Magn. Magn. Mater. **320**, 2233 (2008).

[57] Q.-H. Yang, H.-W. Zhang, Q.-Y. Wen, Y.-L. Liu, and J. Q. Xiao, J. Appl. Phys. **105**, 07A501 (2009).

[58] S. Katlakunta and S. R. Murthy, in (2012), pp. 719–720.

[59] N. . Ibrahim, C. Edwards, and S. . Palmer, J. Magn. Magn. Mater. **220**, 183 (2000).

[60] S. Kahl and A. M. Grishin, J. Appl. Phys. **93**, 6945 (2003).

[61] N. Nagaosa, J. Sinova, S. Onoda, A. H. MacDonald, and N. P. Ong, Rev. Mod. Phys. **82**, 1539 (2010).

[62] E. M. Pugh and T. W. Lippert, Phys. Rev. **42**, 709 (1932).

[63] R. Karplus and J. Luttinger, Phys. Rev. **95**, 1154 (1954).

[64] J. Smit, Physica **24**, 39 (1958).

[65] L. Berger, Phys. Rev. B **2**, 4559 (1970).

[66] Y. Tian, L. Ye, and X. Jin, Phys. Rev. Lett. **103**, 087206 (2009).

[67] K. Behnia, J. Phys. Condens. Matter **21**, 113101 (2009).

[68] K. Behnia, D. Jaccard, and J. Flouquet, J. Phys. Condens. Matter **16**, 5187 (2004).

[69] Y. Pu, D. Chiba, F. Matsukura, H. Ohno, and J. Shi, Phys. Rev. Lett. **101**, 117208 (2008).

[70] S. Y. Huang, W. G. Wang, S. F. Lee, J. Kwo, and C. L. Chien, Phys. Rev. Lett. **107**, 216604 (2011).

[71] J. Weischenberg, F. Freimuth, S. Blügel, and Y. Mokrousov, Phys. Rev. B **87**, 060406 (2013).

[72] M. Hatami, G. Bauer, Q. Zhang, and P. Kelly, Phys. Rev. B **79**, 174426 (2009).

[73] M. I. Dyakonov and V. I. Perel, Phys. Lett. **35**, 459 (1971).

[74] M. I. D'Yakonov and V. I. Perel', Sov. J. Exp. Theor. Phys. Lett. **13**, 467 (1971).

[75] J. E. Hirsch, Phys. Rev. Lett. **83**, 1834 (1999).

[76] J. Sinova, D. Culcer, Q. Niu, N. Sinitsyn, T. Jungwirth, and A. MacDonald, Phys. Rev. Lett. **92**, 126603 (2004).

[77] J. Schliemann, Int. J. Mod. Phys. B **20**, 1015 (2006).

[78] G. Y. Guo, S. Murakami, T.-W. Chen, and N. Nagaosa, Phys. Rev. Lett. **100**, 096401 (2008).

[79] Y. K. Kato, Science **306**, 1910 (2004).

[80] J. Wunderlich, B. Kaestner, J. Sinova, and T. Jungwirth, Phys. Rev. Lett. **94**, 047204 (2005).

[81] A. A. Bakun, B. P. Zakharchenya, A. A. Rogachev, M. N. Tkachuk, and V. G. Fleĭsher, Sov. J. Exp. Theor. Phys. Lett. **40**, 1293 (1984).

[82] E. Saitoh, M. Ueda, H. Miyajima, and G. Tatara, Appl. Phys. Lett. **88**, 182509 (2006).

[83] S. O. Valenzuela and M. Tinkham, Nature **442**, 176 (2006).

[84] T. Kimura, Y. Otani, T. Sato, S. Takahashi, and S. Maekawa, Phys. Rev. Lett. **98**, 156601 (2007).

[85] H. Zhao, E. Loren, H. van Driel, and A. Smirl, Phys. Rev. Lett. **96**, 246601 (2006).

[86] C. W. Koong, B.-G. Englert, C. Miniatura, and N. Chandrasekhar, Arxiv Prepr. Arxiv10041273 (2010).

[87] L. Liu, R. A. Buhrman, and D. C. Ralph, Arxiv Prepr. Arxiv11113702 (2011).

[88] G. E. W. Bauer, E. Saitoh, and B. J. van Wees, Nat. Mater. **11**, 391 (2012).

[89] K. Uchida, S. Takahashi, K. Harii, J. Ieda, W. Koshibae, K. Ando, S. Maekawa, and E. Saitoh, Nature **455**, 778 (2008).

[90] C. M. Jaworski, J. Yang, S. Mack, D. D. Awschalom, J. P. Heremans, and R. C. Myers, Nat. Mater. **9**, 898 (2010).

[91] S. Bosu, Y. Sakuraba, K. Uchida, K. Saito, T. Ota, E. Saitoh, and K. Takanashi, Phys. Rev. B **83**, 224401 (2011).

[92] K. Uchida, T. Nonaka, T. Ota, and E. Saitoh, Appl. Phys. Lett. **97**, 262504 (2010).

[93] R. Ramos, T. Kikkawa, K. Uchida, H. Adachi, I. Lucas, M. H. Aguirre, P. Algarabel, L. Morellón, S. Maekawa, and E. Saitoh, Appl. Phys. Lett. **102**, 072413 (2013).

[94] H. Adachi, K. Uchida, E. Saitoh, and S. Maekawa, Reports Prog. Phys. **76**, 036501 (2013).

[95] J. Xiao, G. E. W. Bauer, K. Uchida, E. Saitoh, and S. Maekawa, Phys. Rev. B **81**, 214418 (2010).

[96] H. Adachi, J. Ohe, S. Takahashi, and S. Maekawa, Phys. Rev. B **83**, 094410 (2011).

[97] H. Adachi, K. Uchida, E. Saitoh, J. Ohe, S. Takahashi, and S. Maekawa, Appl. Phys. Lett. **97**, 252506 (2010).

[98] K. Uchida, H. Adachi, T. Ota, H. Nakayama, S. Maekawa, and E. Saitoh, Appl. Phys. Lett. **97**, 172505 (2010).

[99] K. Uchida, H. Adachi, T. An, T. Ota, M. Toda, B. Hillebrands, S. Maekawa, and E. Saitoh, Nat. Mater. **10**, 737 (2011).

[100] A. Kirihara, K. Uchida, Y. Kajiwara, M. Ishida, Y. Nakamura, T. Manako, E. Saitoh, and S. Yorozu, Nat. Mater. **11**, 686 (2012).

[101] C. M. Jaworski, R. C. Myers, E. Johnston-Halperin, and J. P. Heremans, Nature **487**, 210 (2012).

[102] S. Hoffman, K. Sato, and Y. Tserkovnyak, *Landau-Lifshitz Theory of the Spin Seebeck Effect* (2013).

[103] J. J. Hauser, Phys. Rev. **187**, 580 (1969).

[104] S. Ruegg, G. Schutz, P. Fischer, R. Wienke, W. B. Zeper, and H. Ebert, J. Appl. Phys. **69**, 5655 (1991).

[105] W. Antel, M. Schwickert, T. Lin, W. O'Brien, and G. Harp, Phys. Rev. B **60**, 12933 (1999).

[106] F. Wilhelm, P. Poulopoulos, G. Ceballos, H. Wende, K. Baberschke, P. Srivastava, D. Benea, H. Ebert, M. Angelakeris, and N. K. Flevaris, Phys. Rev. Lett. **85**, 413 (2000).

[107] F. Wilhelm, M. Angelakeris, N. Jaouen, P. Poulopoulos, E. Papaioannou, C. Mueller, P. Fumagalli, A. Rogalev, and N. Flevaris, Phys. Rev. B **69**, 220404 (2004).

[108] J. R. Barnes, S. J. OShea, M. E. Welland, J.-Y. Kim, J. E. Evetts, and R. E. Somekh, J. Appl. Phys. **76**, 2974 (1994).

[109] S. Y. Huang, X. Fan, D. Qu, Y. P. Chen, W. G. Wang, J. Wu, T. Y. Chen, J. Q. Xiao, and C. L. Chien, Phys. Rev. Lett. **109**, 107204 (2012).

[110] T. Kikkawa, K. Uchida, Y. Shiomi, Z. Qiu, D. Hou, D. Tian, H. Nakayama, X.-F. Jin, and E. Saitoh, Phys. Rev. Lett. **110**, 067207 (2013).

[111] S. Geprags, S. Meyer, S. Altmannshofer, M. Opel, F. Wilhelm, A. Rogalev, R. Gross, and S. T. Goennenwein, Appl. Phys. Lett. **101**, 262407 (2012).

[112] Y. M. Lu, Y. Choi, C. M. Ortega, X. M. Cheng, J. W. Cai, S. Y. Huang, L. Sun, and C. L. Chien, Phys. Rev. Lett. **110**, 147207 (2013).

[113] J. Vogel, A. Fontaine, V. Cros, F. Petroff, J.-P. Kappler, G. Krill, A. Rogalev, and J. Goulon, Phys. Rev. B **55**, 3663 (1997).

[114] G. Y. Guo, J. Appl. Phys. **105**, 07C701 (2009).

[115] P. Coleman, P. W. Anderson, and T. V. Ramakrishnan, Phys. Rev. Lett. **55**, 414 (1985).

[116] G.-Y. Guo, S. Maekawa, and N. Nagaosa, Phys. Rev. Lett. **102**, 036401 (2009).

[117] A. Fert, A. Friederich, and A. Hamzic, J. Magn. Magn. Mater. **24**, 231 (1981).

[118] A. J. Manuel and M. McDougald, J. Phys. C Solid State Phys. **3**, 147 (1970).

[119] M. N. Baibich, J. M. Broto, A. Fert, F. N. Van Dau, F. Petroff, P. Etienne, G. Creuzet, A. Friederich, and J. Chazelas, Phys. Rev. Lett. **61**, 2472 (1988).

[120] G. Binasch, P. Grünberg, F. Saurenbach, and W. Zinn, Phys. Rev. B **39**, 4828 (1989).

[121] G. H. Jonker and J. H. Van Santen, Physica **16**, 337 (1950).

[122] M. Julliere, Phys. Lett. **54**, 225 (1975).

[123] T. Miyazaki and N. Tezuka, J. Magn. Magn. Mater. **139**, L231 (1995).

[124] A. W. Rushforth, K. Výborný, C. S. King, K. W. Edmonds, R. P. Campion, C. T. Foxon, J. Wunderlich, A. C. Irvine, P. Vašek, V. Novák, K. Olejník, J. Sinova, T. Jungwirth, and B. L. Gallagher, Phys. Rev. Lett. **99**, 147207 (2007).

[125] D. Wu, P. Wei, E. Johnston-Halperin, D. D. Awschalom, and J. Shi, Phys. Rev. B **77**, 125320 (2008).

[126] A. W. Rushforth, K. Výborný, C. S. King, K. W. Edmonds, R. P. Campion, C. T. Foxon, J. Wunderlich, A. C. Irvine, V. Novák, K. Olejník, A. A. Kovalev, J. Sinova, T. Jungwirth, and B. L. Gallagher, J. Magn. Magn. Mater. **321**, 1001 (2009).

[127] C. M. Wang, Phys. Rev. B **82**, 165331 (2010).

[128] T. McGuire and R. Potter, Magn. Ieee Trans. **11**, 1018 (1975).

[129] W. Gil, D. Görlitz, M. Horisberger, and J. Kötzler, Phys. Rev. B **72**, 134401 (2005).

[130] K. M. Seemann, F. Freimuth, H. Zhang, S. Blügel, Y. Mokrousov, D. E. Bürgler, and C. M. Schneider, Phys. Rev. Lett. **107**, 086603 (2011).

[131] J. N. Eckstein, I. Bozovic, J. ODonnell, M. Onellion, and M. S. Rzchowski, Appl. Phys. Lett. **69**, 1312 (1996).

[132] M. Ziese and S. P. Sena, J. Phys. Condens. Matter **10**, 2727 (1998).

[133] R. Ramos, S. Arora, and I. Shvets, Phys. Rev. B **78**, 214402 (2008).

[134] N. Naftalis, Y. Bason, J. Hoffman, X. Hong, C. H. Ahn, and L. Klein, J. Appl. Phys. **106**, 023916 (2009).

[135] H. Tang, R. Kawakami, D. Awschalom, and M. Roukes, Phys. Rev. Lett. **90**, 107201 (2003).

[136] V. D. Ky, Phys. Status Solidi B **26**, 565 (1968).

[137] I. Genish, L. Klein, J. Reiner, and M. Beasley, Phys. Rev. B **75**, 125108 (2007).

[138] C. Hahn, G. de Loubens, O. Klein, M. Viret, V. V. Naletov, and J. Ben Youssef, Phys. Rev. B **87**, 174417 (2013).

[139] Y.-T. Chen, S. Takahashi, H. Nakayama, M. Althammer, S. T. B. Goennenwein, E. Saitoh, and G. E. W. Bauer, Phys. Rev. B **87**, 144411 (2013).

[140] T. Lin, C. Tang, and J. Shi, Preprint (2013).

[141] M. Althammer, S. Meyer, H. Nakayama, M. Schreier, S. Altmannshofer, M. Weiler, H. Huebl, S. Geprägs, M. Opel, R. Gross, D. Meier, C. Klewe, T. Kuschel, J.-M. Schmalhorst, G. Reiss, L. Shen, A. Gupta, Y.-T. Chen, G. E. W. Bauer, E. Saitoh, and S. T. B. Goennenwein, Phys. Rev. B **87**, 224401 (2013).

[142] N. Vlietstra, J. Shan, V. Castel, J. B. Youssef, and B. J. van Wees, Arxiv Prepr. Arxiv13013266 (2013).

[143] H. Kurt, R. Loloee, K. Eid, W. P. Pratt, and J. Bass, Appl. Phys. Lett. **81**, 4787 (2002).

[144] C. L. Chien, Annu. Rev. Mater. Sci. **25**, 129 (1995).

[145] V. Vlaminck, J. E. Pearson, S. D. Bader, and A. Hoffmann, Arxiv Prepr. Arxiv13050745 (2013).